1987

Penumbral Distributions For High-energy Radiotherapy Photon Beams: Experimental And Theoretical Determinations

Ayoola Clement Akinradewo

CANADIAN THESES

THÈSES CANADIENNES

NOTICE

The quality of this microfiche is heavily dependent upon the quality of the original thesis submitted for microfilming. Every effort has been made to ensure the highest quality of reproduction possible.

If pages are missing, contact the university which granted the degree.

Some pages may have indistinct print especially if the original pages were typed with a poor typewriter ribbon or if the university sent us an inferior photocopy.

Previously copyrighted materials (journal articles, published tests, etc.) are not filmed.

Reproduction in full or in part of this film is governed by the Canadian Copyright Act, R.S.C. 1970, c. C-30.

AVIS

La qualité de cette microfiche dépend grandement de la qualité de la thèse soumise au microfilmage. Nous avons tout fait pour assurer une qualité supérieure de reproduction.

S'il manque des pages, veuillez communiquer avec l'université qui a conféré le grade.

La qualité d'impression de certaines pages peut laisser à désirer, surtout si les pages originales ont été dactylographiées à l'aide d'un ruban usé ou si l'université nous a fait parvenir une photocopie de qualité inférieure.

Les documents qui font déjà l'objet d'un droit d'auteur (articles de revue, examens publiés, etc.) ne sont pas microfilmés.

La reproduction, même partielle, de ce microfilm est soumise à la Loi canadienne sur le droit d'auteur, SRC 1970, c. C-30.

THIS DISSERTATION HAS BEEN MICROFILMED EXACTLY AS RECEIVED

LA THÈSE A ÉTÉ MICROFILMÉE TELLE QUE NOUS L'AVONS REÇUE

PENUMBRAL DISTRIBUTIONS FOR HIGH-ENERGY RADIOTHERAPY PHOTON BEAMS

-o-

Experimental and Theoretical Determinations

by

Ayoola Clement Akinradewo

Department of Physics

Submitted in partial fulfillment
of the requirements for the degree of
Doctor of Philosophy

Faculty of Graduate Studies
The University of Western Ontario
London, Ontario, Canada

November, 1986

ISBN 0-315-36063-1

ABSTRACT

A penumbral model is adopted which considers that two distributions exist in the penumbral region of high-energy radiotherapy units namely, the photon-fluence and the dose distributions. The difference between these two distributions is associated with the lateral spread of the secondary electrons and is strongly dependent on the beam energy and electron density of the medium of interaction.

Specially-designed cylindrical ionization chambers of varying inside diameters were used to determine the primary penumbral dose distributions in media of varying electron density for Co-60, 6- and 31-MV x-ray beams. The results indicate that the measured penumbral dose distributions must be corrected for the inside diameter of the ionization chamber. The penumbral primary dose distributions in lung-equivalent media are significantly broader than those in soft tissue. The difference increases with the beam energy.

Primary penumbral dose distributions in media of varying electron density were also calculated using convolution techniques. Primary dose spread functions were calculated using a modified electron transport model involving both the Klein-Nishina differential collision formula and stopping powers. The primary dose spread functions (or kernels) were

convolved with the appropriate primary penumbral photon-fluence distributions to obtain the corresponding penumbral primary dose distributions in homogeneous phantoms. There was satisfactory agreement between theory and experiment.

The results of the project indicate that the lateral spread of the secondary electrons set in motion by photon interactions increases with the beam energy and decreasing electron density of the medium. This increase in the lateral spread of the secondary electrons results in the broadening of the penumbral dose distributions of high-energy photon beams. The study of these effects should lead to a better understanding of the approximations involved in ignoring electron-fluence effects in the irradiated patient.

ACKNOWLEDGEMENTS

I would like to thank my supervisor, Dr. D.J. Dawson, for his support and guidance over the years. I would also like to thank the members of my Advisory Committee, Drs J.C.F. MacDonald, G.S. Rose and P.W. Whippey, for their guidance and special thanks to the Chairman of the Department of Physics, Professor G.S. Rose, for his kindness and encouragement.

The help by Mr. Jed Schroeder in the development of the program used in the calculation of the kernels is acknowledged with thanks. My gratitude also goes to Mr. Wayne Wissing for keeping the electronic equipment functioning and to the men in the instrument shop, especially Mr. George Yelland, for the excellent job done in the construction of the specially-designed ionization chambers.

My profound appreciation goes to the Ontario Cancer Research and Treatment Foundation, London Regional Cancer Centre, for allowing me the use of their facilities.

To my wife, Adenike

and

My sons, Fiyinfolu and Foluso

TABLE OF CONTENTS

LIST OF TABLES

LIST OF FIGURES

CHAPTER I

INTRODUCTION

In radiation therapy it is invariably necessary to shield parts of the object (or patient) from the source of electromagnetic radiation. This shielding is achieved with a set of beam defining blocks called collimators. Some treatment techniques also require additional shielding of some organs in the treatment field such as the lungs in the mantle technique used in the treatment of Hodgkin's disease [26,34]. The physical edges of the beam in these cases are never infinitely sharp and the region of partial shadow is called the beam penumbra.

Measurements of beam penumbra for high-energy radiotherapy machines is undertaken routinely for new installations at most radiotherapy treatment centres as they are required input data for treatment planning computers. To date, however, little emphasis has been placed on the physical processes that result in the beam penumbra, and far less on the correct interpretation of the measured penumbra and the accuracy of the measurement methodology. This work, for the first time, clearly defines the sources of beam penumbra, describes accurate methods of measurement of penumbral distributions in clinical conditions, provides an interpretation of the measured penumbral distribution, and discusses the impact of the dosemeter type and configuration on penumbral

distributions.

1.1 Beam Penumbra and its Sources

1.1.1 Primary Beam Penumbra

The source-collimator arrangement of a radiotherapy machine, an AECL Therac-6 6-MV linear accelerator, and the block diagram of a typical radiotherapy machine with a finite source size are illustrated in Figure 1.1. The line joining the centre of the source, S, to the centre of the beam, O, is called the central axis.

The beam of radiation incident on an object (or patient) is referred to as the primary beam and includes both the primary photons and the scattered radiation from the collimators [5]. Neglecting the inverse square law and source attenuation, and considering the primary photons only, the intensity of the beam is uniform in the region XX' because all of the source is seen. In the region XYZ and X'Y'Z', however, the intensity of the radiation decreases rapidly. At points Y and Y', 50 % of the source is seen and the dimension, YY', defines the field size. Beyond the points Z and Z' none of the source is seen. This region of varying intensity (XYZ and X'Y'Z') is called the primary penumbral region.

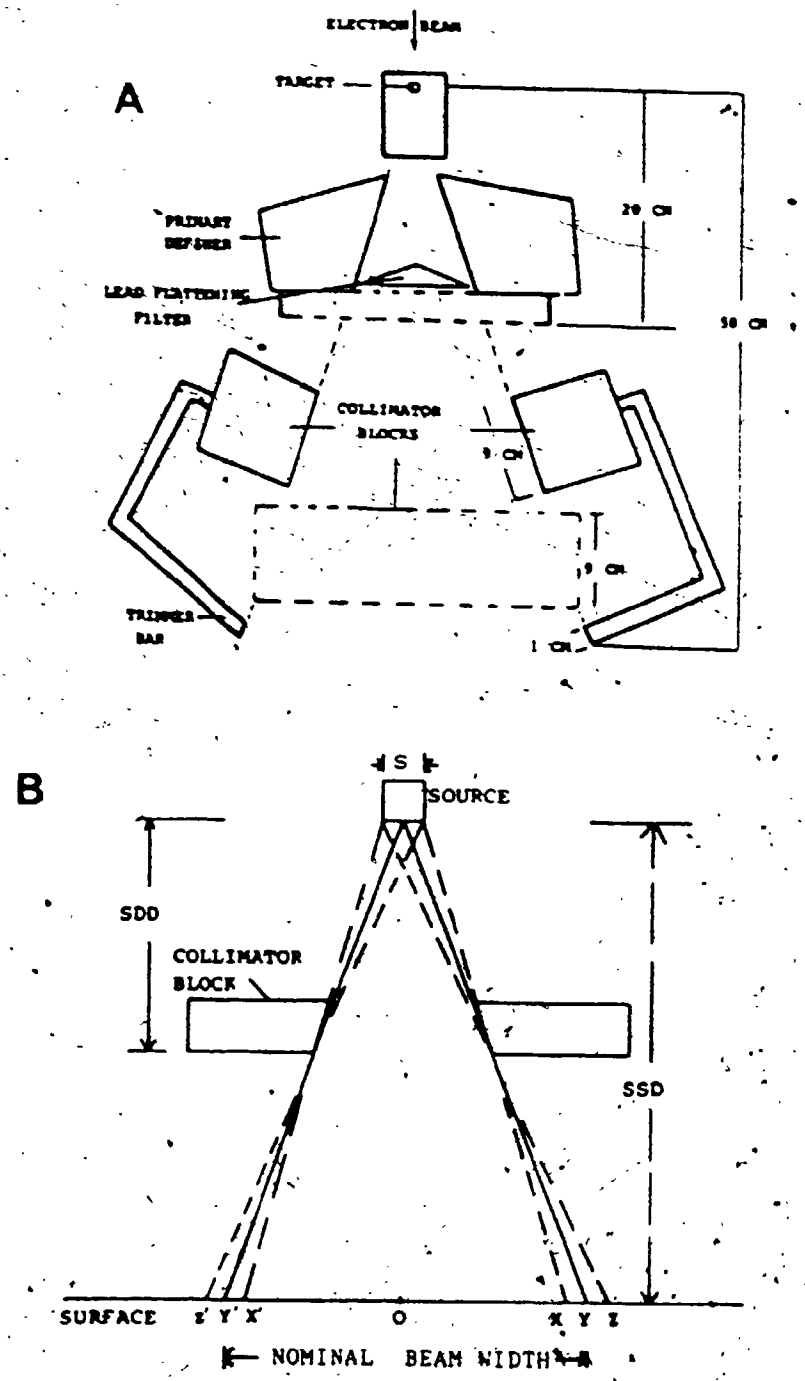

Figure 1.1: (a) Source-Collimator Arrangement of an AECL Therac-6, 6-MV linac; (b) The Surface Penumbra for a Therapy Machine with a Finite Source Size.

The primary beam penumbral width, P_s, at any distance from the collimators follows the geometric law:

$$P_s = \frac{s(SSD-SDD)}{SDD}$$

where s is the source size, SSD is the source-surface distance and SDD is the source-diaphragm distance. [62]

P_s, the geometric penumbra, depends on the source size, the collimator-surface distance and the source-surface distance. For a point source, the geometric penumbra is zero, i.e $P_s = 0$ if $s=0$. For all practical situations, however, the source diameter is finite. For a Co-60 unit, the source diameters vary from 1.0 to 2.5 cm. For accelerators, the source diameters vary from about 0.1 to 0.4 cm.

1.1.2 Scatter Penumbra

Scatter radiation can arise from two major sources namely, the source-collimator system and the phantom. As indicated previously, the source-collimator scatter cannot be readily separated from the primary and hence is normally considered as a component of the primary [5,62].

This collimator scatter includes scattered photons and secondary electrons arising from photon interactions in both the source (or focal spot and flattener) and the

collimators. Some of these secondary electrons are removed through interactions in the air mass between the collimators and irradiated surface. With either sufficient distance between the collimators and the surface or the use of electron filters, the contribution of collimator scattered electrons incident on the patient is small [5,62].

The phantom scatter arises from photon interactions with the phantom material (or patient tissue). The contribution of scattered photons increases with the field size and depth. Naturally, the contribution of scattered photons is maximum at the central axis and decreases toward the edge of the beam. Scatter penumbra arises from this component.

For measurements in air (in which the sensitive volume of the radiation detector is surrounded by the maximum electronic equilibrium thickness) there is a negligible or constant phantom scatter component and therefore, the measured penumbra closely approximates the geometric penumbral distribution.

1.1.3 Transmission Penumbra

There is an additional component to the penumbra associated with transmission through the collimators. Since the source is aligned with the collimator faces for

all field sizes, there is minimal absorption penumbra across the collimator face. The collimators are normally thick enough to reduce the transmission component to less than 1%.

1.1.4 Depth of Maximum Electronic Buildup

The transfer of energy from a photon beam to a medium takes place in two stages. The first stage involves the interaction of the photons with the atoms of the medium resulting in the production of high energy electrons. This stage is described by a quantity termed the kerma, which is the kinetic energy transferred from the photons to the secondary electrons per unit mass of the medium [62].

The second stage involves the transfer of energy from the high-energy secondary electrons to the medium through excitation and ionization. The maximum energy of the electron spectrum increases with the maximum energy of the beam of incident photons. The range of the secondary electrons in the absorber depends on both their energy and the electron density of the medium through which they travel. The transfer of this energy to the medium is called the absorbed dose (or dose).

In the absence of photon attenuation, the kerma is constant with depth. The dose, on the other hand, initially increases with depth, reaching a maximum at a

depth equal to the maximum range of the secondary electrons. This depth is referred to as the depth of maximum dose. At this depth, there is electronic equilibrium as the same number of electrons are set in motion and stopped in the same volume element. Under these conditions, the dose is equal to the kerma.

In an actual situation in which the attenuation of the photon beam is significant, the kerma decreases exponentially from the surface with increasing depth. On the other hand, the dose initially increases and reaches a maximum with increasing depth. This depth, which is near to but less than the maximum range of the electrons, is referred to as the depth of maximum dose. Beyond this depth, the dose, though slightly greater than the kerma, also decreases exponentially with depth [62]. At the point where the dose is equal to the kerma, quasi-electronic equilibrium is said to exist because the number of electrons stopped at this point is not exactly equal to the number that are set in motion at the same point. That is, there is no true electronic equilibrium at any point in a medium irradiated with high-energy beams [62].

The depth of maximum dose increases with the beam energy. This depth approximates 0.5, 1.5 and 5.0 g/cm^2 for Co-60, 6- and 31-MV x rays respectively [62]. The region between the surface and the depth of maximum dose is referred to as the buildup region and is a region of

electronic disequilibrium.

1.2 Clinical Implications of Beam Penumbra

The object of radiation therapy is to deliver a uniform or homogeneous dose to the tumour volume and negligible dose to the normal surrounding tissues. In practice, however, the normal tissue is often given a biologically significant dose. The tissue sensitivity, which varies with cell type, determines the radiation damage. The radiosensitivity of cell types is expressed in terms of the "mean lethal dose", which is the dose that will kill (1/e) of the cell population. [48]

Among the highly sensitive cell types are the cells of the bone marrow, the lining of the gastrointestinal tract, the lens of the eye, and the reproductive organs. Since these cell types have low mean lethal dose, a modest dose causes appreciable damage to them and impairs the normal function of the host organs. Therefore, in radiotherapy treatments where any of these organs reside in the periphery of the tumour volume, care must be taken to keep the dose to these sensitive organs below the threshold that will cause irreparable damage. When excellent localization and reproducible treatments are possible, a knowledge of the penumbral distributions becomes important.

A knowledge of the dose distribution can also be important for insensitive tissues such as the spinal cord. These cell types are non dividing and therefore lack the ability to repair any radiation damage [48]. Radiotherapy of the spinal cord often involves a dose of about 4000 to 4500 cGy which is then supplemented with a boost to the smaller volume involving the primary tumour [26,34]. Since the spinal cord has received nearly a tolerance dose, a small boost, if delivered to the spinal cord, can cause paralysis. In a similar manner, irradiation of the eye lens can produce cataract and irradiation of the reproductive organs can lead to gene mutation and in severe cases to sterility. Irradiation of the bone marrow and other blood forming organs can lead to anaemia and possible death while irradiation of the lining of the gastrointestinal track (GIT) can lead to vomiting, infection and possible death.

These areas of radiation damage indicate the importance of an accurate determination of the dose distribution in the penumbral region in order to avoid overexposure to these radiosensitive organs. Dutreix [36], in 1976, emphasized a sharp cutoff of the beam is important in order to spare critical organs that may be close to the target volume. Pla et al [88], in 1981, considered the importance of an accurately determined penumbral distribution in the irradiation of tumours near the lens of the eye, the central nervous system and the bone marrow. These are some

of the areas where a sharp cut-off of the beam is an advantage. It must be emphasized however, that a sharp cut-off is not always an advantage. When adjacent parallel-opposed fields are matched, sharp penumbral distributions result in high- or low-dose regions when only a small error is made in the spacing between the fields. [1,27,35]

It is equally as important to deliver a uniform dose to the tumour volume as it is to spare the normal tissues that surround it. Although the tumour volume may be within the nominal beam width (the region YY' in Figure 1.1), the tumour dose will be non uniform if parts of it are in the penumbral region (region XY and X'Y'). If the penumbral dose distribution is very broad or if heterogeneities are involved, parts of the tumour volume can be underexposed. This situation can only be avoided if the penumbral dose distribution is accurately known for the prevailing situation.

The irradiated patient, unlike the water phantom, is heterogeneous in composition. Kornelsen and Young [66] indicated that the dose distribution around and beyond the beam edge is expected to change from one medium to another. If for example a soft-tissue/lung interface exists at the edge of a high-energy beam, more electrons, set in motion in the soft tissue, deposit energy in the lung region than vice versa. Moreover, the electrons will travel farther in

the low-density lung than in the soft tissue [66]. This leads to a difference or discontinuity in the dose distributions in the interface region. Thus, electronic disequilibrium associated with regions of low density can be a significant factor in radiotherapy treatment. A treatment regime that would normally deliver a uniform dose to a tumour volume in a homogeneous environment can result in a non uniform dose or underexposure when the tumour volume is located near a low-density medium such as the lung. This is due to the loss of dose to the tumour volume as a result of electronic disequilibrium. This situation must be considered carefully in radiotherapy treatment.

1.3 Review of Beam Penumbra

With the recent improvements in computerized treatment planning using computerized tomographic (CT) data, it has become more practical to optimize dose distributions in radiotherapy. One area which has been neglected in this regard, however, is the penumbral region. Although beam penumbra have been measured with dosemeters of different geometric configurations and types [23,43,47,49,63,87,88], it is only recently that any effort has been made to consider the significance of these measured penumbral distributions.

Johns and Darby [63], in 1950, first emphasized the importance of the chamber diameter on the dose distribution at the beam edge. Sometime later in 1957, Greene [46] calculated that an accurate penumbral distribution is not obtained if the diameter of the ionization chamber exceeds the penumbral width. Later in 1962, Greene [47] used ionization chambers of 0.3-cm and 0.6-cm inside diameter to examine the penumbra of a 300 kVp x-ray beam in air and in water, and of 4- and 20-MV x-ray beams in water. He concluded that a 0.6-cm ionization chamber could resolve the dose distribution across the edge of both conventional and megavoltage x-ray beams in a scattering medium. Greene stated that the effect of scatter permits the use of ionization chambers that have inside diameters equal to twice the width of the geometric penumbra corresponding to in-air measurements.

Dutreix et al [36], in 1965, indicated that electronic equilibrium is achieved at a point in a medium irradiated by x or gamma rays, only if, in a radius equal to the maximum range of the secondary electrons, both the photon field is uniform in intensity and the medium is homogeneous. The beam edge is therefore a region of electronic disequilibrium. Similarly, an interface between media of different electron densities constitutes a region of electronic disequilibrium. Electron fluence effects in such regions are not considered in the present dose calculational models.

Dutreix, Dutreix and Tubiana [36] defined the influence function which expresses the contribution of the interactions at one point to the dose at another point as a function of the distance and angle between the two points. The integral of the influence function in the volume of radius equal to the maximum range of the secondary electrons surrounding the point is the dose at the point. The influence function calculated for 20-MV x rays indicated that the contribution from the vicinity of the point has a much greater effect on the dose at that point than the more distant regions of the electronic equilibrium volume. This suggests that the practical equilibrium volume for penumbral measurements is considerably smaller than the true equilibrium volume.

Dutreix [35], in 1976, linked the variation in the dose distribution in the penumbral region with a lack of lateral electronic equilibrium. She also determined experimentally that the penumbral width increased from 0.5 cm for 6-MV x rays to 2.0 cm for 20-MV x rays.

Patterson and Shragge [87], in 1981, found some degradation in the penumbral width in an 18 MV photon beam with increasing depth using a PTW ionization chamber (I.D.=0.35 cm). This was attributed to the increased contribution of the phantom scatter. They suggested that Compton scattered electrons from the collimator caused some penumbral degradation in the buildup

region.

Pla et al [88], in 1981, used a Farmer ionization chamber (I.D.=0.6 cm) and thermoluminescent crystals to measure the beam profiles for Co-60 (Theratron 780), 4-MV x rays (Therapi 4 linac), and 10-MV x rays (Clinac-18). They reported good agreement between the two dosimetric systems but gave no indication of the geometric configuration of the thermoluminescent dosimeters.

Scarpa et al [93], in 1979, used LiF thermoluminescent dosimeters of dimensions 0.32 x 0.32 x 0.07 cm to measure the dose profile at the edge of a 250 kV x-ray beam in small experimental animals. They indicated that this system gave high spatial resolution.

Chan et al [23], in 1973, used a silicon diode to measure the dose distribution across beams from several megavoltage machines of radiation qualities ranging between Co-60 and 25-MV x rays. Their results indicated that Co-60 units have a much broader penumbra than do accelerators and that the penumbral widths of the accelerators decreased slightly with increasing energy. This result disagreed with the ionometric measurements of Dutreix [35].

Nath et al [81], in 1981, used a diode detector and treatment verification film to measure the penumbral dose distribution for small x-ray fields from a modified 4-MV

linac. They found that the penumbral width was improved with the use of trimmers. They did not compare the results of the two different dosemeters.

Grant III et al [43], in 1978, exposed film to adjacent fields of Co-60 and 6-MV x rays to study their penumbra. They concluded that the penumbra for the 6-MV x rays is slightly superior to that of Co-60.

Kornelson and Young [67], in 1982, used verification film to determine beam profiles in materials of different density. They found that for large fields the penumbral width increased from 1.0 cm in unit-density material to about 2.8 cm in balsa wood (electron density relative to water = 0.162). This degradation of dose was attributed to the greater electron ranges and the increased lateral spread of the secondary electrons in the low-density material.

The work of Harper [49], in 1982, coincided in time with that of Kornelson and Young, and is the most systematic study of beam penumbra undertaken to date. He recognized that two distributions exist in the penumbral region and that different dosemeters measure different distributions. Using two commercial ionization chambers, a PTW ionization chamber (I.D.=0.35 cm), a Farmer ionization chamber (I.D.=0.61 cm) and a solid state diode (sensitive diameter = 0.14 cm), he measured the penumbral

distributions for photon beams from a Co-60 unit (AECL Theratron 780), a 6-MV linac (AECL Therac 6) and a 31-MV betatron (Brown Boveri Asklepitron 35). He considered the origins of the secondary electrons that contribute to the response of the detector and introduced the concept of an effective diameter for ionization chambers. The diode-measured penumbral distributions were sharper than those of the ionization chambers for all energies. The difference, however, increased with the beam energy.

1.4 Project Objective and Scope of Thesis

The primary objective of this project is to determine the impact of the lateral spread of the secondary electrons on the penumbral dose distributions of high-energy radiotherapy beams. The work by Kornelsen and Young [67] indicated that the lateral spread of the secondary electrons caused the width of the penumbral distributions to increase with energy and to decrease with increasing electron density. This work has extended our understanding of these early results.

In this project, the effect of the lateral spread of the secondary electrons on the penumbral dose distributions is determined as a function of both the beam energy and the electron density of the medium of interaction. Both

experimental and theoretical approaches are employed. The experimental approach has involved a detailed study of the effect of the detector configuration and type on the measurement of penumbral distributions for high-energy x-ray beams. The results have lead to the measurement of penumbral distributions not previously measured. A penumbral model is adopted which considers the different penumbral distributions and associates the differences directly with the lateral spread of the secondary electrons.

The theoretical approach has involved the determination of dose spread functions which are similar to dose spread arrays [16,73,75]. The dose spread functions or kernels are based on the physical interaction processes of x rays with matter and follow the resulting secondary electrons through ionization chambers of varying inside diameter and wall materials. Convolution methods are employed to study theoretically the effects of the inside diameter of the ionization chamber, the wall material of the ionization chamber and the beam energy on the resultant penumbral primary dose distributions.

In Chapter II, the experimental techniques are discussed. This includes the radiation detectors used for the measurements, the scanning method and the physical characteristics of the radiotherapy machines.

In Chapter III, the theoretical background for the project is discussed. This includes a discussion of the aspects of cavity theory relevant to penumbral measurements. A penumbral model is introduced and the use of convolution techniques in the theoretical determination of penumbral dose distributions is discussed.

Chapter IV presents the experimental results of the penumbral measurements for Co-60, 6- and 31-MV x rays. The effect of the lateral spread of the secondary electrons on the penumbral distributions is investigated as a function of the beam quality and the electron density of the medium of interaction. The primary penumbral dose distributions in soft tissue (simulated with lucite), in lung (simulated with cedar and balsa) and in a high-density medium (copper) are determined ionometrically. A second penumbral distribution is also determined for the three radiation qualities. These penumbral distributions are used to consider the effect of the lateral spread of the secondary electrons on the penumbral dose distributions.

The theoretical results are presented in Chapter V. Parameters associated with the penumbral dose distributions obtained by the convolution technique are compared with those obtained by the ionometric measurements. Idealized distributions and kernels are used to test the convolution technique and the penumbral model.

The theoretical and experimental results are discussed in Chapter VI in the light of the penumbral model. The differences between theory and experiment are discussed.

CHAPTER II

EXPERIMENTAL TECHNIQUES

2.1. The Radiation Detectors

Specially built cylindrical ionization chambers were used for measurements in this project. These chambers were designed to investigate the effect of the detector type and configuration on the penumbral distributions of high-energy beams and thereby obtain accurate measurements of the penumbral distributions.

Standard commercially-available ionization chambers such as the PTW (Physikalish-Technische Werkstaten) and Farmer chambers have inside diameters of 0.35 and 0.6 cm respectively. In regions of large dose gradients (e.g. the penumbral region) these diameters can be too large to resolve the distributions properly [47,62]. In this project, the effect of chamber inside diameter has been studied extensively using inside diameters from 0.3 to 1.4 cm.

The commercial ionization chambers are supplied with walls of tissue-equivalent materials (i.e. approximately 1.0 g/cm^3). However, other detector types (e.g. diodes, films and thermoluminescent dosimeters) involve materials of high electron density and atomic number. In regions of high-dose gradient, the behaviour and characteristics of

these systems have not been clearly delineated. These effects have been considered by varying the electron density of the wall material from 0.16 to 7.35 relative to that of water. The chamber wall materials included lucite (1.15), cedar (0.32), balsa (0.16) and copper (7.35).

The ionization chambers, used in this project, were designed to fit onto the stem of a standard Farmer chamber. The tufnol thimble chamber (graphite coated) and dielectric support were removed. A replacement lucite support was designed to extend 0.6 cm beyond the end of the metal sleeve leaving 1.6 cm of the original central electrode exposed. The outer diameter of the lucite support was reduced in two steps, each of 0.25-cm length, onto which the walls of the replacement chambers were a press-fit. The supporting surfaces and the inner surface of the non-conducting chamber walls, shown in Figure 2.1, were coated with aquadag to maintain electrical continuity with the metal sleeve. (Aquadag is a suspension of graphite particles in water. When the water evaporates, it leaves behind a thin layer of conducting graphite to form the outer electrode of the chamber.) For each inside diameter and wall material, there were three chamber-wall thicknesses, corresponding to the electronic equilibrium depths of 0.5, 1.5 and 5.0 g/cm^2 for Co-60, 6- and 31-MV x rays respectively.

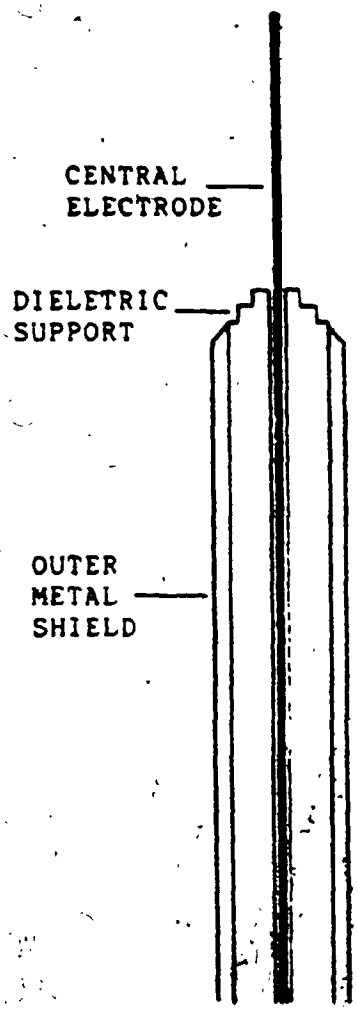

Fig. 2.1a

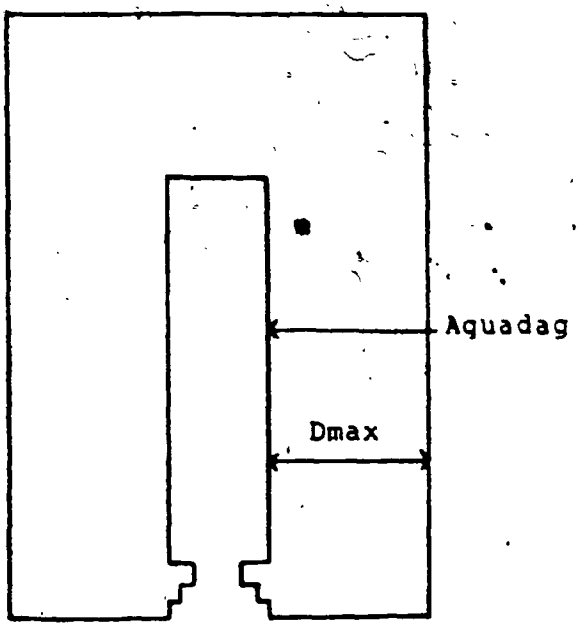

Fig. 2.1b

Figure 2.1: An Illustration of (a) the Redesigned Stem and (b) the Chamber of the Cylindrical Farmer Ionization Chamber.

The properties of some commercially-available detection systems were also studied including a Nuclear Associates silicon diode (sensitive diameter = 0.14 cm), a PTW ionization chamber (I.D.=0.35 cm), and a Farmer-type ionization chamber (I.D.=0.61 cm).

2.2 Detector Characteristics

A number of characteristics of the radiation detectors are important in the assessment of their ability to measure the penumbral distribution. These include the dependence of the detector response on the beam quality, the doserate (ion recombination), the rotation about the axis of the detector and the precision of the radiation detector.

In order to test the dependence of the detector response on quality, each detector was irradiated with Co-60, 6- and 31-MV x-ray beams and the detector response was normalized to that of a standard Farmer chamber under identical conditions. The quality dependence of the Farmer chamber, based on a National Research Council calibration, was 5.5% lower for 250 kV x rays than for Co-60. For all higher photon energies, only a modest dependence on beam quality is expected. The results of the measurements indicated that the response of the chambers normalized to that of a standard Farmer chamber, was independent of beam quality within a few percent for beam qualities from Co-60 to 31-MV

x rays. Similarly, the diode response, normalized to that of the Farmer chamber, indicated that the diode response was similarly independent of beam quality for the same beam energies. Since the diode is shielded, this reduced quality dependence is expected [41,115]. These results agree with those of Harper [49] who tested the same diode for quality dependence using beams from 250-kV to 32-MV x rays. The results also agree with those of Gray [44] who found that the off-axis and depth dose response of a similar diode was within 2% of that of an ionization chamber for Co-60 and 4-MV x rays.

In a typical penumbral measurement, the doserate varies by more than a factor of ten. Further, the output of the accelerators are pulsed while the Co-60 output is steady. It is important that the response of the detector remains linear with doserate for these varying conditions. To test the linearity of response with doserate, each detector was placed in the 6-MV x-ray beam of the Therac 6 at source-detector distances ranging from 100 to 300 cm. For a doserate range from 250 to 2.5 cGy per minute, the diode and ionization responses remained linear. The calculated recombination in the 0.3 to 1.0 cm inside diameter ionization chambers caused less than 0.5% current loss at these doserates [13,14]. However, the current loss due to recombination increased rapidly with the chamber inside diameter and amounted to 5% for the 1.4 cm inside diameter chamber for the 6-MV x-ray beam. The effect of doserate on

the measured penumbral widths, however, is expected to be small. The diode results agreed with the 4-MV x-ray measurements by Gray [44] which showed that the diode response was independent of doserate.

All the radiation detectors were irradiated side on with their axes perpendicular to the axis of the beam. Gray [44] has reported that the diode detector showed no dependence on rotation about its axis when irradiated in this geometry. The ionization chambers employed in this project are cylindrically symmetric about the long axis of the chamber. Hence, no dependence on rotation about their axes is expected.

The radiation detectors have a small response even if no radiation impinged upon them. This leakage current must be subtracted from the measurements made with each detector. The leakage current was larger for the diode detector than for the ionization chambers. The leakage current for each detector remained constant within 2% throughout a penumbral measurement and was never more than 5% of the total detector response. The coefficient of variation of the response of the dosemeters at the isocentre of the Co-60 and 6-MV x-ray units was about 0.5% and was slightly higher for the 31-MV x-ray unit.

When the ionization chambers and the diode detector were used for penumbral measurements, the precision of the radiation detector depended on the detector characteristics, the precision of the scanning system and the variation of the machine parameters. The standard deviation of the P20-80 and P10-90 penumbral widths was +/-0.03 and +/-0.07 cm respectively.

2.3 The Scanning Method

Each detector was mounted on a screw thread of 0.5-cm pitch and was driven by a stepping motor with a single-step capability of 0.01 cm. The axis of the detector was perpendicular to the central axis of the beam. The detector was moved incrementally across a principal axis at the isocentric distance. The output of the detector was connected to a Keithley 610C electrometer with a digital readout. All measurements were taken in air with equilibrium caps using a square field of 10-cm side length at the isocentre.

In measuring a beam profile, a fixed number of monitor units was used for each point of measurement. The number of monitor units was increased for chambers of small inside diameter to maintain the measurement precision. The variation of the chamber response at the isocentre during one beam profile measurement was less than +/-0.5% for both the Co-60 unit and 6 MV linac, and less than +/-1% for the

betatron. Repeat readings were taken at the position of the central axis to eliminate systematic drift in both the electrometer and the machine outputs. About thirty measurement points were taken for each beam profile with steps as small as 0.2 mm in the penumbral region. The detector response at each measurement point was normalized to the central axis response.

Since preliminary measurements established the symmetry of the beam about the central axis, the beam profiles were determined from the central axis to one beam edge only. For purposes of this study, data are indicated for one plane only, although comparable data were determined in the perpendicular planes.

2.4 The Radiation Therapy Machines

The radiotherapy machines for which the penumbral distributions were investigated were a Co-60 unit (an AECL Theratron 780), a 6-MV linear accelerator (an AECL Therac-6) and a 31-MV betatron (a Brown Boveri Asklepitron 35). The isocentres of the Co-60, 6- and 31-MV therapy units are located at 80, 100 and 110 cm from the source respectively. The collimator configurations for the Co-60 unit and 31-MV betatron are illustrated in Fig 2.2 while that for the Therac-6 has been shown earlier in Figure 1.1.

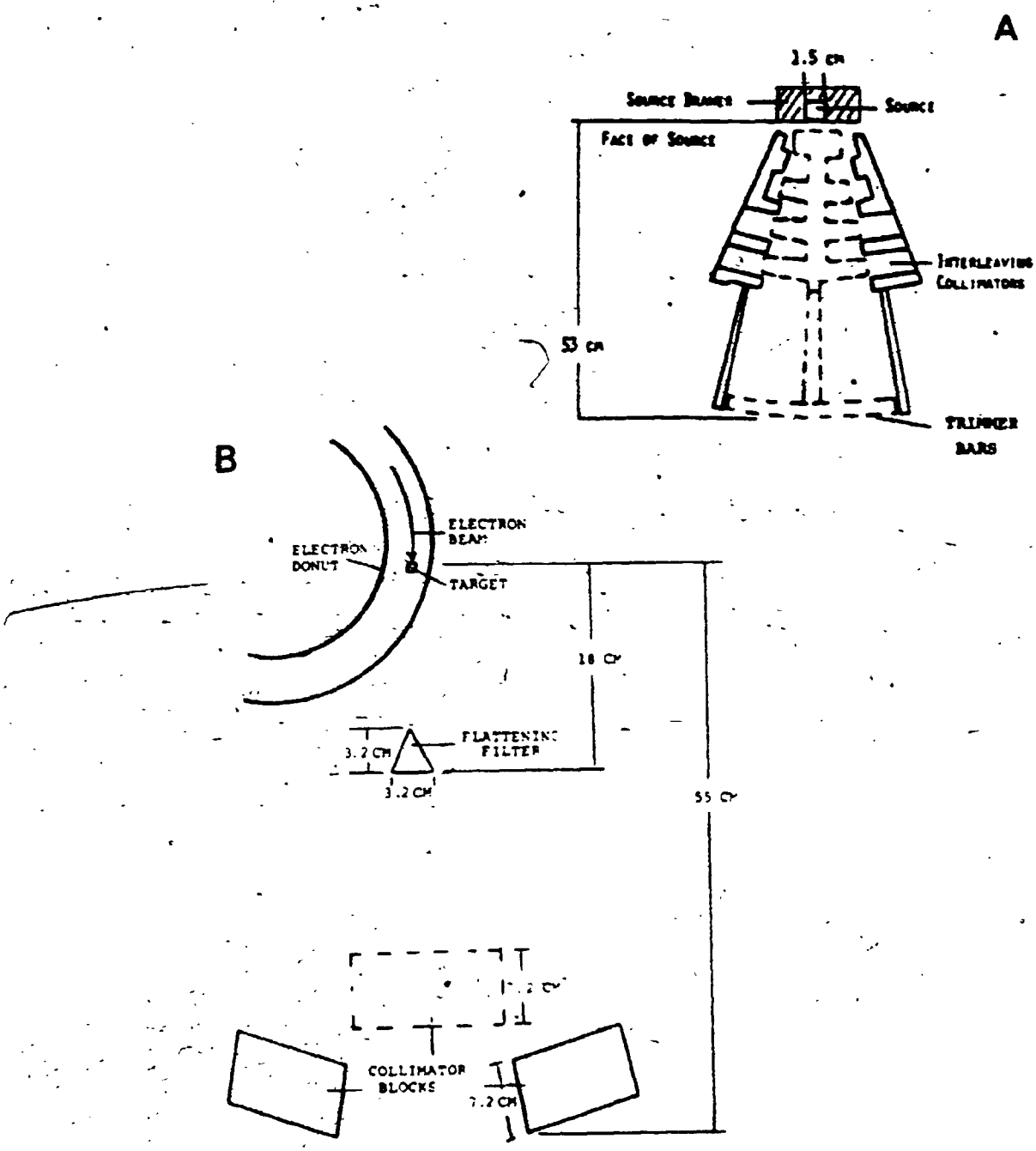

Figure 2.2: The Source-Collimator Arrangement for the High-Energy External Beam Radiotherapy Machines. (a) The Theratron 780 (a Co-60 unit); (b) The Asklepitron 35 (a 31-MV betatron).

The collimator blocks limit the field size of the x-ray beam and attenuate the beam to safe levels beyond the field size. In all three machines, the collimators are moved in such a way that their leading edge is parallel to the diverging rays of the therapeutic beam. The Co-60 unit has an additional set of trimmers located at 53 cm from the source as a final limiting device.

The penumbral distribution for any radiotherapy unit is dependent on the effective source diameter. The effective source diameters vary considerably for the units employed in these measurements. The Co-60 source has a 1.5-cm diameter while the source diameters for 6- and 31-MV x rays are less than 3 and 1 mm respectively. Since the bremsstrahlung radiation from the accelerators is strongly forward-peaked, significant attenuation on the central axis is required to flatten the beam distribution for clinical use. This forward peaking increases with energy and hence attenuation of the central axis dose increases with beam energy. This beam flattening is expected to result in a broadening of the effective source size for accelerators and the broadening should increase with energy. The effective source diameters for the accelerators are still much smaller than that for Co-60.

2.5 Determination of the Penumbral Distribution

2.5.1 Introduction to the Ionometric Technique

Many authors have recognized the clinical importance of an accurate dose distribution in the penumbral region [22,39,50]. Although dosemeters of different configurations and types have been employed for penumbral measurements, little consideration has been given to the effect of these parameters on the accuracy of the measured distributions. In this work, these factors have been considered and have indicated that many published penumbral distributions are in error. The methods, introduced in this project, permit more accurate determination of the penumbral distributions and clearly indicate the shortcomings of some earlier measurements.

A radiation detector is normally introduced into a medium to determine the dose at a point in the medium (normally the centre of the detector). The ICRU definition of dose and the Bragg-Gray theory require a small cavity dimension. The mass of the medium displaced by the cavity must be sufficiently small both that the dose can be defined at a point and that the electron energy spectrum in the medium (resulting from photon interactions in the medium) is not modified by the presence of the cavity [13,62]. However, cavities of small dimensions are both difficult to manufacture and have a decreased signal

to noise ratio. A high signal to noise ratio is important for measurements in the penumbral region due to the significant change in the magnitude of the signal. These conditions result in a minimum practical cavity size for dose determinations in the penumbral region.

When a chamber of finite cavity size is introduced into a medium, the chamber response is averaged over the entire volume of the chamber cavity. In a region of large dose gradient such as the penumbral region, this dose averaging results in the degradation of the measured dose distribution [62]. The magnitude of this effect is expected to increase with the cavity size and must be eliminated to determine an accurate penumbral dose distribution.

Orchard [84] introduced the decrement line to describe the dose distribution at depth in a phantom for high-energy x-ray beams. The decrement line defines the location of points representing percentages of the central- axis dose at the same depth. The penumbral widths at any depth can be obtained from the decrement lines. In a similar way, if the dose levels are normalized to 100% on the central axis, the separation between pairs of dose levels on the same side of the central axis can be referred to as a penumbral width. For example, the separation between the 10% and the 90% dose levels is called the P10-90 penumbral width.

Similarly, a number of such penumbral widths were determined for various dose levels.

2.5.2 The Penumbral Dose Distribution

Lucite has been used to simulate soft tissue. The penumbral widths associated with distributions, measured with chambers of varying inside diameter, can be extrapolated to zero inside diameter to remove the effect of the chamber inside diameter. A series of extrapolated penumbral widths such as P50-90, P50-80, P50-20, P50-10, etc, for ionization chambers constructed of lucite walls can then be used to determine the penumbral dose distribution in soft tissue. For ionization chambers with tissue-equivalent walls, this approach results in an improved penumbral dose distribution in soft tissue.

Similar measurements of the penumbral distributions were made with ionization chambers constructed with walls of lung-equivalent media. A similar extrapolation of the measured penumbral dose distributions for these lung-equivalent walls results in the penumbral dose distribution in lung. The electron density of healthy lung relative to that of water varies between 0.084 and 0.40 [103]. In this project, cedar (0.32) and balsa (0.16) were used to simulate lung. Van Dyk et al [103], using CT numbers, reported that the average electron density of

diseased lung varied widely from the average relative electron density of 0.25 for the healthy lung. When copper-wall ionization chambers are used, the result is the penumbral dose distribution in a high-density medium. This ionometric technique has been introduced for the determination of improved penumbral dose distributions of high-energy x-ray beams. This method can be extended to any energy, field size and depth in a phantom.

CHAPTER III

THEORY

3.1 Relevant Cavity Theory

The introduction of a radiation-sensitive device into a medium to measure the energy absorbed per unit mass (i.e. the dose) constitutes a discontinuity because the device normally differs from the medium in both atomic number and density. This discontinuity is generally referred to as a cavity. The cavity can be in the solid, liquid or gaseous phase and can be more or less dense than the surrounding medium. Cavity theory relates the energy absorbed in the cavity to the energy absorbed in the medium for cavities of different size.

In the treatment of cavity theory, the dimensions of the cavity are related to the range of the secondary electrons. If the cavity size is small with respect to both the range of the electrons liberated in the medium and the photon mean free path, photon interactions inside the cavity are negligible and the dose in the cavity is due to electrons produced in the medium surrounding the cavity. Under these conditions, the dose in the medium D_m, is related to the

dose in the cavity, D_c, by the ratio of the mass collisional stopping powers, $\bar{S}$, in the form

$$\frac{D_m}{D_c} = \bar{S}^{\,medium}_{cavity} \qquad (3.1)$$

where the mass collisional stopping power ratio is averaged over both the photon and electron spectra in the medium [62].

Equation 3.1 is the Bragg-Gray relation [20]. Such a cavity is an electron detector and fulfils the conditions of a Bragg-Gray cavity. The upper limit to the dimensions of a Bragg-Gray cavity is set by the cavity theory while the lower limit is set by mechanical and electrical stability and chamber sensitivity. For a cavity of zero dimensions, the dose in the cavity is equal to that in the medium. This concept was employed in the determination of the penumbral dose distributions of high-energy photon beams.

For large cavities, the range of the electrons liberated in the cavity is small with respect to the dimensions of the cavity. In this case, the electrons that contribute to the dose in the cavity result from photon interactions that occur within the cavity. The dose in the medium, D_m, surrounding the cavity is then related to that in the cavity, D_c, by the ratio of their mass energy absorption

coefficients ($\bar{u}_{en}/\rho$) in the form:

$$\frac{D_m}{D_c} = \frac{[\bar{u}_{en}/\rho]_{medium}}{[\bar{u}_{en}/\rho]_{cavity}} \qquad (3.2)$$

where the mass energy absorption coefficients in both the medium and the cavity are averaged over the photon spectra in the medium and the cavity respectively.

Since the diameter of an air ionization chamber corresponding to a large cavity would be several meters, large cavities are normally of media of high-electron density. Such a high-electron density cavity is a photon detector with the detected photons interacting within the cavity. The cavity measures the energy transfered from the photons to the kinetic energy of the secondary electrons in the medium of the cavity or kerma. This concept was employed in the determination of the penumbral photon-fluence distributions of the high-energy photon beams.

If a beam of monoenergetic photons of energy $h\nu_o$ interacts in a medium, the kerma, K, is related to the photon fluence, Φ, by:

$$K = \Phi . (u_{en}/\rho) . h\nu_o \qquad (3.3)$$

where (u_{en}/ρ) is the mass energy absorption coefficient for the medium [16,17,62]. In this case, the relative

kerma and photon-fluence distributions are equivalent. For a heterogeneous photon beam with a spectrum of photon energies described by $d\Phi(h\nu)/dh\nu$, the kerma is given by [62]:

$$K = \int_0^{h\nu_{max}} \frac{d\Phi(h\nu)}{dh\nu} \cdot \left(\frac{\mu_{en}(h\nu)}{\rho}\right) \cdot h\nu \, dh\nu \qquad (3.4)$$

In a region where the positional dependence of the photon-energy spectrum is limited, the kerma and the photon-fluence distributions are equivalent.

For intermediate cavity sizes, the dose in the cavity results from a combination of photon interactions in both the medium and the cavity. Hence, the cavity is neither a true electron nor a true photon detector.

It should be noted that the cavity for an ionization chamber is a gas-filled space surrounded by a solid medium. For photon energies in excess of 1 MeV, dimensions of the order of 1 cm at atmospheric pressure fulfil the Bragg-Gray conditions [20]. A solid or liquid cavity with a density approximately 1000 times that of air and must have linear dimensions of about 10^{-3} times that for air to fulfil the size requirement for the application of the Bragg-Gray theory. Since this dimension is exceeded by shielded solid state diodes, they do not satisfy the Bragg-Gray relation.

3.2 The Penumbral Model

The x or gamma ray beam from a radiotherapy unit is associated with the source-collimator configuration of the unit. The spatial variation of this beam can be described in terms of a photon-fluence distribution where the photon fluence is defined as the number of photons incident from all directions at a point of interest per square cm of area perpendicular to the direction of each photon [56]. A radiotherapy unit with a small source diameter, such as the betatron with a focal spot less than 1 mm in diameter, produces a beam with a sharp primary penumbral photon-fluence distribution. On the other hand, a Co-60 unit, housing a source of 15-mm diameter, produces a significantly broader primary penumbral photon-fluence distribution.

The interaction of this photon-fluence distribution with a medium results in the production of secondary electrons. For measurements in air, the medium is supplied by the wall of the ionization chamber and its buildup cap. The energy deposited by the secondary electrons per unit mass of the cavity is then related to the dose in the surrounding medium by the cavity theory. This energy deposition results in a second distribution in the penumbral region, namely the dose distribution which is of direct interest in

radiotherapy. The finite range and lateral spread of the secondary electrons result in a dose distribution in the penumbral region, which, in all cases, is either broader than or equivalent to the corresponding kerma or photon-fluence distribution.

For low-energy x-ray beams, the range of the secondary electrons produced in photon interactions approaches zero and the penumbral photon-fluence and dose distributions have equivalent shapes. For energies in excess of 1 MeV, the range of the secondary electrons is significant and the dose distribution is broader than the corresponding photon-fluence distribution. Although the angular distribution of the secondary electrons becomes increasingly forward-peaked with increasing photon energy above 1 MeV [37,38], the increased range of the secondary electrons has been shown to result in a further increase in the lateral spread [67 73,74]. The difference between the width of the penumbral photon-fluence and dose distributions is then expected to increase with energy above 1 MeV.

The measurement of the penumbral dose distribution in a tissue-equivalent medium (usually a water phantom) is undertaken routinely using radiation detectors of different types and configurations [23,35,43,47,62,63,82 87,88]. In

order to measure this distribution correctly, it is necessary to use an electron detector fulfilling the Bragg-Gray conditions. Further, if one is interested in the distribution corresponding to a tissue-equivalent medium, the material of the detector must be tissue equivalent.

In media of low-electron density such as lung, the range and the lateral spread of the secondary electrons are increased [67]. This results in a further broadening of the penumbral dose distribution with respect to the photon-fluence distribution. In order to measure this distribution correctly, the walls of the ionization chambers must be constructed of lung-equivalent media. Such ionization chambers must be specially designed since the commercially-available ionization chambers have tissue-equivalent walls.

Finally, the configuration of the detector must be considered. In regions of large dose gradient such as the penumbral region of high-energy photon beams, dose averaging due to the finite dimensions of the detector results in artificial flattening of the penumbral distribution [62,63]. A detector of small dimensions is therefore required to measure the penumbral distribution correctly. In situations where this is not practical, the

measured distribution must be corrected for the dimensions of the detector. In the case of ionization chambers, the measured distribution must be corrected for the inside diameter of the ionization chamber.

In regions of limited positional dependence of the photon energy spectrum, it has been indicated both that the response of photon detectors is a measure of the kerma and that the kerma is related directly to the photon fluence. For accelerators in which the x-ray beams are produced in the bremsstrahlung process, Mohan et al [80], using a Monte Carlo calculation, have shown that the mean energy of the photon beam decreases modestly with increasing distance from the central axis. For measurements in air, however, the photon-fluence penumbra from accelerators is sufficiently narrow that the positional dependence of the photon-energy spectrum across the penumbra is limited. For the Co-60 unit, the photon-fluence penumbra is much broader but the photon-energy spectrum has a smaller positional dependence. This limited dependence of the photon-energy spectrum across the penumbral region for measurements in air results in equivalent kerma and photon-fluence distributions. The use of an appropriate photon detector then enables the measurement of the penumbral kerma or photon-fluence distribution. This distribution has not previously been detected.

For wall materials of high-electron density, the range and the lateral spread of the secondary electrons are decreased. The difference between the penumbral photon-fluence and dose distributions then decreases. In the limit of infinite electron density, the range of the secondary electrons is reduced to zero and the penumbral photon-fluence and dose distributions are equivalent. In this project, the concept of zero lateral electron spread in a medium of infinite electron density is used to design appropriate photon detectors for the measurement of the penumbral photon-fluence distributions of high energy radiotherapy photon beams.

3.3 Theoretical Dose Calculation in a Phantom

3.3.1 Monte Carlo Method

Several authors [9,73,91,106,107,108,111] have used the Monte Carlo method to calculate the dose distribution under varying condrtions and geometries. In a typical photon-transport Monte Carlo model, the histories of approximately 10^5 photons [9,22] are followed to obtain the dose distribution in the entire phantom. Since 20 to 30 Compton scattered events reduce the energy of a photon from

several MeV down to 50 keV [9] it is relatively simple to follow photon histories. These calculations, however, suffer from two main drawbacks. First, they are very time consuming and second, electron-fluence effects are not taken into consideration. The photon transport calculation technique is not accurate in the buildup region, in the build-down region, in regions of inhomogeneities, and in the penumbral region of high-energy photon beams.

These electron-fluence effects can be considered with the use of the electron transport Monte Carlo calculation; however, the number of electron interactions is enormous. In order to reduce the required amount of computation in a typical electron-transport Monte Carlo calculation, the complete description of the charged-particle histories is abandoned and snapshots are taken at various times during the particle history [9]. A condensed history is sampled by letting the particle carry out a random walk in which each step takes into account the combined effect of many collisions.

The Monte Carlo model has seen limited use [16,72] in regions of varying photon fluence such as the beam edge of high-energy radiotherapy machines. The measurement of the penumbral photon-fluence distribution, introduced in this project, allows the extension of Monte Carlo calculations

to the penumbral region of high-energy radiotherapy photon beams.

3.3.2 The Convolution Technique

In this method, the dose distribution is calculated by convolving the photon-fluence distribution with an appropriate kernel. Mackie et al [75] used Monte Carlo techniques to determine the three-dimensional spatial distribution of energy deposited by secondary electrons and positrons which spread from the site of photon interactions. This was termed the dose spread array. They used this three-dimensional dose spread array as the kernel in a convolution integration to produce a three-dimensional dose distribution. The primary dose distribution is obtained when the primary photon-fluence distribution is convolved with the primary dose spread array [73,75].

The primary dose spread array (or electron transport kernel) is characteristic of the beam energy and the electron density of the medium in which the interactions occur. Since the range and the lateral spread of the secondary electrons increase with photon energy and with decreasing electron density, the dimensions of the primary dose spread array correspondingly increase [75].

Two methods can be used to determine the primary dose spread array or kernel. In the first method, incident photons are forced to interact in a voxel element of the phantom. This voxel, termed the interaction voxel, is surrounded by other voxels extending to at least the maximum range of the secondary electrons. The dose distribution, deposited by secondary electrons in this array of voxels, is called the primary dose spread array. This approach, termed the interaction point of view, is illustrated in Figure 3.1a.

In the second method, termed the dose deposition point of view, the dose at a single point or voxel is determined. This voxel, located at the origin of a cartesian coordinate system is surrounded by other voxels extending to at least the maximum range of the secondary electrons in the medium. The dose deposited in the dose deposition voxel, as a result of equal numbers of primary interactions occurring in each voxel, is determined in turn. This is illustrated in Figure 3.1b. These individual dose contributions are then normalized to the total dose deposited in the dose deposition voxel to obtain the primary dose spread array. The dose spread array obtained via the interaction point of view and the dose deposition point of view are, however, equivalent [73,75].

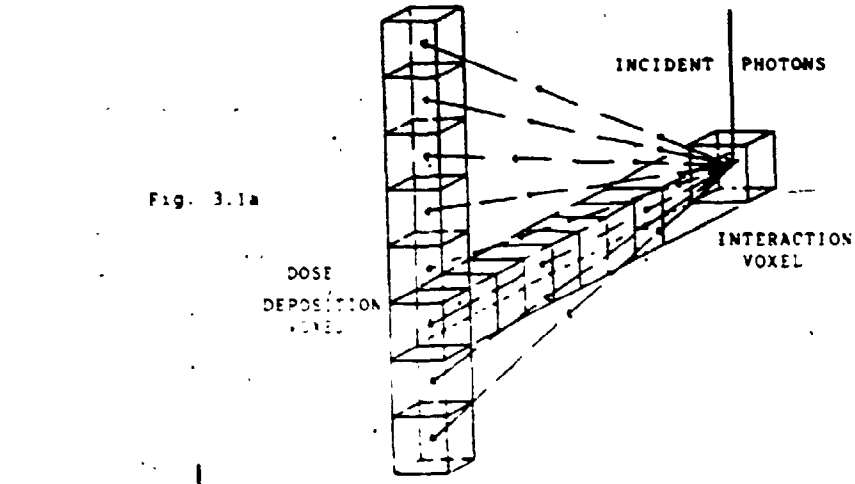

Fig. 3.1a

THE INTERACTION POINT OF VIEW

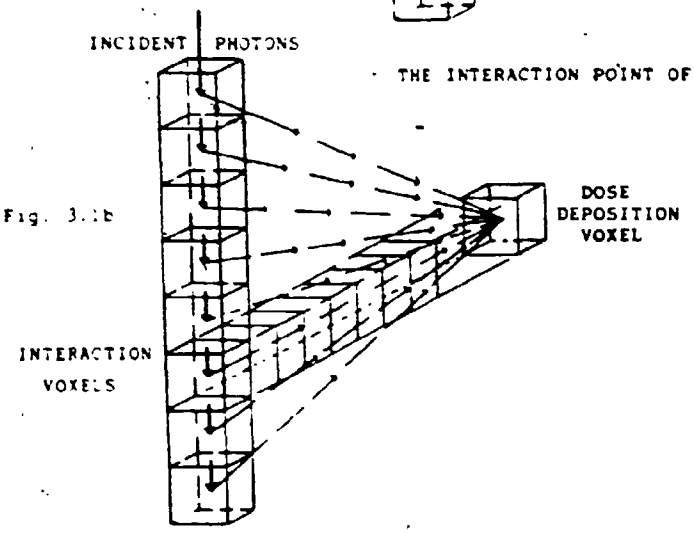

Fig. 3.1b

THE DOSE DEPOSITION POINT OF VIEW

Figure 3.1

(a) The Interaction Point of View. (b) The Dose Deposition Point of View.

In this project, the second method, the dose deposition point of view, was adopted to determine a one-dimensional dose spread function. This function is similar to the dose spread array of Mackie et al [73,74], however, in this thesis it is reduced to one-dimension. Although a more approximate kernel results, this approach avoids the time-consuming calculations of the Monte Carlo method.

3.4 Calculation of the Kernels

The irradiation geometry of the ionization chamber is illustrated in Figure 3.2. Although it is conventional to denote the axis of the beam as the z-axis, the irradiation geometry illustrated in Figure 3.2 was adopted for convenience. The cylindrical ionization chamber has an inside radius, r, and an outside radius, b, with a wall thickness, b-r, sufficient to meet the conditions for electronic equilibrium. The chamber is irradiated side on with its axis perpendicular to the direction of propagation of the photons and parallel to one principal plane. In this geometric configuration, the photon fluence is invariant along the axis of the ionization chamber. The ionization chamber can then be divided into a large number of equivalent discs of thickness dz.

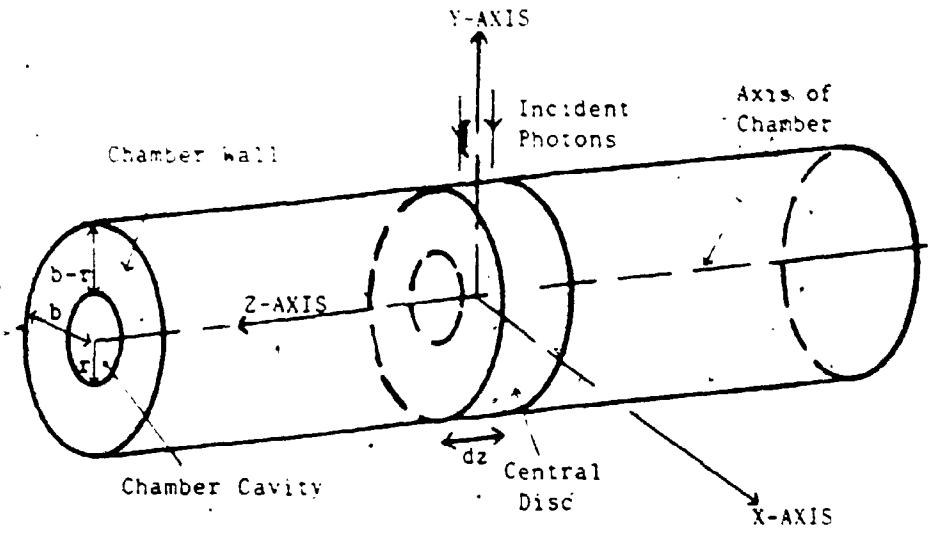

Figure 3.2: Irradiation Geometry of the Cylindrical Ionization Chamber

The kernel for the central disc, located at the origin, is calculated using the dose deposition point of view. The air cavity of the central disc is then the dose deposition voxel. The annulus of each disc (wall of the ionization chamber) is divided into a two-dimensional array of interaction voxels of dimensions dx.dy.dz. The increments of both the width, dx, and the height, dy, of the interaction voxel are equal to 0.1 mm. The thickness, dz, of the disc is related to the maximum lateral spread of the secondary electrons, L_{max}, according to the following relation:

$$dz = 2L_{max}/11 \qquad (3.5)$$

Each disc is divided into a two-dimensional array of interaction voxels. The dose deposited in the air cavity of the central disc, due to photon interactions in an interaction voxel, is calculated in turn for each interaction voxel and associated with the location of the interaction voxel. This results in a two-dimensional array of dose contributions associated with each disc. The assumption has been made that the photon-fluence is invariant along the axis of the ionization chamber. There are eleven identical discs. Therefore, the two-dimensional arrays of dose contributions associated with each of the eleven discs are coalesced into a single two-dimensional array of dose contributions by adding the dose

contributions from all interaction voxels of constant x- and y-indices. This two-dimensional array of dose contributions is further reduced to one-dimension, and after each element is normalized to the total dose deposited in the air cavity of the central disc, is termed the dose spread function or kernel. By definition, this kernel is associated with the central disc.

Only secondary electrons from eleven discs of thickness dz can contribute to the response of the central disc. The relative dose deposited in this air cavity, due to equal numbers of photon interactions in each interaction voxel, is calculated for each of the eleven discs in turn. The response associated with each secondary electron is determined by its pathlength through the air cavity of the central disc.

A Fortran program was developed locally to calculate the kernel associated with a cylindrical ionization chamber of any inside radius r, and electron density, ρ_e. The important steps in the calculation of the kernel associated with lucite-walled cylindrical ionization chamber of inside diameter, 2r, irradiated by Co-60 beam (hv=1.25 MeV) are described below to illustrate the general approach.

3.4.1: Kernel Calculation for Co-60.

The calculation of the kernel for Co-60 is carried out by first determining the energy and angular distribution of secondary electrons resulting from photon interactions in the wall material. At the mean photon energy of 1.25 MeV, only Compton interactions need be considered for Co-60. The energy distribution of the Compton electrons scattered at mean angle θ, $E(\theta)$, is calculated using the equation below:

$$E(\theta) = h\nu_o \frac{2\alpha \cos^2\theta}{(1+\alpha) - \alpha^2 \cos^2\theta} \qquad (3.6)$$

where $h\nu_o$ is the energy of the incident photon and $\alpha = h\nu_o / 0.511$, is the photon energy expressed in electron mass units. [37,38,62] Since the Compton electrons are scattered only in the forward direction, the energy, E_θ, is calculated at one degree intervals for the Compton electrons scattered between 0 and 90 degrees and stored in a lookup table.

The mean range, R_θ, of the Compton electrons scattered at angle θ in lucite is determined by dividing the electron energy, E_θ, by the average electron stopping power, $\bar{S}(E, \rho_e)$, for lucite [58,62]. That is:

$$\bar{R}_\theta = E_\theta / \bar{S}(E, \rho_e) \qquad (3.7)$$

The assumption is made that the Compton electrons maintain their initial directions of travel in the medium. The lateral spread of these electrons, L_θ, is then related to the mean range, $\bar{R}_\theta$, as $L_\theta = \bar{R}_\theta \sin\theta$. Again, since the Compton electrons are scattered only in the forward direction, the mean range, $\bar{R}_\theta$, and the lateral spread, L_θ, are calculated at one degree intervals for the Compton electrons scattered between 0 and 90 degrees. The maximum lateral spread of the electrons determined from these calculations, L_{max}, establishes the thickness of the disc along the chamber axis, $dz = 2L_{max}$ [11].

The Klein-Nishina differential collision cross section, $d_e\sigma/d\Omega$, is used to generated a lookup table of the scattering probability per unit solid angle, of Comptons electrons scattered at mean angle, θ, to the direction of the incident photon, at one degree intervals, using the equation below:

$$\frac{d(_e\sigma)}{d\Omega} = \left\{\frac{r_o^2}{(1+\alpha)}\right\}(1+\cos w)\left\{\frac{1}{1+\alpha(1-\cos w)}\right\}^2\left\{\frac{1+\cos^2 w}{2}\right\} \cdots$$

$$\times\left\{1 + \frac{\alpha^2(1-\cos w)^2}{(1+\cos^2 w)\{1+\alpha(1-\cos w)\}}\right\}\left\{\frac{\sin w}{\sin^3\theta}\right\} \qquad (3.8)$$

where $\alpha = h\nu_o/0.511$, is the photon energy expressed in electron mass units, $r_o = e^2/m_o c^2$ is the classical radius of the electron and w is the photon scattering angle [37,38]. The lookup-table approach for the angular distribution of

the Compton electrons is adopted to save computation time.

The kernel associated with the central disc is calculated in two stages. The first stage involves the calculation of the relative dose contributions (per incident photon fluence) from each interaction voxel of the central disc to the air cavity of the central disc. The second stage involves the calculation of the relative dose contributions from each interaction voxel in each out-of-plane discs to the air cavity of the central disc.

The first of these calculations, namely, the relative dose contribution from an interaction voxel of the central disc to the air cavity of the central disc employs the following approach. The angle β ($=\theta_l - \theta_s$) subtended at the interaction voxel by the air cavity of the central disc (indicated in Figure 3.3a) is divided into 15 equal angles, $\Delta\theta$ as illustrated in Figure 3.3b. The energy, E_θ, is obtained from the lookup table and the range, R_θ, of the Compton electron scattered into each of the angles $\Delta\theta$ (with θ varying from θ_s to θ_l in 15 increments) are calculated as the first step in determining if the electron can reach the edge of the air cavity.

Then, the pathlength of the secondary electron from the interaction voxel $A(x_i, y_i, z_i)$ to the edge of the air cavity, S, is calculated. From Figure 3.3c, m can be

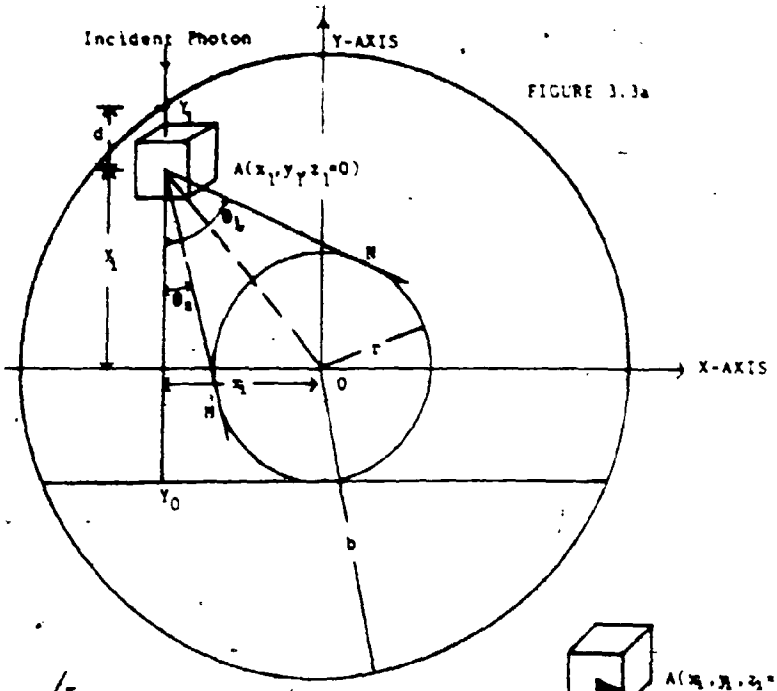

FIGURE 3.3a

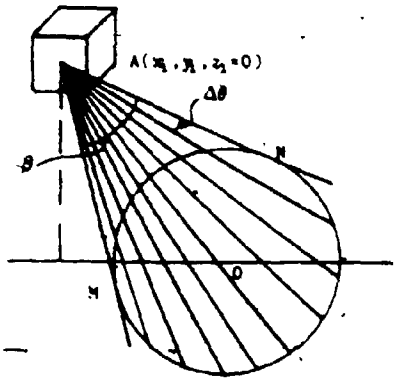

FIGURE 3.3b

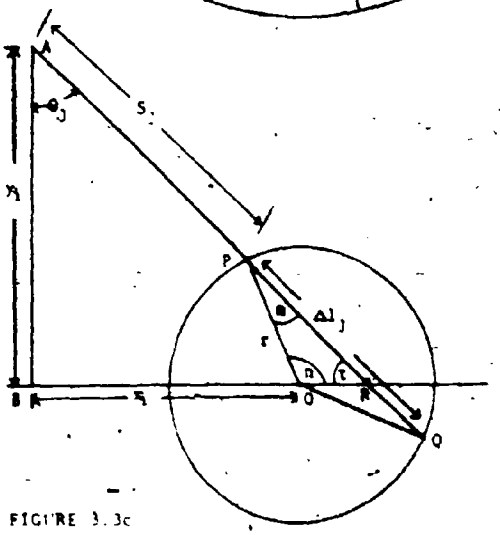

FIGURE 3.3c

FIGURE 3.3 KERNEL CALCULATION GEOMETRY FOR THE CENTRAL DISC.

obtained using the sine law, and hence n (=180-m-t) can be determined. The pathlength of the secondary electron from the interaction voxel to the edge of the air cavity, S is then given by:

$$S = AP = AR - PR$$

which, using the cosine law, is given by:

$$S = y_i \sec\theta - (OR^2 + PO^2 - 2.OR.PO.\cos n)^{\frac{1}{2}} \qquad (3.9)$$

In the event that the electron range, R_θ, is greater than the pathlength to the edge of the cavity, its pathlength through the air cavity of the central disc, Δl, which, from Figure 3.3c, is equal to 2rcosm, is determined. The response of the air cavity associated with this electron is obtained by multiplying Δl by the appropriate $d\sigma/d\Omega'$. The relative number of ionizations produced in the air cavity of the central disc (per incident photon fluence) due to electrons originating from the interaction voxel located at $A(x_i, y_i, z_i)$ ΔN_i is then obtained by summation over the angle β using the following equation:

$$dN_i = \sum_{j=1}^{j=15} \frac{d\sigma(\theta_j, h\nu)}{d\Omega'} \cdot \Delta l_j \cdot \Delta\Omega_j \qquad (3.10)$$

where Δl_j is the pathlength through the air cavity of the central disc, and $\Delta\Omega_j$ is the element of solid angle subtended at the interaction voxel.

The relative dose contributions from the interaction

voxels along each strip of constant x-index in the central disc, to the air cavity of the central disc, are calculated in turn by increasing the y index in steps of 0.1 mm from the lower edge of the cavity, Y_0, to the top surface of the strip, Y_1, as indicated earlier. The calculation is extended only to the lower edge of the cavity because the Compton electrons are scattered only in the forward direction.

It can be assumed that the photons are incident parallel to the strip of interaction voxels (the y-axis). This assumption is valid on the basis that the chamber outer diameter is much smaller than the photon-source to chamber distance (80, 100 and 110 cm for Co-60, 6- and 31-MV x-ray units respectively). Therefore, the relative number of photons reaching each voxel of the strip (at depth d from the top surface of the strip) is proportional to $\exp[-\mu.d]$, where $\mu(h\nu, P_a)$ is the linear attenuation coefficient for the medium. The relative dose contribution from each interaction voxel is multiplied by the appropriate attenuation factor, $[-\mu.d]$, to account for photon attenuation.

The relative dose contributions (per photon fluence) from the interaction voxels along other strips of the central disc are calculated by increasing the x index in steps of 0.1 mm to the maximum lateral spread of the

electrons. As a result of the cylindrical angular dependence of the Compton electrons, calculations are implemented for only one half of the disc. The relative dose contributions from interaction voxels in the two halves of the disc are the mirror images of each other.

The second stage in the calculation of the kernel associated with the central disc involves the calculation of the relative dose contributions from interaction voxels in the offset discs to the air cavity of the central disc. The dimensions of the interaction voxel are the same and the calculations are implemented for each offset disc in turn. Since the interaction voxels of an offset disc are out of the plane of the dose deposition voxel (the air cavity of the central disc), the calculations require some modification.

In order to calculate the ionization produced in the air cavity of the central disc due to electrons originating from the interaction voxel $A(x_i, y_i, z_i)$, we need to calculate the pathlength of an electron from the point of origin to the edge of the air cavity, S, and its pathlength in the air cavity of the central disc, Δl. These calculations can be illustrated by considering orthogonal projections of the cylindrical ionization chamber in the x-y and y-z planes. In Figures 3.4 a and b, an interaction voxel of an offset disc is illustrated, and electrons

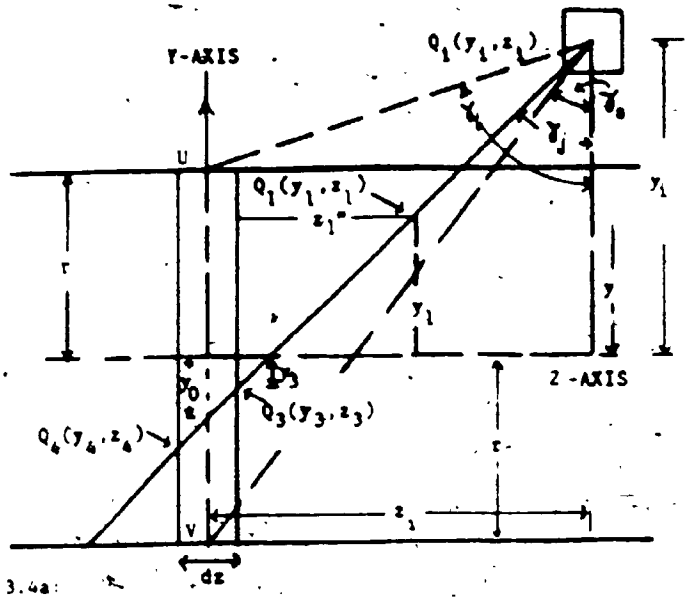

FIGURE 3.4a:
THE Y-Z PROJECTION.

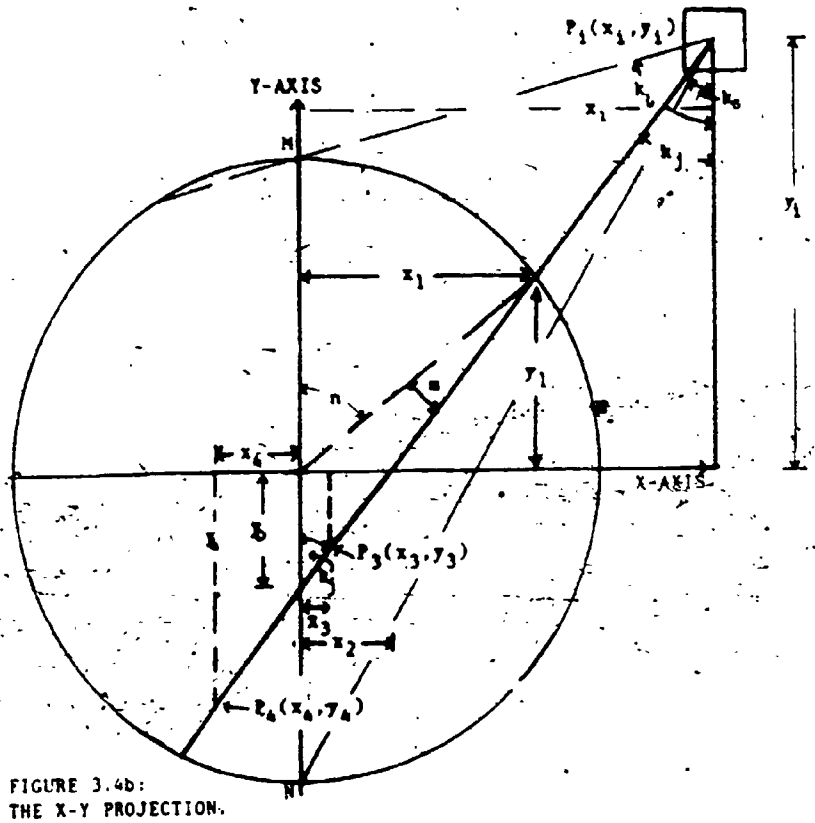

FIGURE 3.4b:
THE X-Y PROJECTION.

FIGURE 3.4: ORTHOGONAL PROJECTIONS OF THE CYLINDRICAL IONIZATION CHAMBER.

originating from this interaction voxel, traveling between the ray lines QU and QV (in Fig. 3.4a) and PM and PN (in Fig. 3.4b) can reach the air cavity of the central disc located at the origin O, if they have sufficient energy to reach the wall of the air cavity. These orthogonal projections can be used to determine both S and Δl. The details of these calculations are described in Appendix 3A and summarized below:

In order to calculate S and Δl, we need to calculate the following:

(i) the point of entry of the electron to the air cavity, $Q_1(x_1,y_1,z_1)$;

(ii) the point of entry of the electron into the air cavity of the central disc, $Q_3(x_3,y_3,z_3)$; and

(iii) the point of exit of the electron from the air cavity of the central disc, $Q_4(x_4,y_4,z_4)$.

These points are illustrated in Figures 3.4a and 3.4b, the orthogonal projections in the y-z and x-y planes respectively.

After the determination of the coordinates (x_1,y_1,z_1), (x_3,y_3,z_3), and (x_4,y_4,z_4), as described in Appendix 3A, the pathlength from the interaction voxel, $A(x_1,y_1,z_1)$, to the edge of the air cavity, S_j, is calculated using the

following equation

$$S_j^2 = (x_1 - x_1)^2 + (y_1 - y_1)^2 + (z_1 - z_1)^2 \qquad (3.11)$$

The pathlength of the electron through the air cavity of the central disc, Δl_j, is given by:

$$\Delta l_j^2 = (x_3 - x_4)^2 + (y_3 - y_4)^2 + (z_3 - z_4)^2 \qquad (3.12)$$

The relative number of ionizations produced in the air cavity of the central disc due to electrons originating from the interaction voxel $A(x_1, y_1, z_1)$ and scattered between the angles θ_j and $\theta_j + d\theta$ (to the direction of the incident photon) into the solid angle $\Delta\Omega_j$, $\Delta N_{1,j}$, is given by:

$$\Delta N_{1,j} = \frac{d\sigma(\theta_j, h\nu)}{d\Omega} \cdot \Delta l_j \cdot \Delta\Omega_j \qquad (3.13)$$

And the relative number of ionizations produced in the air cavity of the central disc due to electrons originating from the interaction voxel $A(x_1, y_1, z_1)$, is given by:

$$\Delta N_1 = \sum_{j=1}^{j=15} \frac{d\sigma(\theta_j, h\nu)}{d\Omega} \cdot \Delta l_j \cdot \Delta\Omega_j \qquad (3.14)$$

(The calculation of $\Delta\Omega_j$ is described in Appendix 3A.)

Again, the calculations summarized above, and described in detail in Appendix 3A, are repeated for each interaction voxel of the offset disc. Calculations for offset disc on

only one side of the central disc are required as a result of the cylindrical angular dependence of the Compton electrons.

The above two-stage calculations determine the response of the air cavity of the central disc due to interactions in both the central disc and the surrounding discs. It has been indicated earlier, however, that this response is equivalent to the response of the entire cavity of the ionization chamber due to the photon interactions in the central disc only. This response is the kernel associated with the central disc. The relative dose contributions (per incident photon fluence) from interaction voxels of constant x- and y- indices, of the eleven discs (a central disc and ten out-of-plane discs) are added. This yields a two-dimensional array of relative dose contributions, $K(x_1,y_1)$. This two-dimensional array of relative dose contributions is the dose spread function or kernel associated with the central disc of the ionization chamber. Since all the discs are identical, $K(x_1,y_1)$ is the kernel associated with each disc of the ionization chamber if end effects are ignored.

It can be recalled that in the calculation of the relative dose contributions from interaction voxels along each strip, photon attenuation along the strip was taken into account. With this correction, the kernel elements

along each strip (constant x-index) can be added to obtain a one-dimensional kernel, $K(x_i)$. That is,

$$K(x_i) = \sum_{y_i=Y_0}^{y_i=Y_1} K(x_i, y_i) \qquad (3.15)$$

This one-dimensional kernel, $K(x_i)$, calculated using the method described above, is applicable only to cylindrical ionization chambers. The reduction of the kernel to one-dimension was adopted to simplify both the calculation of the convolution product and the presentation of the results.

3.4.2: Kernel Calculation for 6- and 31-MV X Rays

The method employed in the calculation of the kernels for Co-60 units can be extended to calculate the kernels for linear accelerators. Since the photon energy spectra of the accelerators are not known, effective energies of 50% of the maximum photon energies were chosen for both the 6- and 31-MV x-ray beams. Again, only Compton interactions were considered for the 6- and 31-MV x rays to simplify the kernel calculation.

Since the lateral spread of the secondary electrons is greater for the two accelerators than for Co-60, the thickness of the disc, dz, increases with the photon energy

and correspondingly the size of the interaction voxel. The width, dx, and the height, dy, of the interaction voxel were maintained at 0.1 mm. The increase in the equilibrium thickness with the photon energy, (1.5 and 5.0 gm/cm^2 for 6- and 31-MV x rays respectively), results in an increase in the number of interaction voxels in each disc.

3.4.3: Kernel Calculation for Different Electron Densities

The kernel calculations in the preceeding sections for Co-60, 6- and 31-MV x rays respectively, were described for lucite-walled cylindrical ionization chambers of varying inside diameter. The same approach was employed in the calculation of the kernels associated with cedar-, balsa-, and copper-walled cylindrical ionization chambers of varying inside diameter. Again, only Compton interactions were considered for all photon energies and chamber wall electron densities.

The calculated one-dimensional kernel or dose spread function, expresses the photon interactions in the chamber wall, the transport of the electrons in the chamber wall and their energy deposition in the chamber cavity. This kernel, $K(x_i, hv, \rho_e, i.d.)$, is a function of the lateral position with respect to the chamber axis, x_i, the photon energy, hv, the electron density of the chamber, ρ_e, and

the inside diameter of the ionization chamber, i.d.

3.5 Dose Calculation by Convolution Method

In this project, the photon-fluence distribution in the penumbral region has been determined for the first time. The convolution method can then be extended to the calculation of dose distributions in these regions. The relationship between the primary photon-fluence distribution and the primary dose distribution is of particular interest because it allows the study of secondary electron effects directly without the complication associated with scattered photons. In this project, therefore, only primary photon-fluence distributions and the associated kernels were considered.

In general, the dose distribution in an entire phantom is desired and this entails the use of a three-dimensional kernel and a three-dimensional convolution calculation. In this project, however, one-dimensional photon-fluence distributions were determined (using ionometric techniques) along a principal plane of the photon beam, through the isocentre of the machine, and in a direction perpendicular to the axis of the beam. Since it was also possible to calculate a one-dimensional kernel, the required convolution calculation is one-dimensional.

If the photon-fluence distribution is stored in a linear array of n elements as Fluence(n) with elements Fluence(1), Fluence(2), .., Fluence(n), corresponding to the photon fluence at positions X(1), X(2), ..., X(n), in increments of 0.1 mm, the convolution equation for the calculation of the dose, D(X), at the centre of the ionization chamber when located at position X becomes:

$$\text{Dose}(X) = \sum_{j=-M}^{j=M} \text{Fluence}(i-j).K(j) \qquad (3.16)$$

where K(-M), K(-M+1), ..., K(M-1), K(M) are the 2M+1 elements of the convolution kernel. [21]

The photon-fluence distributions used in the convolution calculations were obtained experimentally. For convenience, the calculated penumbral distributions were normalized to 50% at 50 mm from the isocentre. The results of these calculations are described in Chapter V.

CHAPTER IV

EXPERIMENTAL RESULTS

4.1 Ionometric Measurements for High-Energy X-ray Beams

This project has adopted a penumbral model which indicates that two distributions exist in the penumbral region of high-energy radiation beams, namely, the photon-fluence distribution and the dose distribution. The photon-fluence distribution is associated with the x-ray unit (the radiotherapy machine) while the dose distribution is associated with the energy deposition of the secondary electrons set in motion by photon interactions. The difference between the two penumbral distributions is associated with the lateral spread of the secondary electrons.

There are two components to the distributions in the penumbral region of high-energy x-ray beams, namely, the primary and secondary radiation components. Since the secondary component tends to mask the physical processes that result in the different distributions in the penumbral region, the penumbral model is best checked by considering the primary component only. Experimental techniques are introduced to determine both the primary penumbral photon-fluence distribution and the primary penumbral dose distribution of high-energy radiotherapy photon beams.

The work of Greene [47] and Harper [49] has indicated some dependence of the dose distribution measured in the penumbral region of high-energy x-ray beams on the type and configuration of the radiation detector. Cylindrical lucite-walled ionization chambers of varying inside diameter were used for measurement of the primary penumbral dose distributions.

The increase in the lateral spread of the secondary electrons with increasing photon beam energy has been established in a number of recent publications [67,73,74,75]. The effect has been studied by using three beam energies available in the London Regional Cancer Centre namely, Co-60, 6- and 31-MV x rays.

Recent publications by Kornelsen and Young [67], Young and Kornelsen [116] and Mackie et al [73,74,75] have indicated that the lateral spread of the secondary electrons increases in media of decreased electron density. Ionization chambers with walls of cedar and balsa were used to study the increasing lateral electron spread with decreasing electron density.

With increasing electron density, the lateral spread of the secondary electrons is reduced and the penumbral dose distributions become narrower. In the limit, when the electron density approaches infinity, the lateral spread of the secondary electrons is zero and the penumbral dose

distribution is equivalent to the penumbral photon-fluence distribution. Ionization chambers with walls of copper were used to investigate the effect of the reduced lateral spread of the secondary electrons on the penumbral distribution of high-energy photon beams.

All measurements were made in air at the depth of electronic equilibrium, namely 0.5, 1.5 and 5.0 g/cm^2 for Co-60, 6- and 31-MV x rays respectively. For each beam energy, square fields of 10-cm side length were employed. All measurements were made through the isocentres located 80, 100 and 110 cm for the Co-60 unit, 6- and 31-MV x-ray units respectively. Trimmer bars were installed at 53 cm from the source for the Co-60 measurements.

4.2 Co-60 Penumbral Dose Distributions in Lucite

4.2.1 Effect of Chamber Inside Diameter

The effect of the configuration of the radiation detector on the penumbral distribution for Co-60 was studied using lucite-walled ionization chambers of varying inside diameter. A number of the measured penumbral distributions are indicated in Figure 4.1 along with the distribution extrapolated to zero inside diameter.

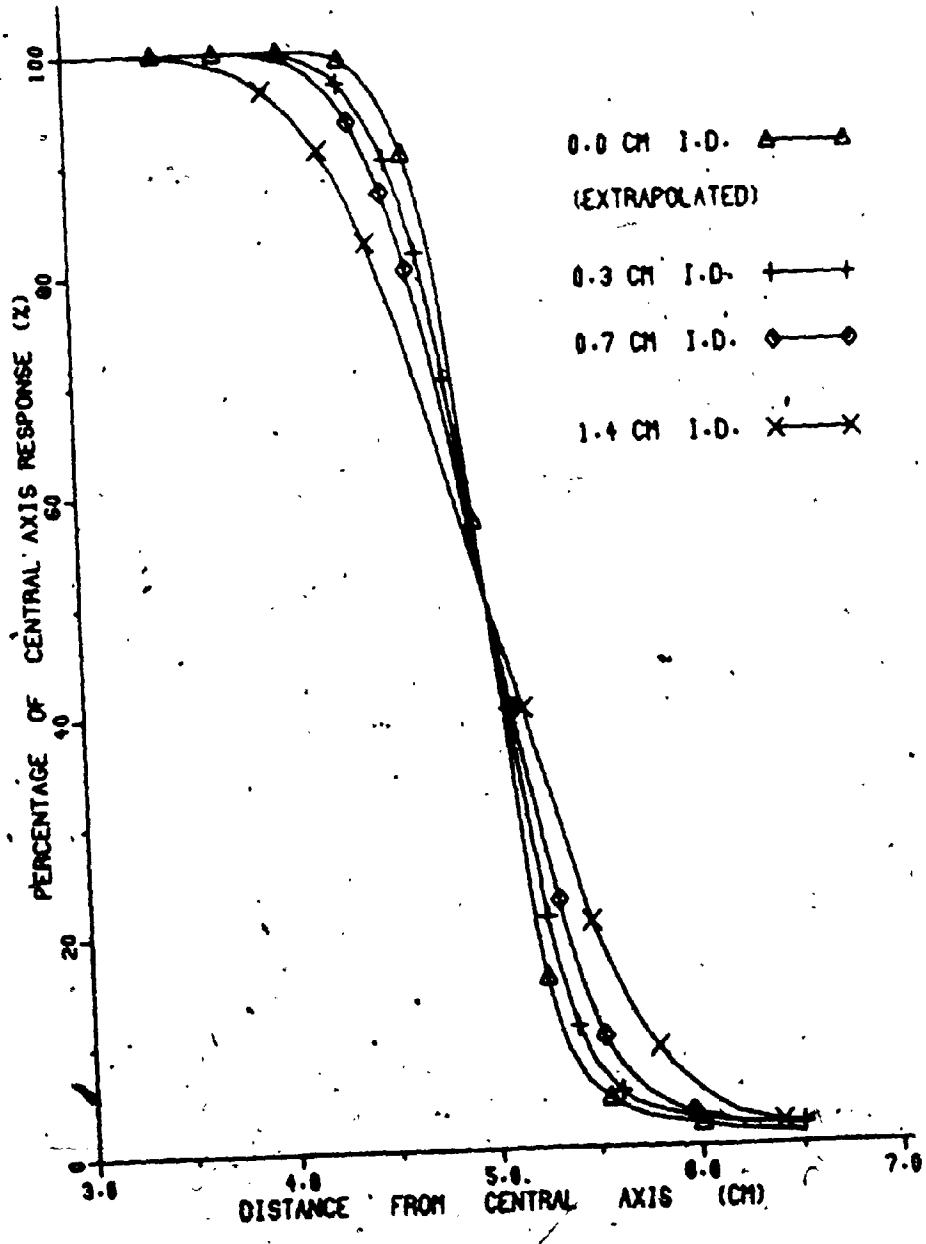

FIGURE 4.1

THE VARIATION OF THE PENUMBRAL DOSE DISTRIBUTION (IN LUCITE) WITH CHAMBER INSIDE DIAMETER FOR CO-60 BEAM

The penumbral widths, determined from these and other measured distributions, are listed as a function of chamber inside diameter in Table 4.1. The P20-80 and P10-90 penumbral widths are shown as a function of inside diameter in Figure 4.2. The linear least squares fits with correlation coefficients greater than 0.99 are represented by the solid lines while the linear extrapolations to zero inside diameter are indicated by the broken lines. The error bars indicate one standard deviation. The P20-80 and P10-90 penumbral widths, measured with the PTW and Farmer ionization chambers, are also indicated in Figure 4.2. The standard deviations are +/-0.03 and +/-0.07 cm for the P20-80 and P10-90 penumbral widths respectively.

The symmetry of the penumbral dose distributions about the 50% dose level is indicated in Table 4.1. Asymmetry in the widths is evident only beyond the 90-10% dose region with the lower dose levels showing the greater width.

4.2.2 Co-60 Primary Penumbral Dose Distribution

Figure 4.2 and Table 4.1 indicate clearly the linear dependence of the measured penumbral widths on the inside diameter of the ionization chamber. A first approximation to the correct penumbral dose distribution in tissue-equivalent media can be made by extrapolating these penumbral widths to zero inside diameter and plotting the

Table 4.1

Penumbral Difference	Inside Ionization Chamber Diameter (cm)						Least Squares Fit	
	0.3	0.5	0.7	1.0	1.2	1.4	Slope	Intercept
%	Penumbral Width (cm)						cm/ cm i.d.	(cm)
P50-98	0.71	0.73	0.80	0.93	1.02	1.14	0.40	0.55
P50-95	0.58	0.60	0.65	0.77	0.83	0.93	0.33	0.45
P50-93	0.51	0.55	0.58	0.69	0.75	0.85	0.31	0.40
P50-90	0.44	0.47	0.52	0.61	0.66	0.74	0.27	0.34
P50-85	0.35	0.38	0.42	0.50	0.54	0.61	0.24	0.27
P50-80	0.28	0.30	0.35	0.41	0.45	0.50	0.20	0.21
P50-70	0.18	0.20	0.22	0.26	0.29	0.32	0.13	0.14
P50-60	0.09	0.10	0.11	0.13	0.15	0.16	0.07	0.07
P50-40	0.09	0.10	0.11	0.13	0.15	0.16	0.07	0.07
P50-30	0.18	0.20	0.23	0.26	0.30	0.33	0.14	0.13
P50-20	0.27	0.31	0.35	0.41	0.45	0.50	0.21	0.21
P50-15	0.34	0.38	0.43	0.50	0.56	0.61	0.25	0.26
P50-10	0.43	0.48	0.53	0.62	0.70	0.76	0.30	0.33
P50-05	0.61	0.69	0.74	0.85	0.90	1.01	0.35	0.51
P20-80	0.55	0.61	0.70	0.82	0.90	1.00	0.41	0.42
P10-90	0.87	0.95	1.05	1.23	1.36	1.50	0.58	0.67

Table 4.1: Penumbral Width versus Chamber Inside Diameter for Co-60.

Medium: Lucite.

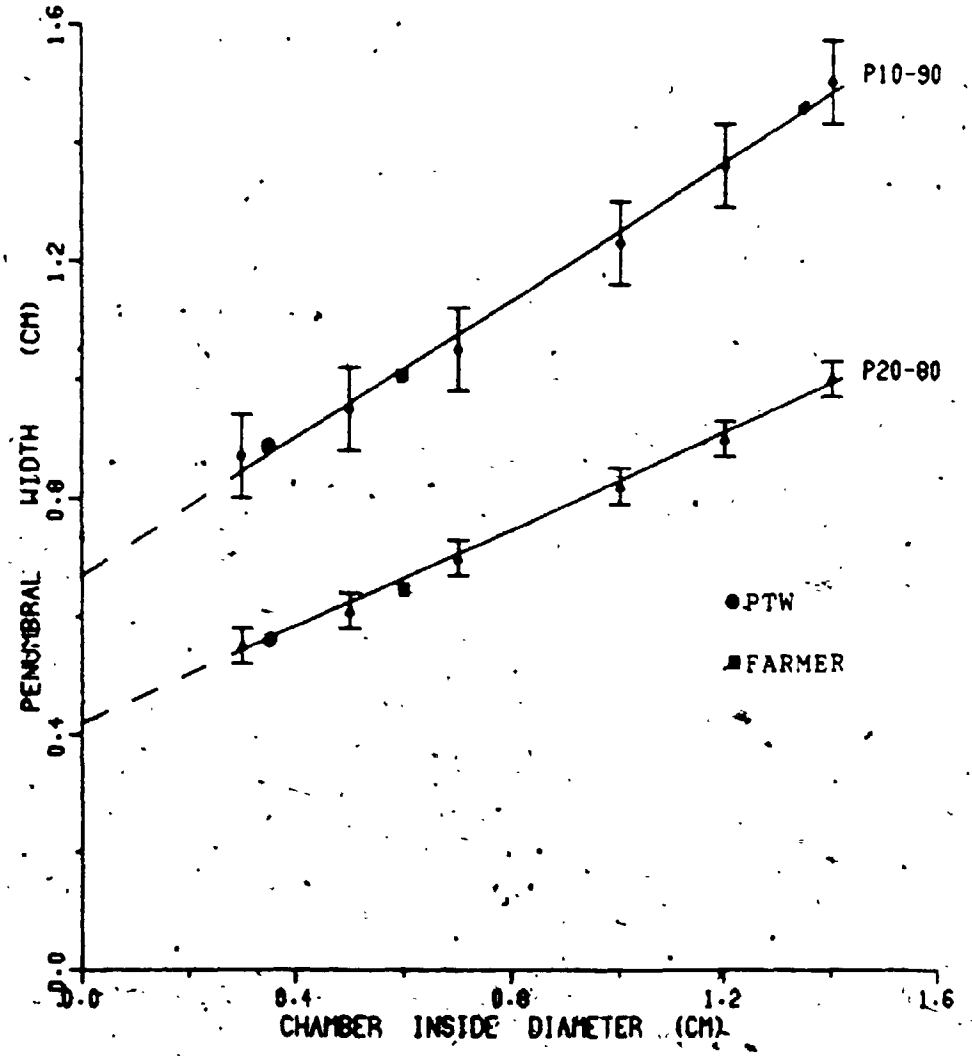

FIGURE 4.2

THE P20-80 AND P10-90 PENUMBRAL WIDTH VERSUS CHAMBER INSIDE DIAMETER FOR CO-60 BEAM. MEDIUM: LUCITE.

results relative to the position of the 50% dose level. This distribution is indicated as the extrapolated distribution in Figure 4.1. This figure indicates significant degradation of the penumbral distributions measured for ionization chambers with inside diameters corresponding to commercially-available detectors.

4.3 6- and 31-MV X-ray Distributions in Lucite

4.3.1 Effect of Chamber Inside Diameter

The dependence of the 6- and 31-MV x-ray penumbral dose distributions on the inside diameter of the ionization chamber was also investigated. The same set of chambers were used for the Co-60, 6- and 31-MV x-ray beams. Appropriate buildup sleeves of 1.0 g/cm^2 and 4.5 g/cm^2 for 6- and 31-MV x rays respectively were added to the chambers to achieve the depth required for electronic equilibrium.

The measured penumbral dose distributions for 6- and 31-MV x rays are similar to those illustrated in Figure 4.1. Penumbral widths were similarly determined as a function of chamber inside diameter and are listed in Tables 4.2 and 4.3 for the 6- and 31-MV x rays respectively, along with the parameters of the linear least squares fits. The P20-80 and P10-90 penumbral widths for the specially designed ionization chambers, the PTW and the

Table 4.2

Penumbral Difference (%)	Inside Diameter (i.d.) of Ionization Chamber (cm)						Least Squares Fit	
	0.3	0.5	0.7	1.0	1.2	1.4	Slope	Intercept
	Penumbral Width (cm)						cm/cm i.d.	(cm)
P50-98	0.68	0.74	0.85	0.97	1.07	1.12	0.42	0.55
P50-95	0.50	0.55	0.63	0.76	0.86	0.93	0.41	0.36
P50-93	0.43	0.50	0.58	0.69	0.77	0.86	0.39	0.31
P50-90	0.36	0.42	0.49	0.60	0.69	0.77	0.38	0.24
P50-85	0.28	0.33	0.40	0.51	0.57	0.65	0.34	0.17
P50-80	0.22	0.27	0.34	0.43	0.47	0.54	0.29	0.13
P50-70	0.14	0.18	0.22	0.28	0.32	0.36	0.20	0.08
P50-60	0.07	0.09	0.11	0.14	0.16	0.18	0.10	0.04
P50-40	0.07	0.09	0.10	0.14	0.16	0.18	0.10	0.04
P50-30	0.14	0.18	0.22	0.29	0.32	0.36	0.20	0.08
P50-20	0.26	0.31	0.36	0.43	0.48	0.54	0.25	0.18
P50-15	0.35	0.41	0.45	0.52	0.58	0.65	0.26	0.27
P50-10	0.49	0.54	0.58	0.65	0.71	0.80	0.27	0.41
P50-05	0.88	0.92	1.05	1.18	1.22	1.25	0.37	0.77
P20-80	0.48	0.58	0.70	0.86	0.95	1.08	0.54	0.32
P10-90	0.85	0.96	1.07	1.22	1.40	1.57	0.64	0.64

Table 4.2: Penumbral Width versus Chamber Inside Diameter for 6-MV X Rays.

Medium: Lucite.

Table 4.3

Penumbral Difference (%)	Inside Diameter (i.d.) of Ionization Chamber (cm)						Least Squares Fit	
	0.3	0.5	0.7	1.0	1.2	1.4	Slope	Intercept
	Penumbral Width (cm)							(cm)
P50-98	1.38	1.40	1.41	1.43	2.44	1.45	0.06	1.37
P50-95	0.85	0.90	0.94	1.01	1.05	1.08	0.21	0.79
P50-93	0.71	0.75	0.79	0.86	0.92	0.95	0.23	0.64
P50-90	0.56	0.60	0.64	0.71	0.78	0.84	0.25	0.47
P50-85	0.39	0.43	0.49	0.58	0.62	0.69	0.27	0.30
P50-80	0.29	0.33	0.39	0.48	0.51	0.58	0.26	0.21
P50-70	0.17	0.21	0.25	0.31	0.34	0.38	0.19	0.12
P50-60	0.08	0.10	0.13	0.16	0.17	0.19	0.10	0.05
P50-40	0.08	0.10	0.13	0.16	0.17	0.19	0.10	0.05
P50-30	0.17	0.21	0.26	0.32	0.34	0.39	0.20	0.12
P50-20	0.35	0.39	0.46	0.52	0.56	0.61	0.24	0.28
P50-15	0.52	0.56	0.62	0.68	0.73	0.78	0.24	0.45
P50-10	0.85	0.90	0.95	1.02	1.06	1.12	0.24	0.78
P50-07	1.40	1.40	1.45	1.54	1.58	1.62	0.22	1.31
P50-05	2.46	2.46	2.46	2.46	2.46	2.46	0.00	2.46
P20-80	0.64	.72	.85	1.00	1.07	1.19	0.50	0.49
P10-90	1.44	1.50	1.59	1.73	1.84	1.96	0.49	1.26

Table 4.3: Penumbral Width versus Chamber Inside Diameter for 31-MV X rays.

Medium: Lucite.

Farmer chambers are illustrated in Figures 4.3 and 4.4 for the 6- and 31-MV x rays respectively. The linear least squares fits are indicated by the solid lines. The error bars are one standard deviations each, and are +/-0.03 and +/-0.07 cm for the P20-80 and P10-90 penumbral widths respectively. The results in Figures 4.3 and 4.4 indicate significant degradation of the penumbral distributions for inside diameters corresponding to commercially-available models.

The measured penumbral dose distributions for 6- and 31-MV x rays are symmetric about the 50% dose level between the 20-80% dose levels, beyond which the penumbral widths diverge significantly. Again, the lower dose level regions show the greater widths.

4.3.2 Primary Penumbral Dose Distributions

The penumbral widths in Tables 4.2 and 4.3 were found to be linearly dependent on the inside diameter of the chamber with a correlation coefficient greater than 0.99. The extrapolation to zero inside diameter yields a first approximation to the penumbral widths of the primary penumbral dose distribution that can be measured in an equilibrium volume of lucite. The primary penumbral dose distributions, derived from these extrapolated penumbral widths, are illustrated for 6- and 31-MV x rays in

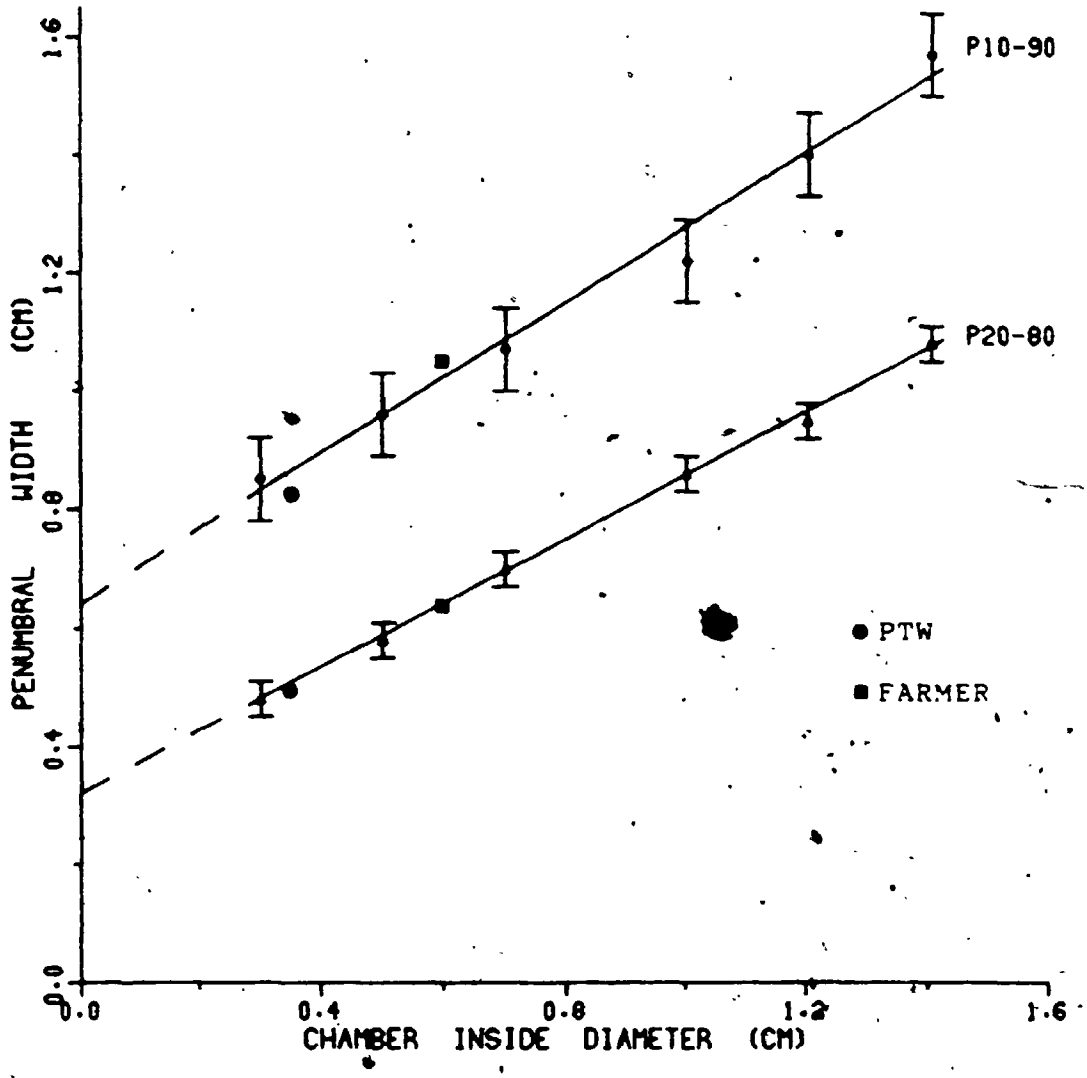

FIGURE 4.3

THE P20-80 AND P10-90 PENUMBRAL WIDTH VERSUS CHAMBER INSIDE DIAMETER FOR 6-MV X-RAY BEAM. MEDIUM: LUCITE

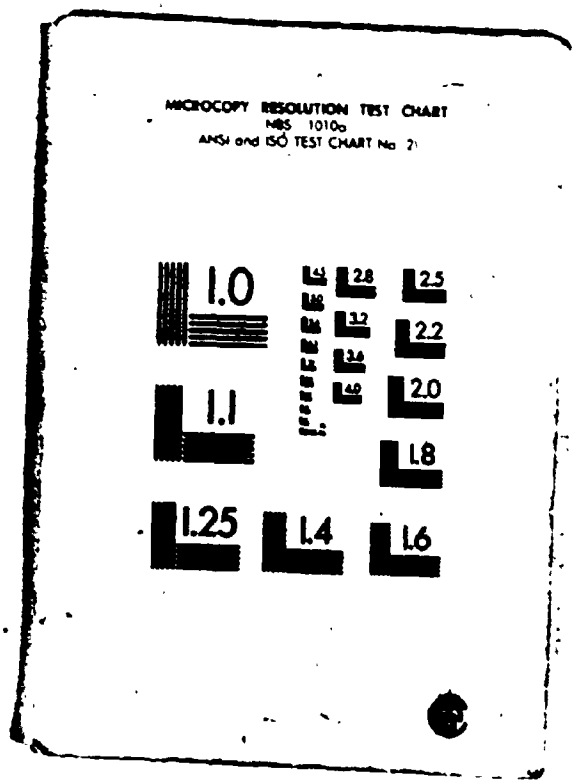
MICROCOPY RESOLUTION TEST CHART
NBS 1010a
ANSI and ISO TEST CHART No. 2
1.0
1.1
1.25
1.4
1.6
1.8
2.0
2.2
2.5
2.8
3.2
3.6
4.0

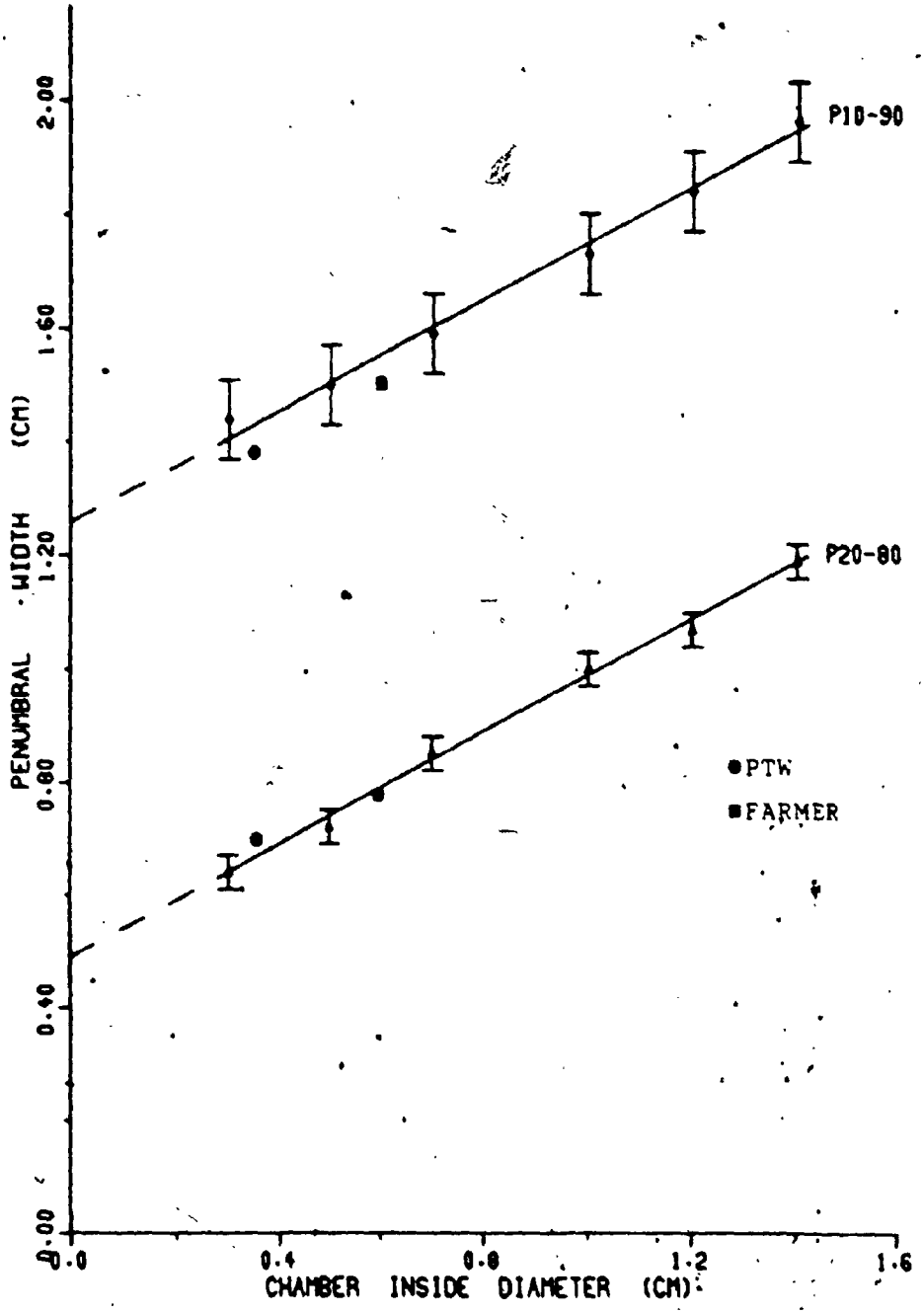

FIGURE 4.4

THE P20-80 AND P10-90 PENUMBRAL WIDTH VERSUS CHAMBER INSIDE DIAMETER FOR 31-MV X-RAY BEAM. MEDIUM: LUCITE

Figure 4.5 along with that for Co-60. This figure indicates that the primary penumbral dose distribution in lucite (or soft tissue) is clearly broader for 31-MV x rays than for either Co-60 or 6-MV x rays.

4.4 Energy Dependence of the Penumbral Distributions

Two parameters were introduced in the ionometric determination of the primary penumbral dose distributions of high-energy x-ray beams, namely, the slope and the intercept of the linear least squares fit associated with the dependence of the measured penumbral widths on the inside diameter of the ionization chamber. The parameters of the P20-80 and P10-90 penumbral widths are listed as a function of the beam energy in Table 4.4. Since the standard errors of the slopes are +/-0.05 and +/-0.13 cm/(cm inside diameter) for the P20-80 and P10-90 penumbral widths respectively, these slopes can be considered independent of the photon beam energy. These slopes are a measure of the degradation of the penumbral dose distributions associated with the chamber inside diameter.

The measured intercepts for the primary penumbral dose widths are also indicated in Table 4.4. The standard deviations of the P20-80 and P10-90 penumbral intercepts are +/-0.03 and +/-0.07 cm respectively. In Table 4.5,

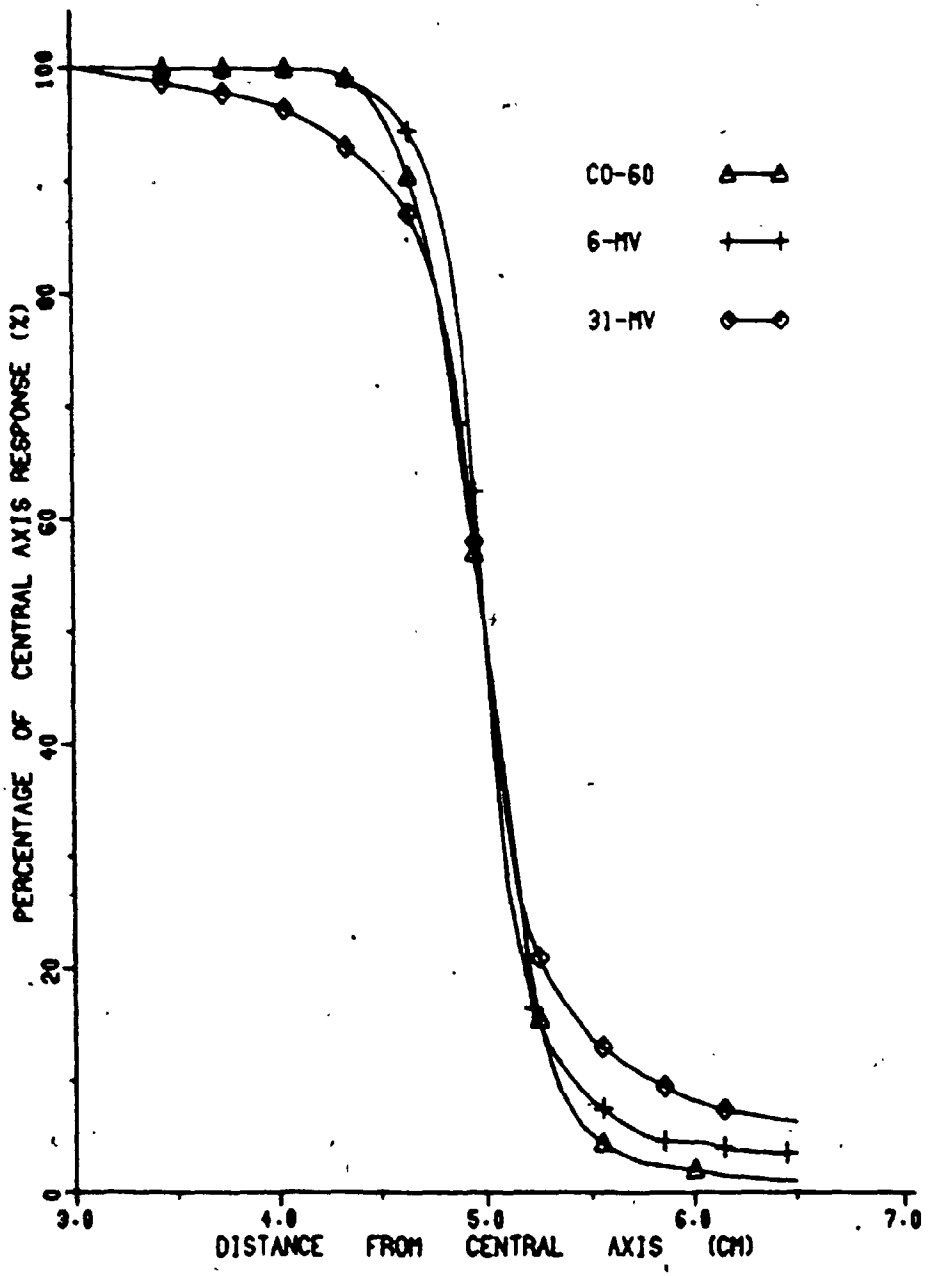

FIGURE 4.5

THE PRIMARY PENUMBRAL DOSE DISTRIBUTIONS IN SOFT TISSUE FOR CO-60, 6-MV AND 31-MV X-RAY BEAMS.

Table 4.4

Beam Energy	P20-80 Parameters		P10-90 Parameters	
	Intercept (cm)	Slope cm/cm i.d.	Intercept (cm)	Slope cm/cm i.d.
Co-60	0.42±.03	0.41±.05	0.67±.07	0.58±.13
6-MV X Rays	0.32±.03	0.54±.05	0.64±.07	0.64±.13
31-MV X Rays	0.49±.03	0.50±.05	1.26±.07	0.48±.13

Table 4.4: The P20-80 and P10-90 Parameters as a Function of Beam Energy for the Penumbral Dose Distributions in Lucite.

Table 4.5

Beam Quality	P20-80 +/-0.03 cm				P10-90 +/-0.07 cm			
	Inter-cept	Diode	PTW	Far-mer	Inter-cept	Diode	PTW	Far-mer
Co-60	0.42	0.46	0.56	0.65	0.67	0.74	0.89	1.01
6-MV X Rays	0.32	0.25	0.50	0.64	0.64	0.43	0.84	1.05
31-MV X Rays	0.49	0.28	0.69	0.78	1.26	0.66	1.42	1.54

Table 4.5: Extrapolated P20-80 and P10-90 Penumbral Dose Width and the P20-80 and P10-90 Penumbral Widths measured with the Diode, PTW and Farmer Ionization Chambers.

these intercepts are compared with the P20-80 and P10-90 penumbral widths measured with the diode, the PTW and the Farmer ionization chambers. The penumbral widths, measured with the diode, are significantly smaller than the intercepts for both accelerators. For Co-60, however, there is no significant difference. The penumbral widths for the two commercial ionization chambers are wider than the intercepts for all beam energies as indicated in Figures 4.2, 4.3 and 4.4 for Co-60, 6- and 31-MV x rays respectively.

4.5 Penumbral Distributions in Low-Density Media

A reduced electron density results in a broadening of the penumbral dose distribution [67]. This effect, which has been associated with the increased lateral spread of the secondary electrons, was investigated using cedar-walled and balsa-walled ionization chambers. The density of these media encompass the density of lung which has been shown to be dependent on the age of the patient [103]. The determination of the penumbral dose distribution in equilibrium volumes of cedar or balsa demonstrates the impact of lung on these distributions. Since equilibrium volumes for these low-density media result in extremely large ionization chambers, the effect of inhomogeneity of the walls of the ionization chambers is considered.

4.5.1 Effect of Inhomogeneity of the Chamber Wall

The equilibrium thicknesses in cedar and balsa are extremely large for both 6- and 31-MV x rays. For a square field of side length 10 cm, electronic equilibrium cannot be realized for these chambers. Ionization chambers with composite walls of cedar and lucite were, therefore, employed to determine the effect on the penumbral measurements of the inhomogeneity of the chamber wall.

The primary penumbral dose distribution for 6-MV x rays was measured using ionization chambers of 0.5 cm inside diameter. The walls were constructed in such a way that the inner annulus of cedar was varied from 0 to 100% of the total wall thickness. For all chambers but one, the total wall thickness corresponded to the equilibrium thickness for 6-MV x rays.

The P20-80 and P10-90 penumbral widths, determined from the measured distributions, are listed as a function of the percentage of cedar in the inner wall of the ionization chamber in Table 4.6. The results, plotted in Figure 4.6, indicate that the penumbral widths, measured with the composite chambers, are equivalent to those determined with a homogeneous cedar-walled chamber when the cedar constitutes more than 30% of the inner wall of the ionization chamber. The P20-80 and P10-90 penumbral widths, measured with a wall thickness of 80% of the

Table 4.6

Percentage of Cedar in Wall	Cedar Thickness in Chamber Wall	Lucite Thickness in Chamber Wall	Penumbral Widths	
			P20-80	P10-90
%	G/CM	G/CM	CM	CM
100.0	1.19*	0	0.94	1.72
77.1	1.19	0.35	0.92	1.78
55.9	0.84	0.66	0.89	1.74
32.0	0.50	0.85	0.93	1.71
16.0	0.23	1.18	0.79	1.41
0.0	0	1.77	0.57	0.93

Table 4.6: 6-MV X-ray P20-80 and P10-90 Penumbral Widths as a Function of Percentage of Cedar in Composite Cedar/Lucite-walled Ionization Chamber (I.D.=0.50 cm).

* This wall thickness is only 80% of the depth of electron equilibrium.

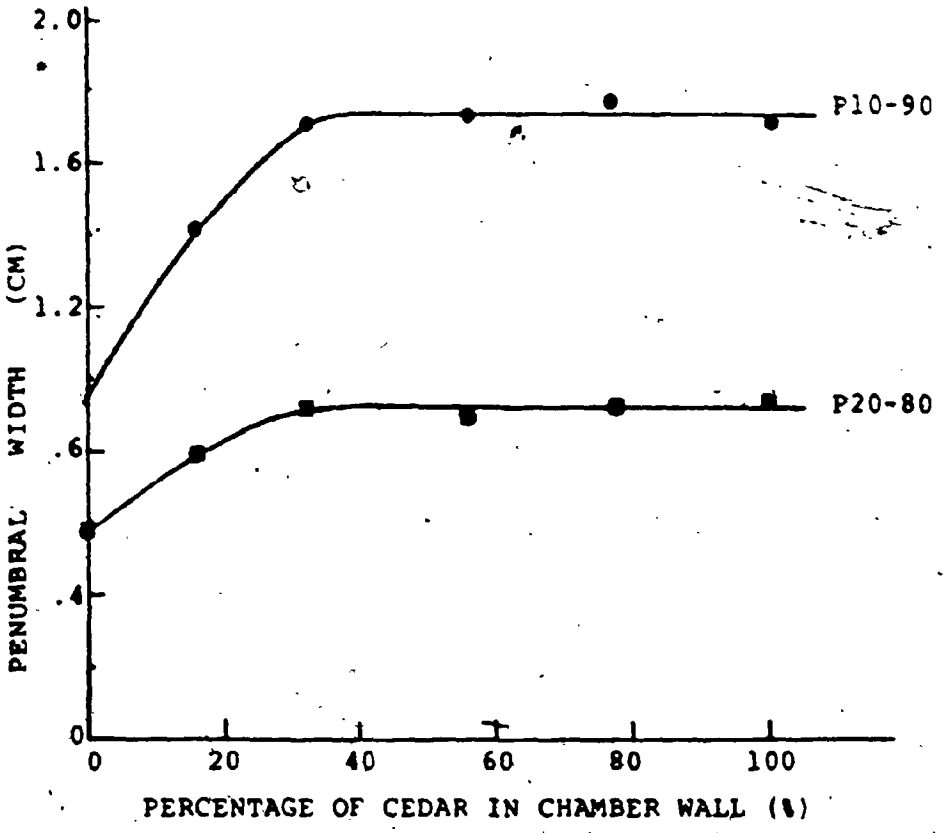

Figure 4.6: The P20-80 and P10-90 penumbral width versus percentage of cedar in composite cedar/lucite-walled ionization chamber for 6-MV x-ray beam.

equilibrium thickness, were also equivalent to those at the equilibrium depth.

The cedar-walled and balsa-walled chambers used for measurements on the 6-MV x-ray unit were composite chambers. Each chamber was surrounded with a lucite buildup cap to take the effective wall thickness to the electronic equilibrium depth.

The cedar-walled chamber used for the penumbral measurements for 31-MV x rays was a block of cedar of dimensions 30 X 30 X 20 cm (constructed from smaller blocks 2.5 X 2.5 X 20 cm) with a cedar-walled chamber of 0.5 cm inside diameter at the centre of the block.

4.5.2 Low-Density Effects for Co-60

The effect of the configuration of the radiation detector on the penumbral distribution for Co-60 was studied using cedar-walled and balsa-walled ionization chambers of varying inside diameter. The penumbral distributions, measured for a number of inside diameters, are illustrated in Figure 4.7 for the cedar-walled chambers. The degradation of the penumbral distributions increases with the chamber inside diameter.

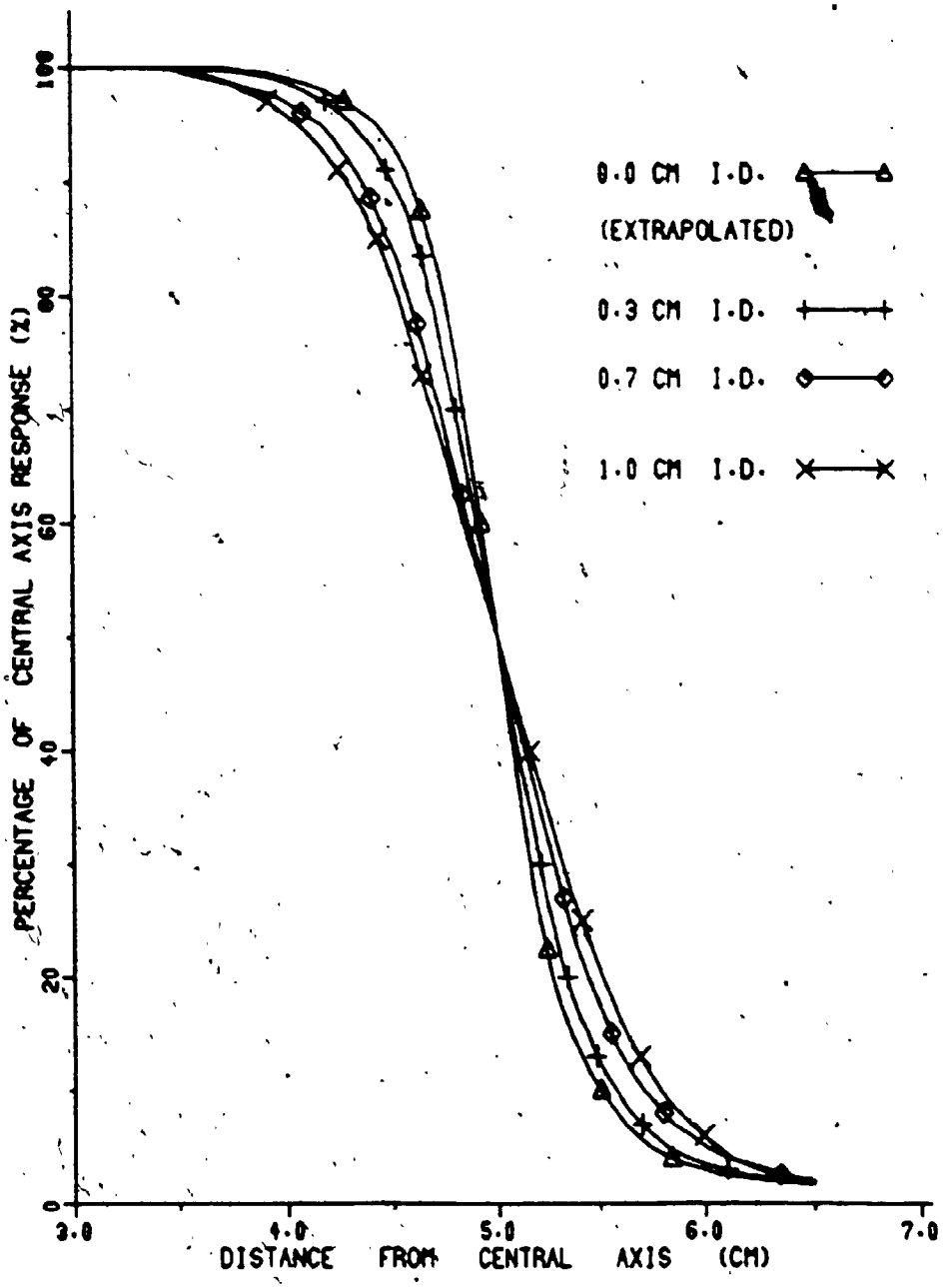

FIGURE 4.7

THE VARIATION OF THE PENUMBRAL DOSE DISTRIBUTION (IN CEDAR) WITH CHAMBER INSIDE DIAMETER FOR CO-60 BEAM

The penumbral widths, determined as a function of the chamber inside diameter from the measured penumbral distributions, are listed in Tables 4.7 and 4.8 for the cedar and balsa chambers respectively along with the parameters of the linear least squares fits. The measured P20-80 and P10-90 penumbral widths in cedar are illustrated as a function of chamber inside diameter for Co-60 in Figure 4.8. The effect of the chamber inside diameter is eliminated by extrapolating the linear least squares fit to zero inside diameter. This approach yields a first approximation to the primary penumbral dose width. The primary penumbral dose distribution, obtained from the primary penumbral dose widths for Co-60, is illustrated in Figure 4.7 along with the measured distributions.

The measured penumbral distributions for Co-60 using cedar- and balsa-walled ionization chambers show symmetry about the 50% dose level within the 20-80% dose level region. The penumbral widths beyond this region diverge significantly from symmetry with the lower dose level region showing the greater width.

Table 4.7

Penumbral Difference %	Inside Diameter (i.d.) of Ionization Chamber (cm)				Least Squares Fit	
					Slope	Intercept
	0.3	0.5	0.7	1.0		
	Penumbral Width (cm)				cm/ cm i.d.	(cm)
P50-98	0.92	1.02	1.14	1.20	0.41	0.82
P50-95	0.67	0.77	0.83	0.94	0.38	0.57
P50-93	0.59	0.68	0.74	0.85	0.36	0.49
P50-90	0.50	0.58	0.64	0.73	0.32	0.41
P50-85	0.39	0.46	0.52	0.58	0.27	0.32
P50-80	0.32	0.37	0.42	0.47	0.22	0.26
P50-70	0.20	0.24	0.27	0.31	0.16	0.16
P50-60	0.10	0.12	0.14	0.16	0.09	0.08
P50-40	0.10	0.12	0.14	0.16	0.09	0.08
P50-30	0.21	0.25	0.28	0.32	0.16	0.17
P50-20	0.34	0.40	0.44	0.51	0.24	0.27
P50-15	0.44	0.50	0.55	0.63	0.27	0.36
P50-10	0.58	0.65	0.71	0.79	0.30	0.50
P50-05	0.82	0.92	1.00	0.06	0.34	0.74
P20-80	0.66	0.77	0.86	0.98	0.46	0.53
P10-90	1.08	1.23	1.35	1.52	0.52	0.91

Table 4.7: Penumbral Width versus Chamber Inside Diameter for Co-60.

Medium: Cedar.

Table 4.8

Penumbral Difference %	Inside Diameter (i.d.) of Ionization Chamber (cm)			Least Squares Fit	
				Slope	Intercept
	0.5	0.7	1.0		
	Penumbral Width (cm)			cm/ cm i.d.	(cm)
P50-98	1.90	1.90	1.90	0.00	1.90
P50-95	1.34	1.38	1.43	0.18	1.25
P50-93	1.12	1.16	1.23	0.22	1.01
P50-90	0.90	0.94	1.02	0.24	0.78
P50-85	0.68	0.72	0.79	0.22	0.57
P50-80	0.54	0.57	0.63	0.18	0.45
P50-70	0.33	0.36	0.40	0.14	0.26
P50-60	0.16	0.18	0.20	0.08	0.12
P50-40	0.16	0.18	0.20	0.08	0.12
P50-30	0.34	0.37	0.40	0.12	0.28
P50-20	0.62	0.64	0.68	0.12	0.56
P50-15	0.78	0.83	0.88	0.20	0.69
P50-10	1.05	1.09	1.13	0.16	0.97
P50-07	1.34	I.36	1.39	0.10	1.29
P50-05	1.70	1.70	1.70	0.00	1.70
P20-80	1.16	1.21	1.31	0.30	1.01
P10-90	1.95	2.03	2.15	0.40	1.75

Table 4.8: Penumbral Width versus Chamber Inside Diameter for Co-60.

Medium: Balsa.

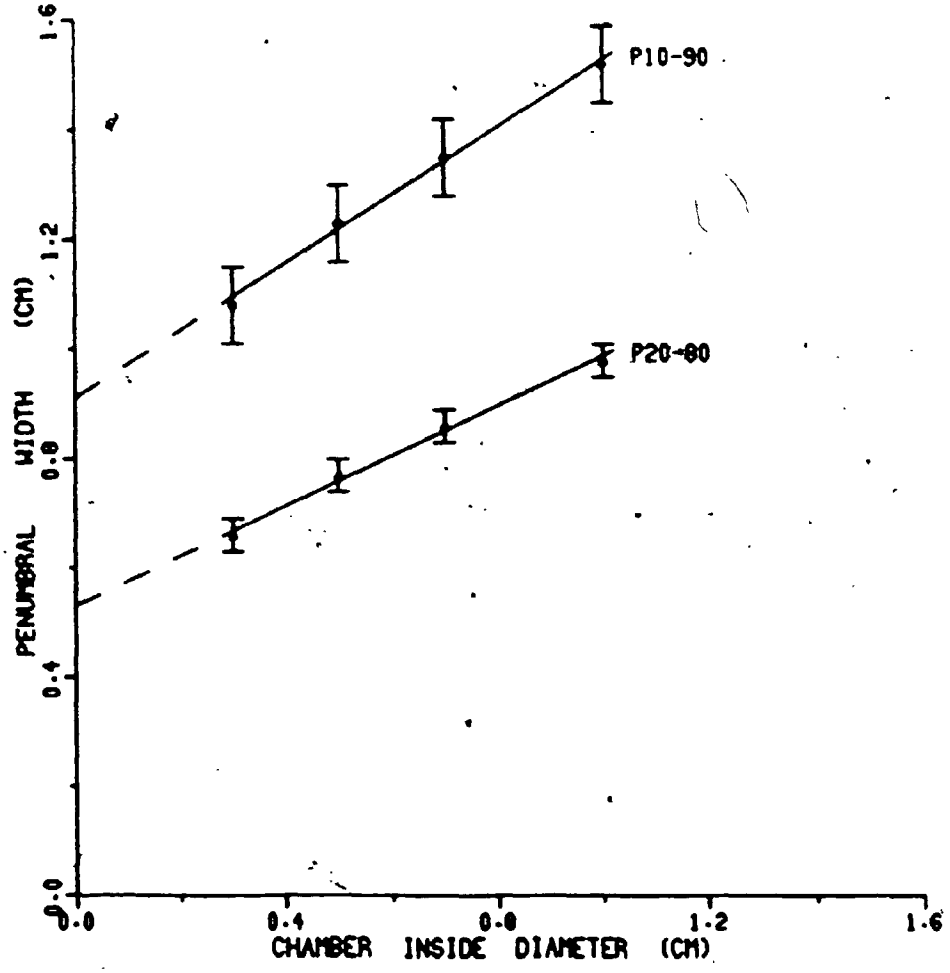

FIGURE 4.8

THE P20-80 AND P10-90 PENUMBRAL WIDTH VERSUS CHAMBER INSIDE DIAMETER FOR CO-60 BEAM. MEDIUM: CEDAR.

4.5.3 Low-Density Effects for 6-MV X Rays

The penumbral distributions for 6-MV x rays were also measured using cedar-walled ionization chambers having varying inside diameter. These distributions are similar to those illustrated in Figure 4.7 for Co-60. The measured penumbral distributions again showed increasing degradation with increasing chamber inside diameter.

The penumbral widths, determined as a function of the chamber inside diameter from the measured penumbral distributions, are listed in Table 4.9 for 6-MV x rays. The linear least squares fits for the dependence of the penumbral widths on the chamber inside diameter were extrapolated to zero inside diameter to eliminate the effect of the inside diameter of the ionization chamber. These results for the P20-80 and P10-90 penumbral widths are shown in Figure 4.9 for the 6-MV x rays. This approach yields the first approximation to the primary penumbral dose distribution.

The measured penumbral distributions for 6-MV x rays using cedar-walled ionization chambers showed symmetry about the 50% dose level only within the 30-70% dose level region. The penumbral widths beyond this region diverge significantly from symmetry with the lower dose level region again showing the greater width.

Table 4.9

Penumbral Difference (%)	Inside Diameter (i.d.) of Ionization Chamber (cm)				Least Squares Fit	
					Slope	Intercept
	0.3	0.5	0.7	1.0		
	Penumbral Width (cm)				cm/cm i.d.	(cm)
P50-98	1.61	1.67	1.73	1.83	0.31	1.51
P50-95	1.11	1.18	1.26	1.39	0.40	0.98
P50-93	0.89	0.97	1.06	1.19	0.43	0.76
P50-90	0.68	0.76	0.84	0.96	0.40	0.56
P50-85	0.49	0.56	0.63	0.72	0.33	0.39
P50-80	0.37	0.43	0.50	0.57	0.29	0.29
P50-70	0.22	0.27	0.31	0.37	0.21	0.16
P50-60	0.11	0.13	0.15	0.18	0.10	0.08
P50-40	0.11	0.13	0.15	0.18	0.10	0.08
P50-30	0.24	0.28	0.31	0.37	0.18	0.19
P50-20	0.46	0.50	0.53	0.60	0.20	0.40
P50-15	0.64	0.68	0.72	0.80	0.23	0.57
P50-10	0.93	1.00	1.06	1.13	0.28	0.85
P50-05	1.63	1.67	1.72	1.77	0.20	1.57
P20-80	0.83	0.93	1.03	1.17	0.49	0.69
P10-90	1.61	1.76	1.90	2.09	0.68	1.41

Table 4.9: Penumbral Width versus Chamber Inside Diameter for 6-MV X Rays.

Medium: Cedar.

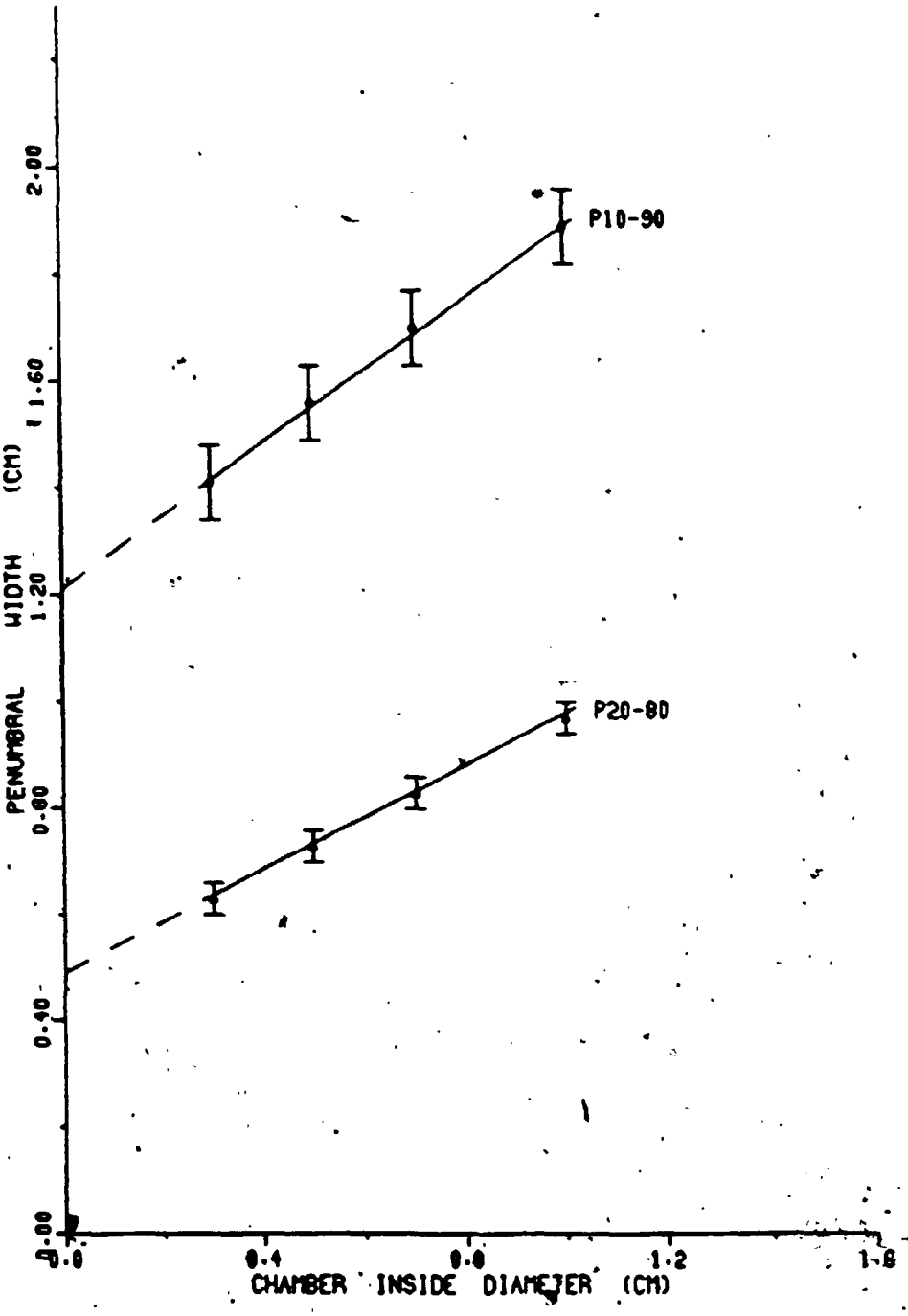

FIGURE 4.9

THE P20-80 AND P10-90 PENUMBRAL WIDTH VERSUS CHAMBER INSIDE DIAMETER FOR 6-MV X-RAY BEAM. MEDIUM: CEDAR

4.5.4 Energy Dependence in Cedar

The primary penumbral dose distributions in cedar for the Co-60, 6- and 31-MV x-ray beams are indicated in Figure 4.10. The widths of the primary penumbral dose distributions increase significantly with the beam energy.

The intercepts and the slopes of the linear least squares fits for the primary P20-80 and P10-90 penumbral dose widths in cedar are compared in Table 4.10 for the three beam energies. The intercepts for cedar are larger than the corresponding intercepts for lucite indicated in Table 4.4. The differences increase strongly with the beam energy.

The slopes are a measure of the degradation of the measured primary penumbral dose widths associated with the inside diameter of the ionization chamber. The slope of the P20-80 and P10-90 penumbral widths are approximately 0.5 cm/(cm inside diameter) and are in agreement with the slopes in Table 4.4 for lucite. Table 4.10 indicates that the slopes are independent of the beam energy as in the case for lucite.

In situations for which only one chamber inside diameter was used for the measurement of the primary penumbral dose distribution, mean slopes were used to correct the results to zero inside diameter. These situations included the

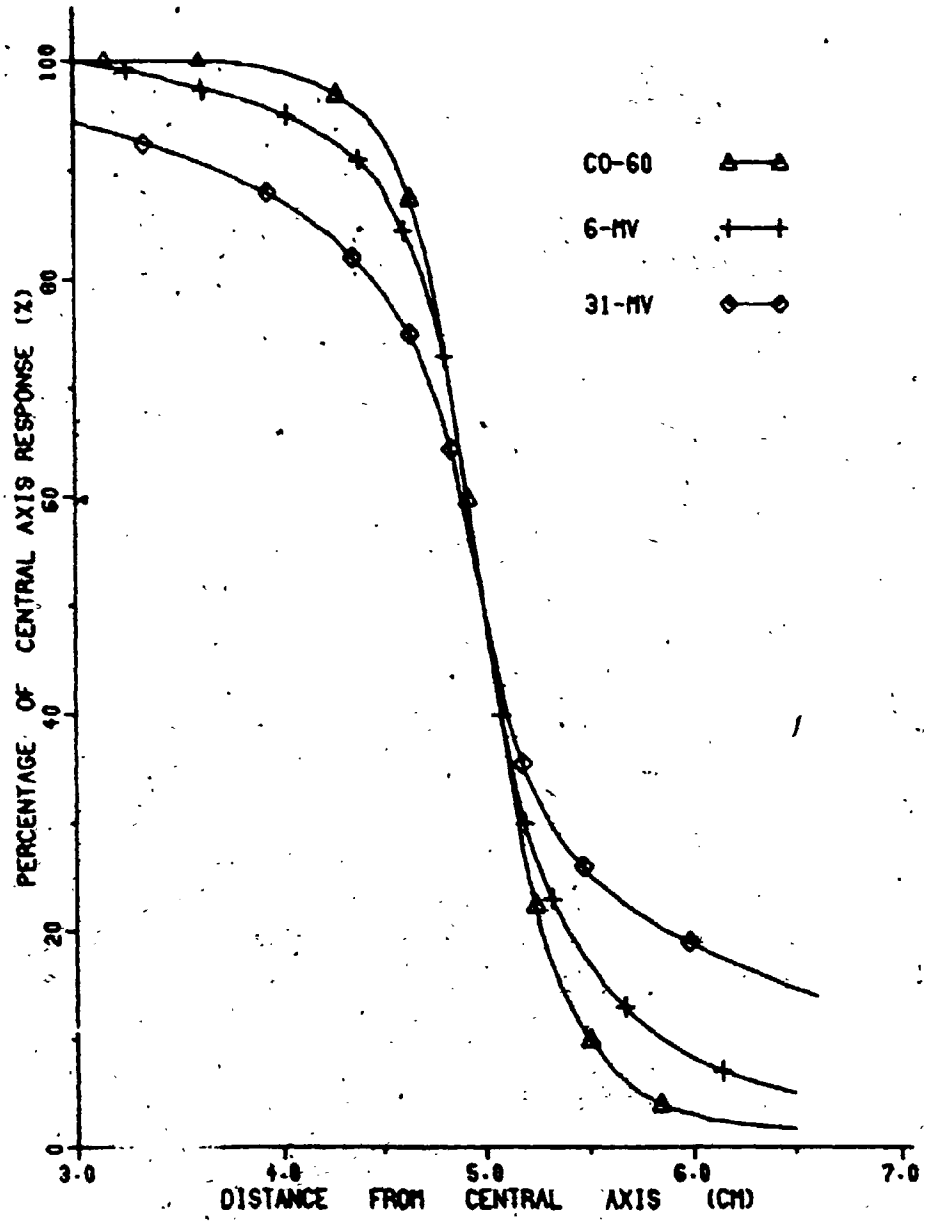

FIGURE 4.10

THE PRIMARY PENUMBRAL DOSE DISTRIBUTIONS IN LUNG TISSUE FOR CO-60, 6-MV AND 31-MV X-RAY BEAMS.

Table 4.10

Beam Energy	P20-80 Parameters		P10-90 Parameters	
	Intercept (cm)	Slope cm/cm i.d.	Intercept (cm)	Slope cm/cm i.d.
Co-60	0.53±.03	0.46±.05	0.91±.07	0.62±.13
6-MV X Rays	0.69±.03	0.49±.05	1.41±.07	0.68±.13
31-MV X Rays	1.42±.03		3.58±.07	

Table 4.10: The P20-80 and P10-90 Parameters of the Dose Distributions in Cedar as a Function of Beam Energy.

measurement of the primary penumbral dose distributions in balsa for 6-MV x rays and in cedar for 31-MV x rays.

4.6 High-Density Effect

Ionization chambers with copper walls were employed in this project to study the effect of a reduced lateral spread of the secondary electrons on the penumbral distribution of high-energy photon beams. The inside diameters of the ionization chambers were again varied from 0.3 to 1.4 cm to measure the penumbral region for Co-60, 6- and 31-MV x rays. The techniques, employed for media of low-electron density, were extended to the determination of the primary penumbral dose distribution in copper.

The measured penumbral distributions using the copper-walled chambers, are illustrated in Figure 4.11 for Co-60. Again, the measured penumbral distributions for 6- and 31-MV x rays are similar to those illustrated in Figure 4.11 for Co-60. The results indicate increased broadening of the penumbral distribution with chamber inside diameter for all beam energies. The penumbral widths, determined from these measured distributions, are listed in Tables 4.11, 4.12 and 4.13 for Co-60, 6- and 31-MV x rays respectively along with the parameters of the linear least squares fits of the penumbral width against chamber inside diameter. The P20-80 and P10-90 penumbral

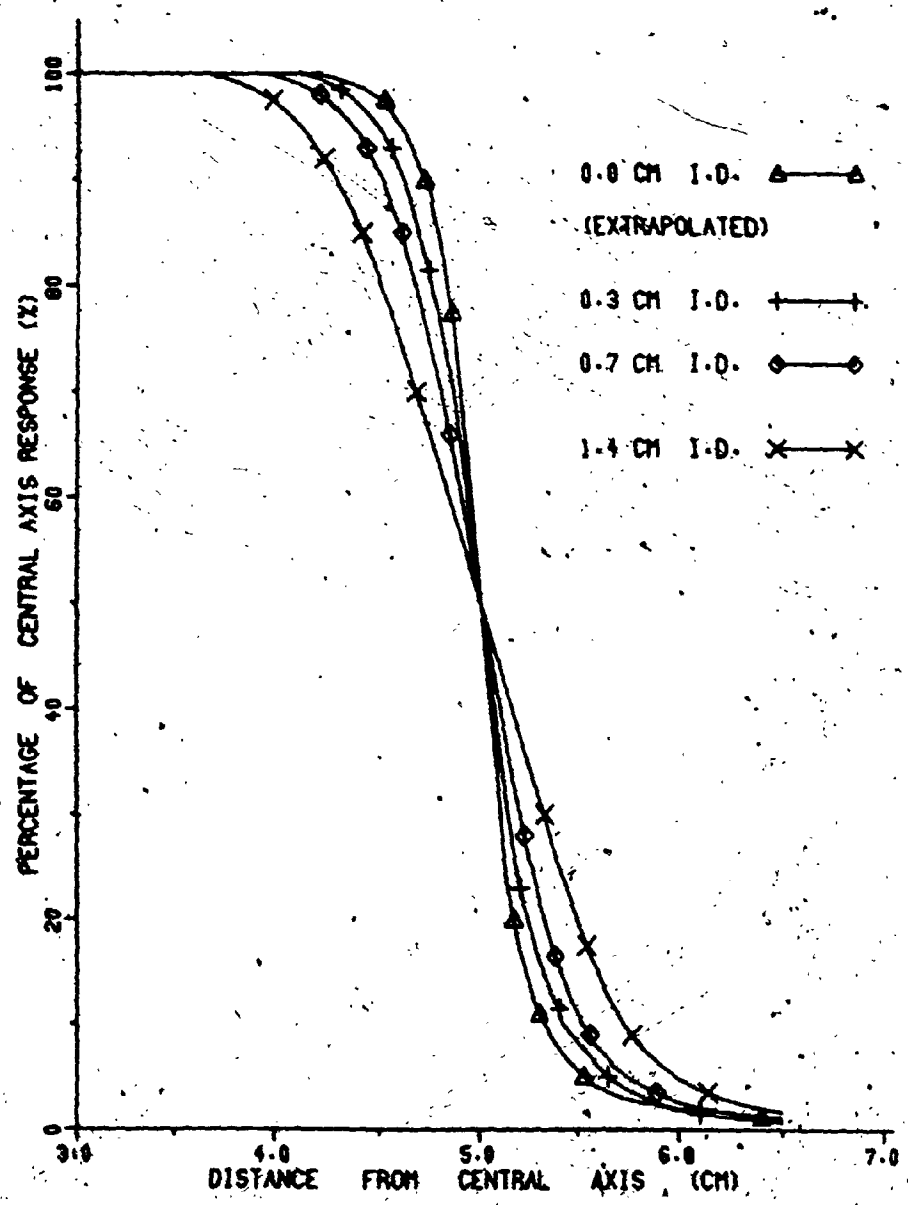

FIGURE 4.11

THE VARIATION OF THE PENUMBRAL DOSE DISTRIBUTION (IN COPPER) WITH CHAMBER INSIDE DIAMETER FOR CO-60 BEAM

Table 4.11

Penumbral Difference %	Inside Diameter (I.D.) of Ionization Chamber (cm)						Least Squares Fit	
	0.3	0.5	0.7	1.0	1.2	1.4	Slope	Intercept
	Penumbral Width (cm)						cm/cm i.d	(cm)
P50-98	0.64	0.70	0.78	0.88	0.97	1.06	0.38	0.52
P50-95	0.50	0.55	0.62	0.70	0.79	.87	0.33	0.39
P50-93	0.43	0.48	0.54	0.62	0.71	.80	0.33	0.32
P50-90	0.38	0.42	0.48	0.56	0.63	.71	0.30	0.28
P50-85	0.31	0.35	0.39	0.47	0.53	0.59	0.26	0.22
P50-80	0.25	0.29	0.32	0.39	0.45	0.49	0.22	0.18
P50-70	0.15	0.18	0.20	0.25	0.30	0.32	0.16	0.10
P50-60	0.07	0.09	0.10	0.13	0.15	0.16	0.08	0.05
P50-40	0.07	0.09	0.10	0.13	0.15	0.16	0.08	0.05
P50-30	0.14	0.18	0.20	0.25	0.30	0.32	0.16	0.10
P50-20	0.24	0.29	0.33	0.41	0.46	0.49	0.23	0.17
P50-15	0.32	0.36	0.41	0.50	0.56	0.60	0.27	0.23
P50-10	0.43	0.46	0.52	0.61	0.68	0.73	0.29	0.33
P50-05	0.65	0.67	0.73	0.81	0.88	0.99	0.30	0.53
P20-80	0.49	0.58	0.63	0.80	0.91	0.98	0.45	0.34
P10-90	0.81	0.88	1.00	1.17	1.31	1.44	0.59	0.61

Table 4.11: Penumbral Width versus Chamber Inside Diameter for Co-60.

Medium: Copper.

Table 4.12

Penumbral Difference (%)	Inside Diameter (I.D.) of Ionization Chamber (cm)						Least Squares Fit	
							Slope	Intercept
	0.3	0.5	0.7	1.0	1.2	1.4		
	Penumbral Width (cm)						cm/cm i.d.	(cm)
P50-98	0.50	0.57	0.66	0.83	0.95	1.08	0.52	0.32
P50-95	0.35	0.43	0.51	0.67	0.77	0.85	0.47	0.20
P50-93	0.30	0.38	0.46	0.61	0.70	0.80	0.46	0.15
P50-90	0.26	0.33	0.41	0.54	0.64	0.71	0.42	0.13
P50-85	0.21	0.27	0.34	0.45	0.54	0.61	0.37	0.09
P50-80	0.18	0.23	0.29	0.38	0.45	0.52	0.31	0.08
P50-70	0.12	0.15	0.19	0.25	0.30	0.35	0.21	0.05
P50-60	0.06	0.08	0.10	0.13	0.15	0.18	0.10	0.03
P50-40	0.06	0.08	0.10	0.13	0.15	0.18	0.10	0.03
P50-30	0.12	0.15	0.19	0.25	0.30	0.35	0.21	0.05
P50-20	0.20	0.25	0.30	0.38	0.46	0.53	0.30	0.10
P50-15	0.26	0.31	0.36	0.44	0.54	0.61	0.32	0.15
P50-10	0.35	0.40	0.47	0.55	0.63	0.73	0.34	0.24
P50-05	0.63	0.67	0.75	0.80	0.87	0.96	0.29	0.53
P50-03	1.35	1.35	1.35	1.35	1.35	1.35	0.00	1.35
P20-80	0.38	0.48	0.59	0.76	0.91	1.05	0.61	0.18
P10-90	0.61	0.73	0.88	1.09	1.27	1.44	0.76	0.36

Table 4.12: Penumbral width versus chamber inside diameter for 6-MV x rays.

Medium: Copper.

Table 4.13

Penumbral Difference (%)	Chamber Inside Diameter (I.D.) (cm)						Least Squares Fit	
	0.3	0.5	0.7	1.0	1.2	1.4	Slope	Intercept
	Penumbral Width (cm)						cm/ cm i.d	(cm)
P50-98	0.38	0.46	0.59	0.72	0.81	0.88	0.47	0.24
P50-95	0.32	0.39	0.50	0.63	0.72	0.79	0.44	0.18
P50-93	0.29	0.35	0.46	0.59	0.68	0.75	0.43	0.15
P50-90	0.25	0.31	0.41	0.54	0.62	0.69	0.41	0.12
P50-85	0.21	0.26	0.34	0.47	0.53	0.60	0.37	0.09
P50-80	0.17	0.22	0.29	0.39	0.45	0.52	0.32	0.07
P50-70	0.11	0.15	0.19	0.26	0.30	0.34	0.21	0.04
P50-60	0.05	0.07	0.10	0.13	0.15	0.17	0.11	0.02
P50-40	0.05	0.07	0.10	0.13	0.15	0.17	0.11	0.02
P50-30	0.10	0.14	0.19	0.26	0.29	0.34	0.22	0.03
P50-20	0.18	0.24	0.29	0.39	0.44	0.52	0.30	0.09
P50-15	0.25	0.31	0.37	0.47	0.52	0.60	0.31	0.16
P50-10	0.37	0.44	0.48	0.57	0.63	0.70	0.29	0.28
P50-07	0.54	0.56	0.60	0.69	0.74	0.86	0.28	0.43
P50-05	1.20	1.20	1.20	1.12	1.20	1.20	0.00	1.20
P20-80	0.35	0.46	0.58	0.78	0.89	1.04	0.63	0.15
P10-90	0.62	0.75	0.89	1.11	1.25	1.39	0.71	0.40

Table 4.13: Penumbral Width versus Chamber Inside Diameter for 31-MV X Rays.

Medium: Copper.

widths are indicated in Figures 4.12, 4.13 and 4.14 for Co-60, 6- and 31-MV x rays respectively. The linear least squares fits are indicated by the solid lines in these figures while the broken lines represent the linear extrapolations to zero inside diameter. The slopes and intercepts of the linear least squares fits for the P20-80 and P10-90 penumbral widths are summarized in Table 4.14. The standard errors of the slopes are +/-0.05 and +/-0.13 cm/(cm inside diameter) for the P20-80 and P10-90 penumbral widths respectively. Again, these slopes which indicate the degradation associated with the chamber inside diameter, are nearly independent of the beam energy.

The measured distributions for Co-60, 6- and 31-MV x rays are symmetric about the 50% dose level as indicated in Tables 4.11, 4.12 and 4.13. Again, the symmetry diverges significantly beyond the 10-90% dose region with the lower dose region showing the greater width.

The intercepts yield a first approximation to the primary penumbral widths. The extrapolated primary penumbral dose distributions in copper are obtained from these intercepts listed in Tables 4.11, 4.12 and 4.13 for Co-60, 6- and 31-Mv x rays respectively. The extrapolated primary penumbral dose distribution in copper is indicated for Co-60 in Figure 4.12. The extrapolated primary penumbral dose distributions for 6- and 31-MV x rays are similar while that for Co-60 is significantly broader.

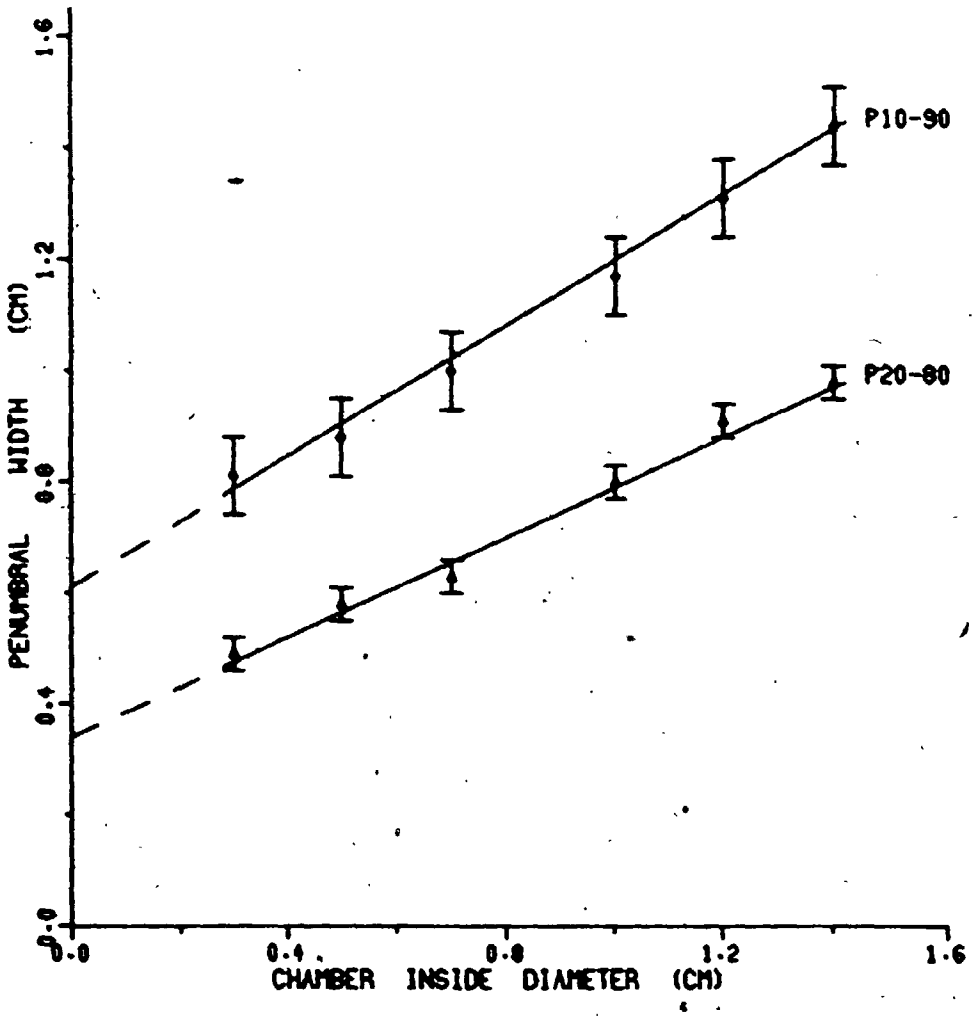

FIGURE 4.12

THE P20-80 AND P10-90 PENUMBRAL WIDTH VERSUS CHAMBER INSIDE DIAMETER FOR CO-60 BEAM. MEDIUM: COPPER

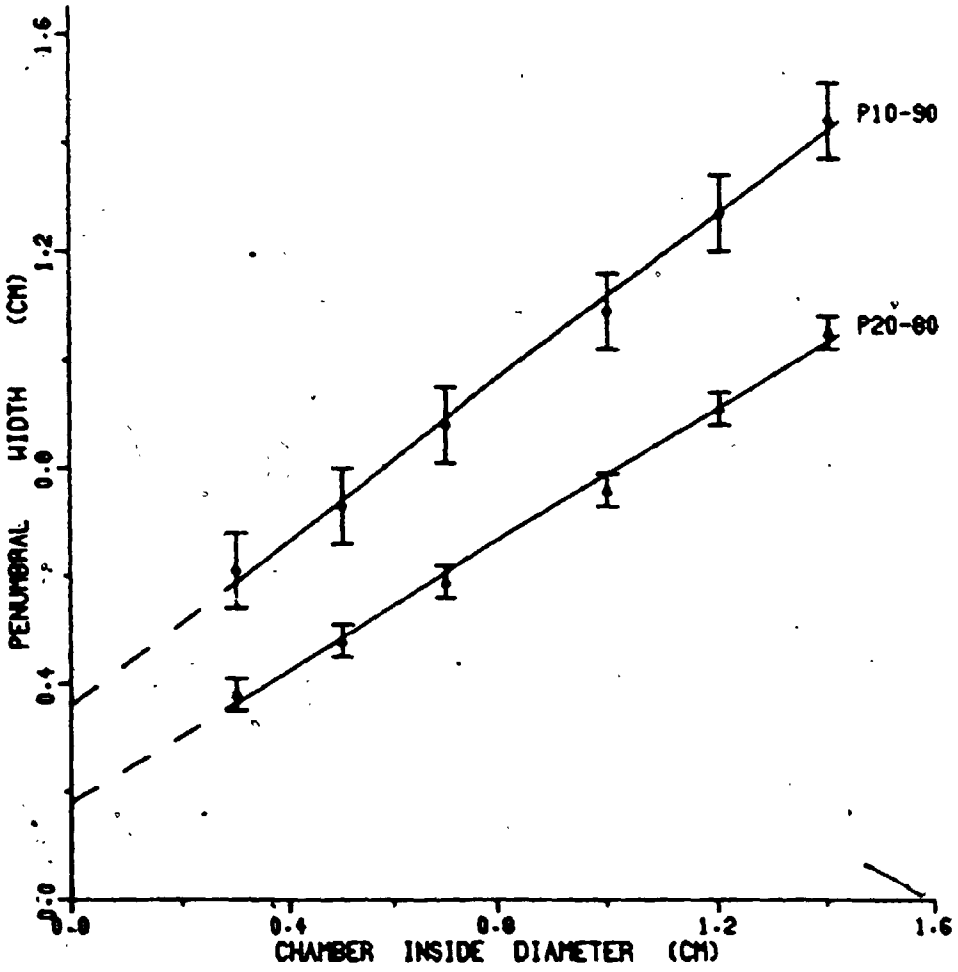

FIGURE 4.13

THE P20-80 AND P10-90 PENUMBRAL WIDTH VERSUS CHAMBER INSIDE DIAMETER FOR 6-MV X-RAY BEAM. MEDIUM: COPPER

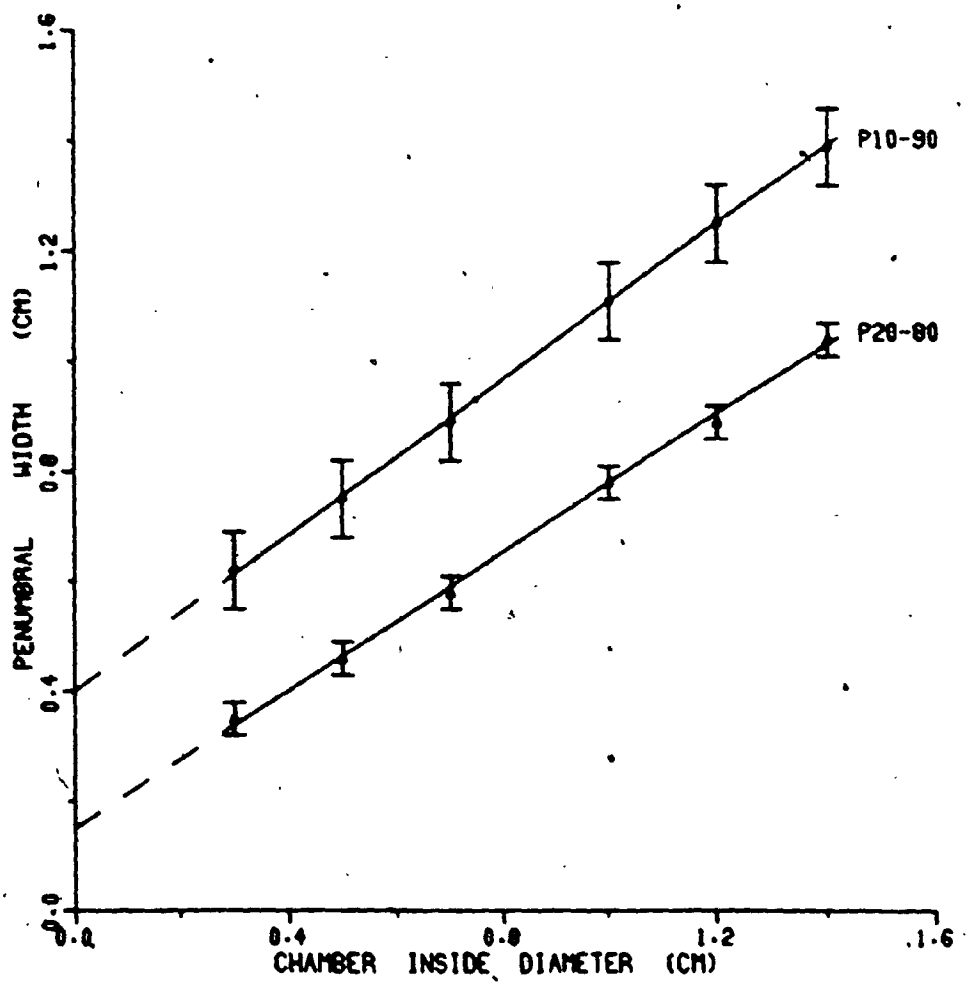

FIGURE 4.14

THE P20-80 AND P10-90 PENUMBRAL WIDTH VERSUS CHAMBER INSIDE DIAMETER FOR 31-MV X-RAY BEAM. MEDIUM: COPPER

Table 4.14

Beam Energy	P20-80 Parameters		P10-90 Parameters	
	Intercept	Slope	Intercept	Slope
Co-60	0.34±.03	0.45±.05	0.61±.07	0.59±.13
6-MV X Rays	0.18±.03	0.61±.05	0.36±.07	0.76±.13
31-MV X Rays	0.15±.03	0.63±.05	0.40±.07	0.71±.13

Table 4.14: The Primary Penumbral Widths of the Penumbral Dose Distribution in Copper as a Function of Beam Energy.

4.7 Primary Penumbral Photon-Fluence Distributions

The ionometric extrapolation technique was used to determine the primary penumbral dose distributions in equilibrium volumes of lucite, cedar, balsa and copper for Co-60, 6- and 31-MV x rays. The primary penumbral dose widths corresponding to these distributions are listed as a function of the electon density, relative to water, of the chamber-wall material in Tables 4.15, 4.16 and 4.17 for Co-60, 6- and 31-MV x rays respectively.

The primary penumbral dose widths are observed to increase with decreasing electron density. For infinite electron density, the lateral spread of the secondary electrons is reduced to zero. When the primary penumbral dose widths are plotted against the reciprocal of the electron density, an extrapolation to infinite electron density is practical. The P20-80 and P10-90 penumbral dose widths as a function of the reciprocal of the relative electron density of the wall material, are indicated for Co-60, 6- and 31-MV x rays in Figures 4.15, 4.16 and 4.17 respectively. The standard deviations are +/- 0.03 cm and +/- 0.07 cm for the P20-80 and P10-90 primary penumbral dose widths. The error bars are one standard deviation.

Table 4.15

Penumbral Difference	Chamber Wall Electron Density Relative to Water				Least Squares Fit	
	Cu 7.35	Lu 1.15	Ce 0.32	Ba 0.16	Slope	Intercept
	Reciprocal of Density					
	0.14	0.87	3.13	6.25		
(%)	Penumbral Intercepts (cm)				(cm)	(cm)
P50-98	0.52	0.55	0.82	1.50	0.16	0.42
P50-95	0.39	0.45	0.57	1.08	0.11	0.33
P50-93	0.32	0.40	0.49	0.90	0.09	0.29
P50-90	0.28	0.34	0.41	0.70	0.07	0.26
P50-85	0.22	0.27	0.32	0.53	0.05	0.21
P50-80	0.18	0.21	0.26	0.40	0.04	0.17
P50-70	0.10	0.14	0.16	0.25	0.02	0.10
P50-60	0.05	0.07	0.08	0.12	0.01	0.05
P50-40	0.05	0.07	0.08	0.12	0.01	0.05
P50-30	0.10	0.13	0.17	0.25	0.02	0.10
P50-20	0.17	0.21	0.27	0.44	0.04	0.16
P50-15	0.23	0.26	0.36	0.62	0.06	0.20
P50-10	0.33	0.33	0.50	0.80	0.08	0.28
P50-05	0.53	0.51	0.74	1.37	0.14	0.42
P20-80	0.34	0.42	0.53	0.84	0.08	0.33
P10-90	0.61	0.67	0.91	1.50	0.15	0.54

Table 4.15: Co-60 Beam Primary Penumbral Width as a Function of the Reciprocal of Chamber-Wall Relative Electron Density.

Table 4.16

Penumbral Difference	Chamber Wall Electron Density Relative to Water				Least Squares Fit	
	Cu 7.35	Lu 1.15	Ce 0.32	Ba 0.16	Slope	Intercept
	Reciprocal of Density					
	0.14	0.87	3.13	6.25		
(%)	Penumbral Intercepts (cm)				(cm)	(cm)
P50-98	0.32	0.55	1.51	2.56	0.37	0.27
P50-95	0.20	0.36	0.98	1.75	0.27	0.16
P50-93	0.15	0.31	0.76	1.39	0.20	0.13
P50-90	0.13	0.24	0.56	1.06	0.15	0.10
P50-85	0.09	0.17	0.39	0.70	0.10	0.08
P50-80	0.08	0.13	0.29	0.48	0.07	0.07
P50-70	0.05	0.08	0.16	0.25	0.03	0.05
P50-60	0.03	0.04	0.08	0.13	0.02	0.03
P50-40	0.03	0.04	0.08	0.13	0.02	0.03
P50-30	0.05	0.08	0.19	0.27	0.04	0.05
P50-20	0.10	0.18	0.40	0.68	0.09	0.09
P50-15	0.15	0.27	0.57	1.08	0.15	0.13
P50-10	0.24	0.41	0.85	1.71	0.24	0.18
P50-05	0.53	0.77	1.57	2.83	0.38	0.45
P20-80	0.18	0.32	0.69	1.16	0.16	0.17
P10-90	0.36	0.64	1.41	2.77	0.39	0.28

Table 4.16: 6-MV X Rays Primary Penumbral Width as a Function of the Reciprocal of Chamber-Wall Relative Electron Density.

Table 4.17

Penumbral Difference	Chamber Wall Electron Density Relative to Water			Least Squares Fit	
	Cu 7.35	Lu 1.15	Ce 0.32	Slope	Intercept
	Reciprocal of Density				
	0.14	0.87	3.13		
(%)	Penumbral Intercepts (cm)			(cm)	(cm)
P50-98	0.24	1.37	2.96	0.86	0.34
P50-95	0.18	0.79	2.15	0.65	0.15
P50-93	0.15	0.64	1.73	0.52	0.13
P50-90	0.12	0.47	1.31	0.39	0.09
P50-85	0.09	0.30	0.84	0.25	0.07
P50-80	0.07	0.21	0.55	0.16	0.06
P50-70	0.04	0.12	0.25	0.09	0.03
P50-60	0.02	0.05	0.11	0.03	0.02
P50-40	0.02	0.05	0.11	0.03	0.02
P50-30	0.03	0.05	0.31	0.09	0.03
P50-20	0.09	0.28	0.87	0.26	0.05
P50-15	0.16	0.45	1.45	0.44	0.09
P50-10	0.28	0.78	2.27	0.66	0.19
P50-07	0.43	1.31	3.29	0.94	0.38
P50-05	1.20	2.46	4.20	0.95	1.31
P20-80	0.15	0.49	1.42	0.42	0.10
P10-90	0.40	1.26	3.58	1.05	0.29

Table 4.17: 31-MV X Rays Primary Penumbral Width as a Function of the Reciprocal of Chamber-Wall Relative Electron Density.

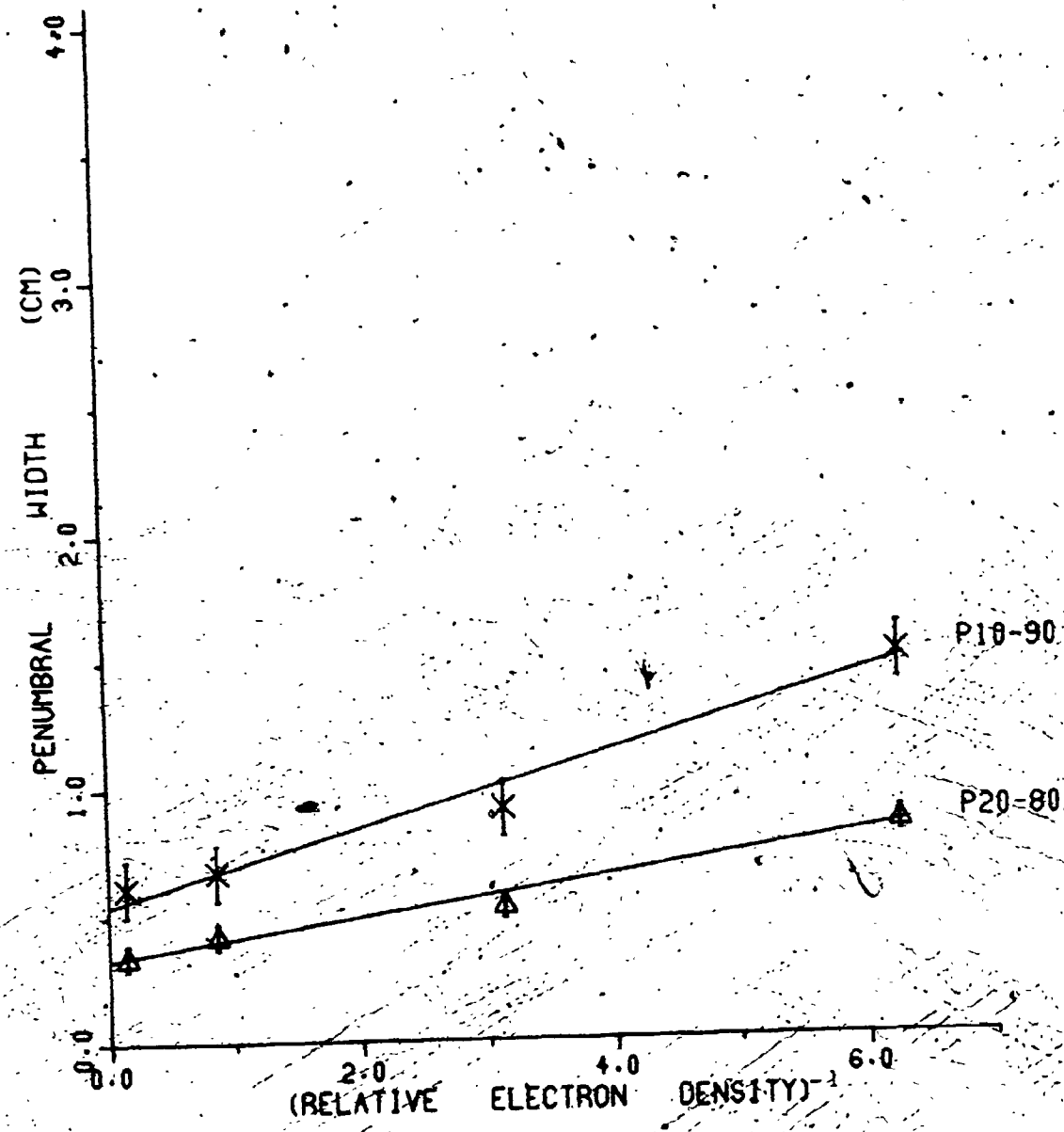

FIGURE 4.15

P20-80 AND P10-90 PRIMARY PENUMBRAL WIDTHS VERSUS RECIPROCAL OF RELATIVE ELECTRON DENSITY FOR CO-60

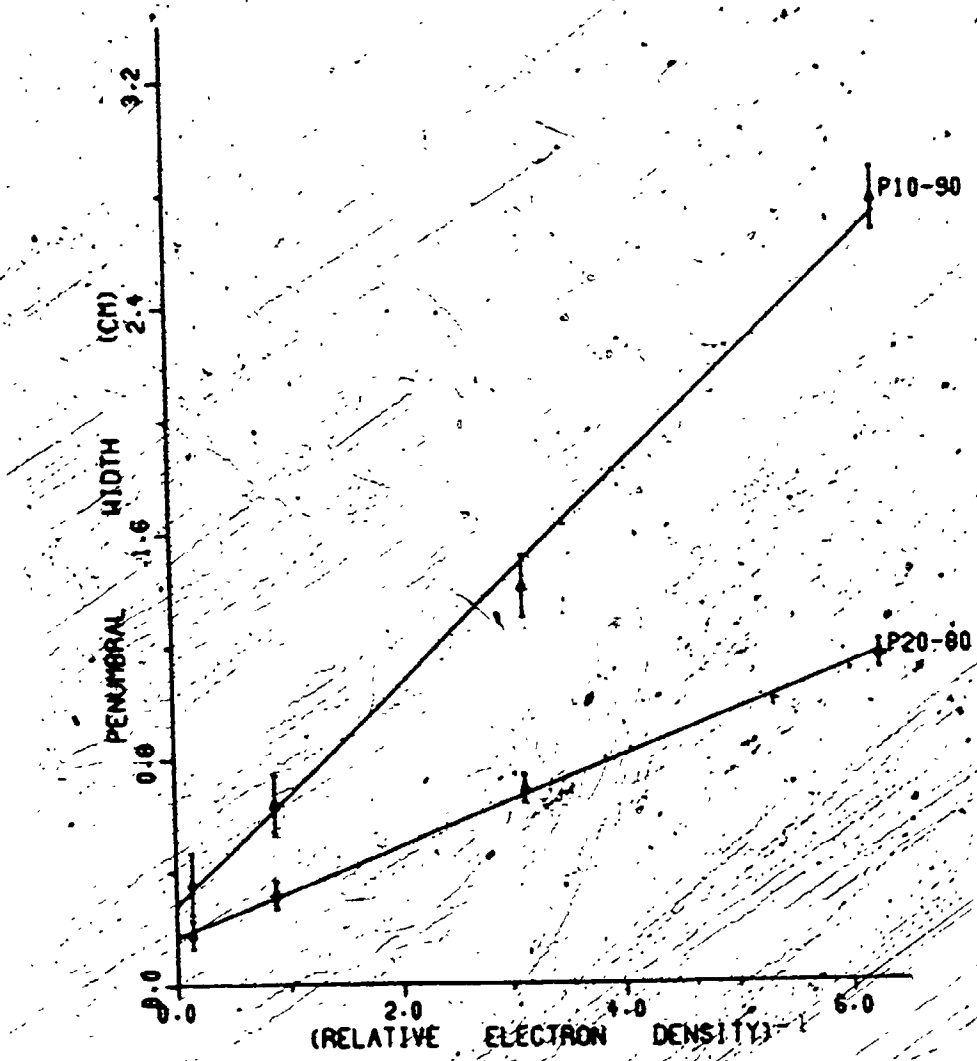

FIGURE 4.16

P20-80 AND P10-90 PRIMARY PENUMBRAL WIDTHS VERSUS RECIPROCAL OF RELATIVE ELECTRON DENSITY FOR 6-MV X RAYS

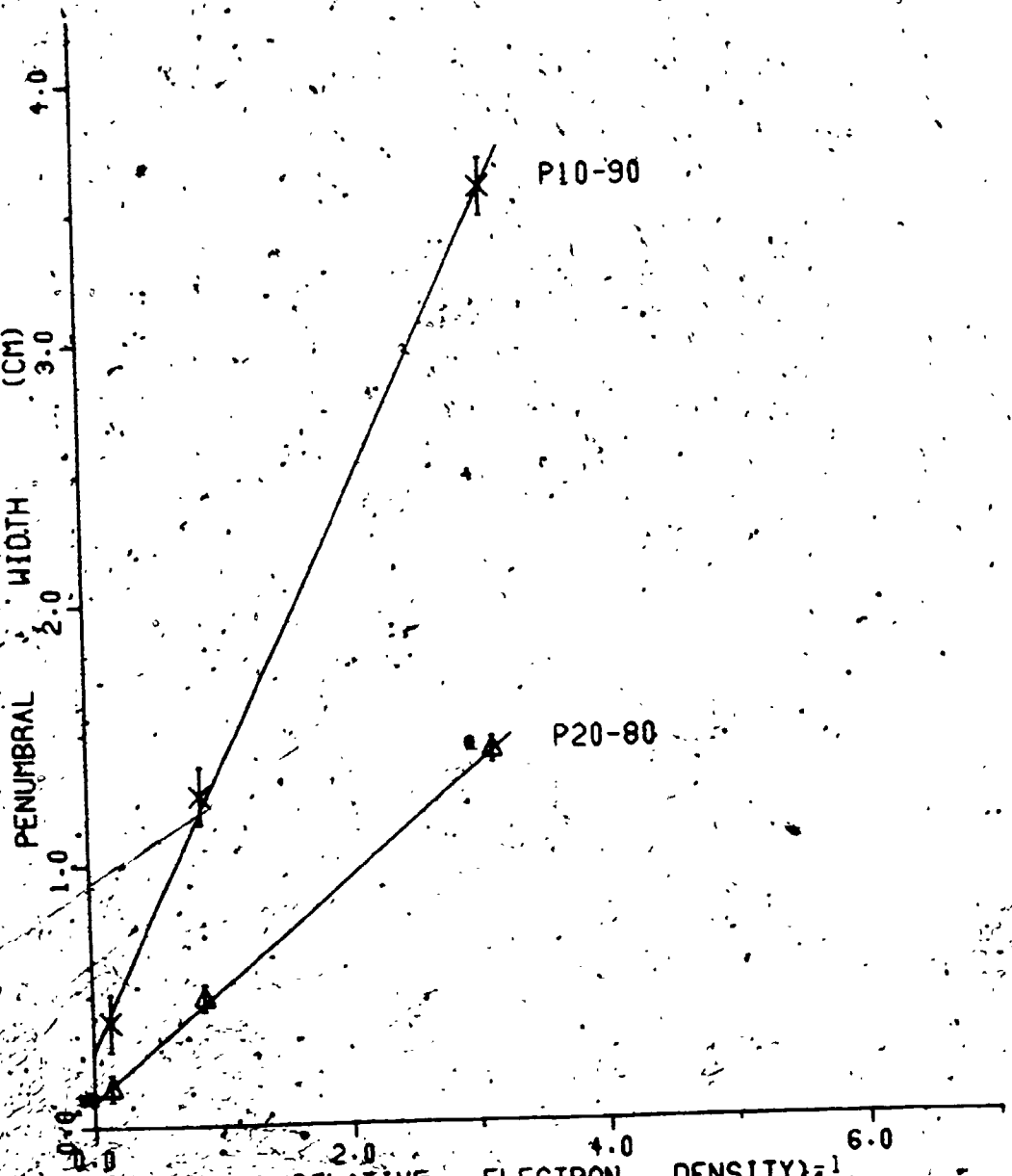

FIGURE 4.17

P20-80 AND P10-90 PRIMARY PENUMBRAL WIDTHS VERSUS RECIPROCAL OF RELATIVE ELECTRON DENSITY FOR 31-MV X RAYS

The intercepts and slopes of the linear least squares fits for the dependence of the P20-80 and P10-90 primary penumbral dose widths on the reciprocal of the relative electron density are listed in Table 4.18. The intercept, corresponding to infinite electron density, indicates the width of the primary penumbral photon-fluence distribution while the slope indicates the broadening of the primary penumbral dose widths with decreasing electron density.

The intercepts of the linear least squares fits for a distribution of penumbral widths can be used to determine the primary penumbral dose distributions in a medium of infinite electron density. The penumbral model indicates that the electron ranges and lateral spreads are reduced to zero in this case and the primary penumbral dose distribution is equivalent to the kerma or photon-fluence distribution. These distributions, based on the intercepts in Tables 4.15, 4.16 and 4.17, are indicated for Co-60, 6- and 31-MV x rays in Figure 4.18. These are the fitst published penumbral photon-fluence distributions. The primary penumbral photon-fluence distribution for 31-MV x rays is approximately equivalent to that for 6-MV x rays. Both accelerator distributions are significantly narrower than the corresponding distribution for Co-60.

Table 4.18

Beam Energy	P20-80 Parameters		P10-90 Parameters	
	Intercept (cm)	Slope	Intercept (cm)	Slope
Co-60	0.32±.03	0.08±.02	0.53±.07	0.15±.04
6-MV X Rays	0.17±.03	0.16±.02	0.28±.07	0.39±.04
31-MV X Rays	0.11±.03	0.42±.03	0.29±.07	1.05±.07

Table 4.18: The Photon-Fluence Primary Penumbral Widths as a Function of Beam Energy.

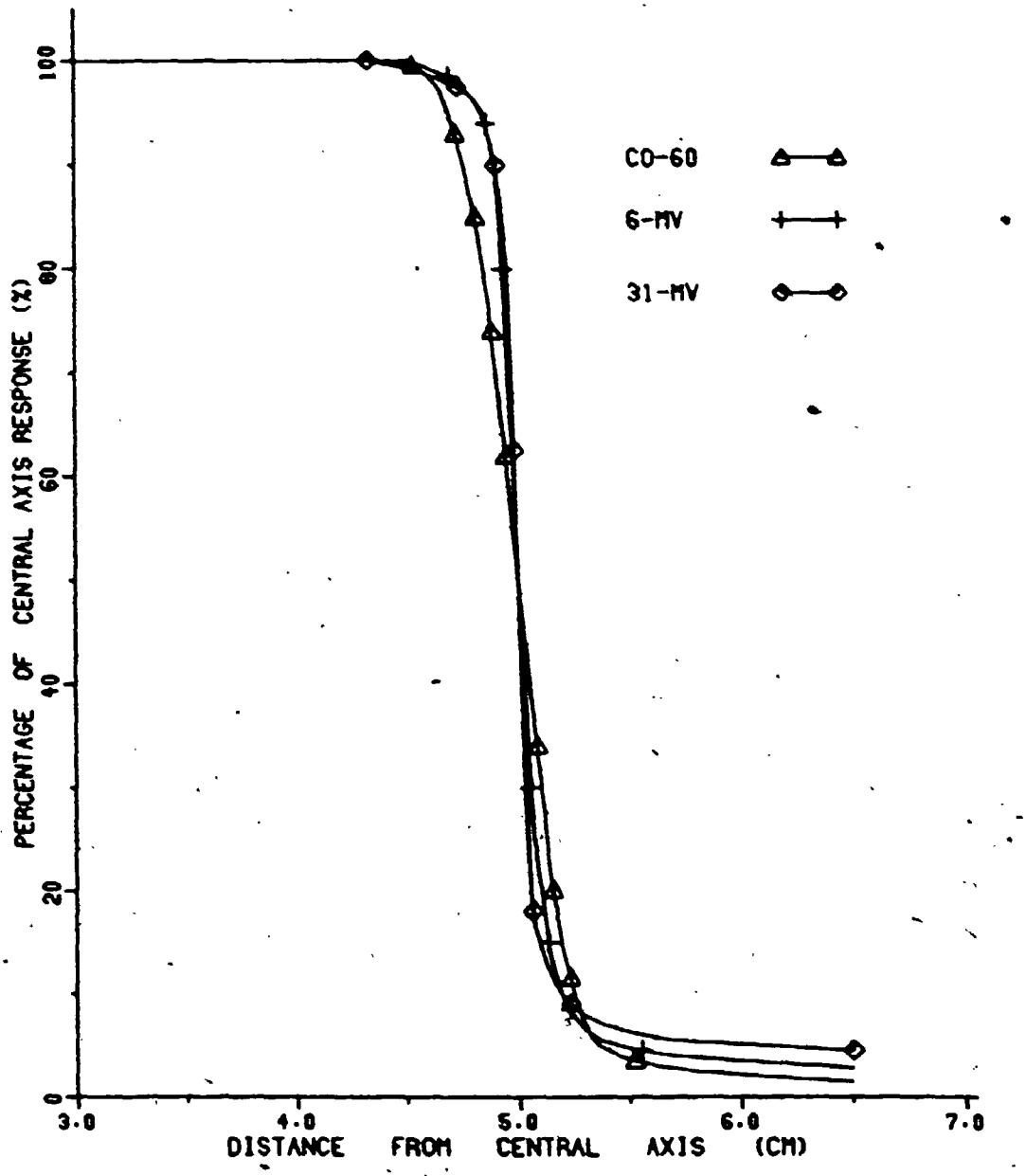

FIGURE 4.18

THE PRIMARY PENUMBRAL PHOTON-FLUENCE DISTRIBUTIONS FOR CO-60, 6- AND 31-MV X RAYS

4(8) Electron-Density Effect

The primary penumbral photon-fluence distributions and the primary penumbral dose distributions in both soft tissue and lung are compared for Co-60, 6- and 31-MV x rays in Figures 4.19, 4.20 and 4.21 respectively. These primary distributions were obtained by extrapolation to zero inside diameter. The broadening of the primary penumbral distributions with decreasing electron density is indicated at all beam energies. These figures indicate that the lateral spread of the secondary electrons increases with decreasing electron density and with increasing photon beam energy.

The P20-80 primary penumbral dose widths for Co-60 are compared for varying wall materials in Figure 4.22. The results for the P10-90 primary penumbral widths for Co-60, and the P20-80 and P10-90 primary penumbral widths for both 6- and 31-MV x rays are similar to those illustrated in Figure 4.22. The dependence of the P20-80 and P10-90 penumbral widths on the inside diameter of the ionization chamber is approximately independent of the material of the chamber wall for the three photon beam energies.

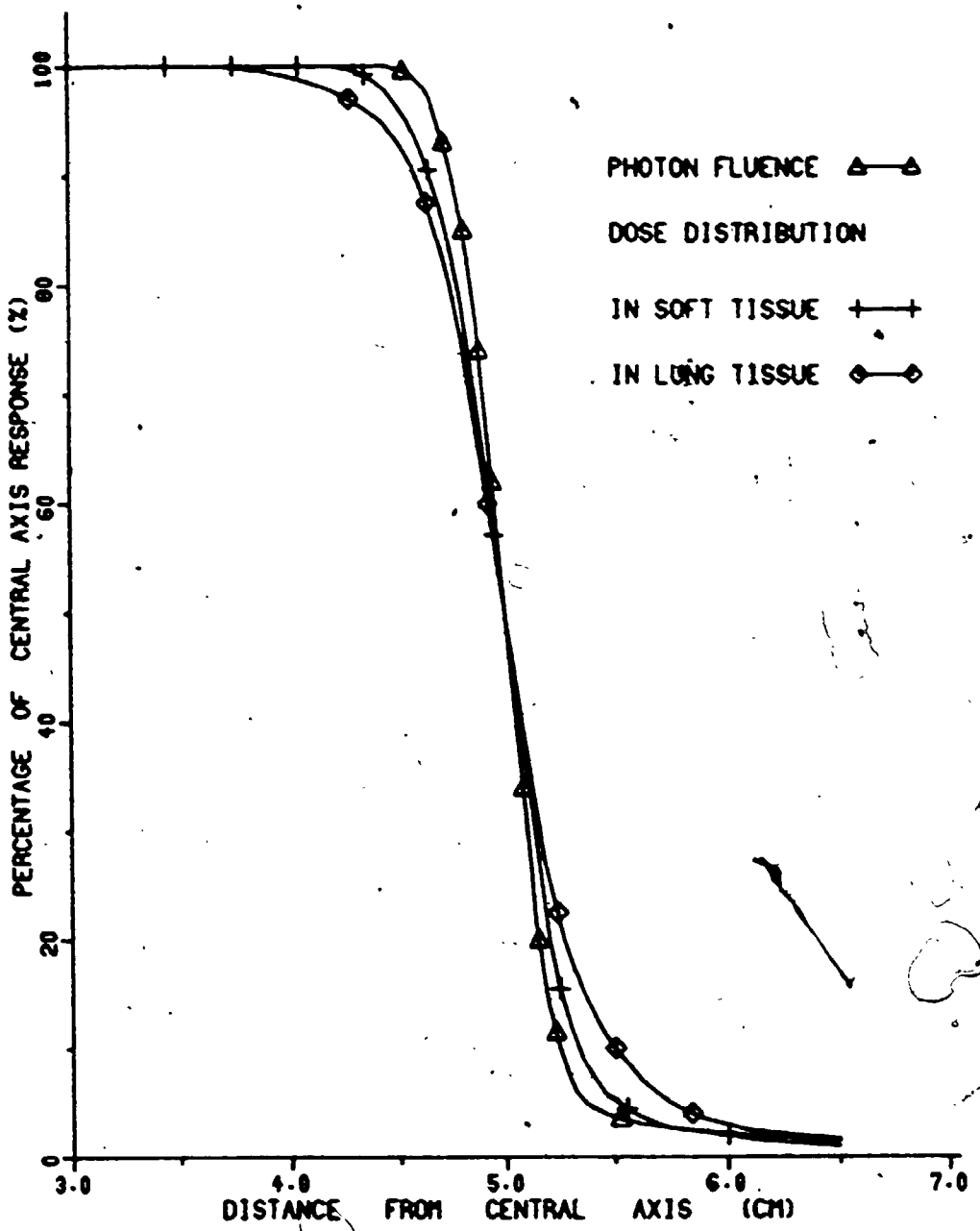

FIGURE 4.19

CO-60 PRIMARY PENUMBRAL PHOTON-FLUENCE DISTRIBUTION AND THE PRIMARY PENUMBRAL DOSE DISTRIBUTIONS IN SOFT TISSUE AND LUNG

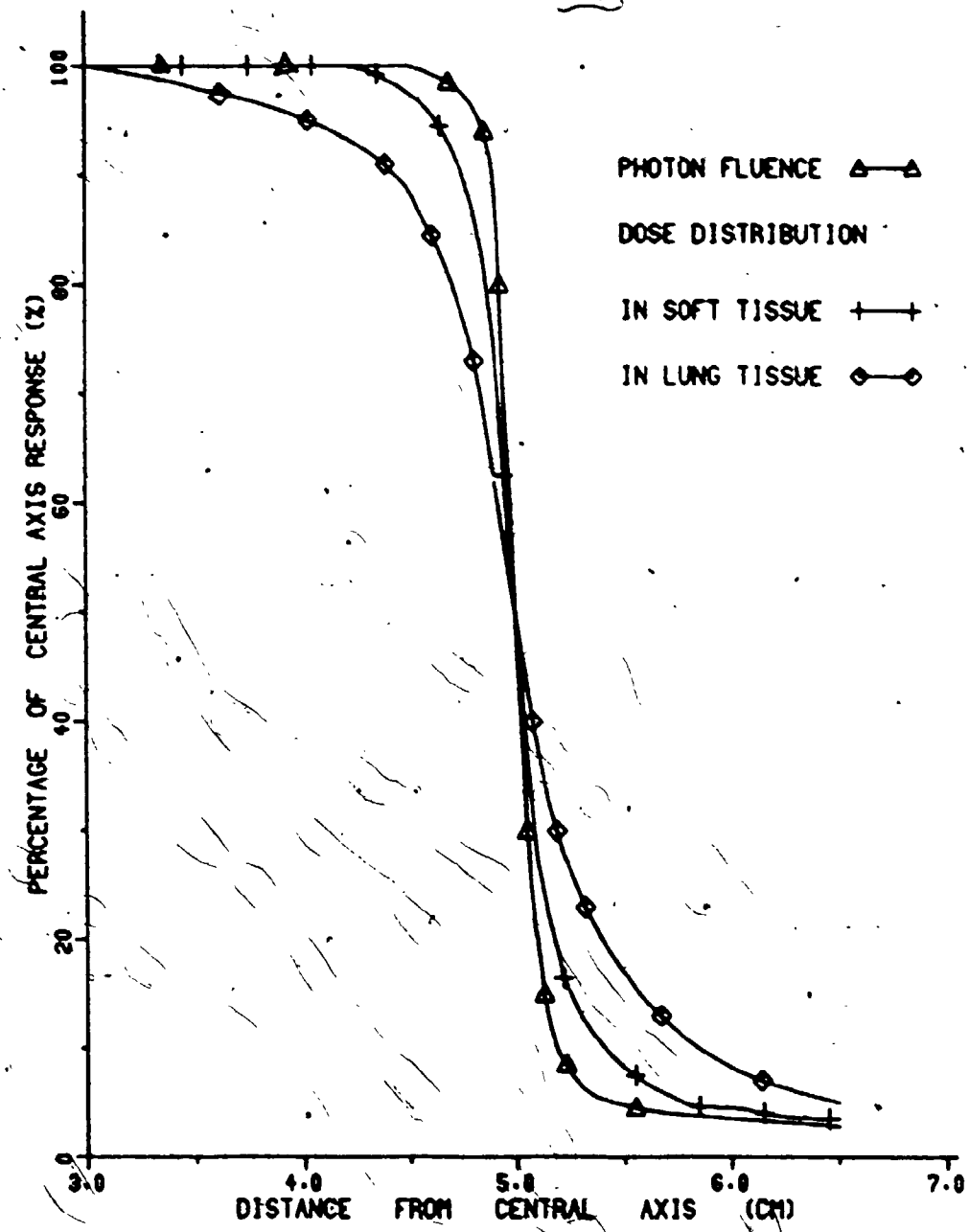

FIGURE 4.20

6-MV X-RAY PRIMARY PENUMBRAL PHOTON-FLUENCE DISTRIBUTION AND THE PRIMARY PENUMBRAL DOSE DISTRIBUTIONS IN SOFT TISSUE AND LUNG

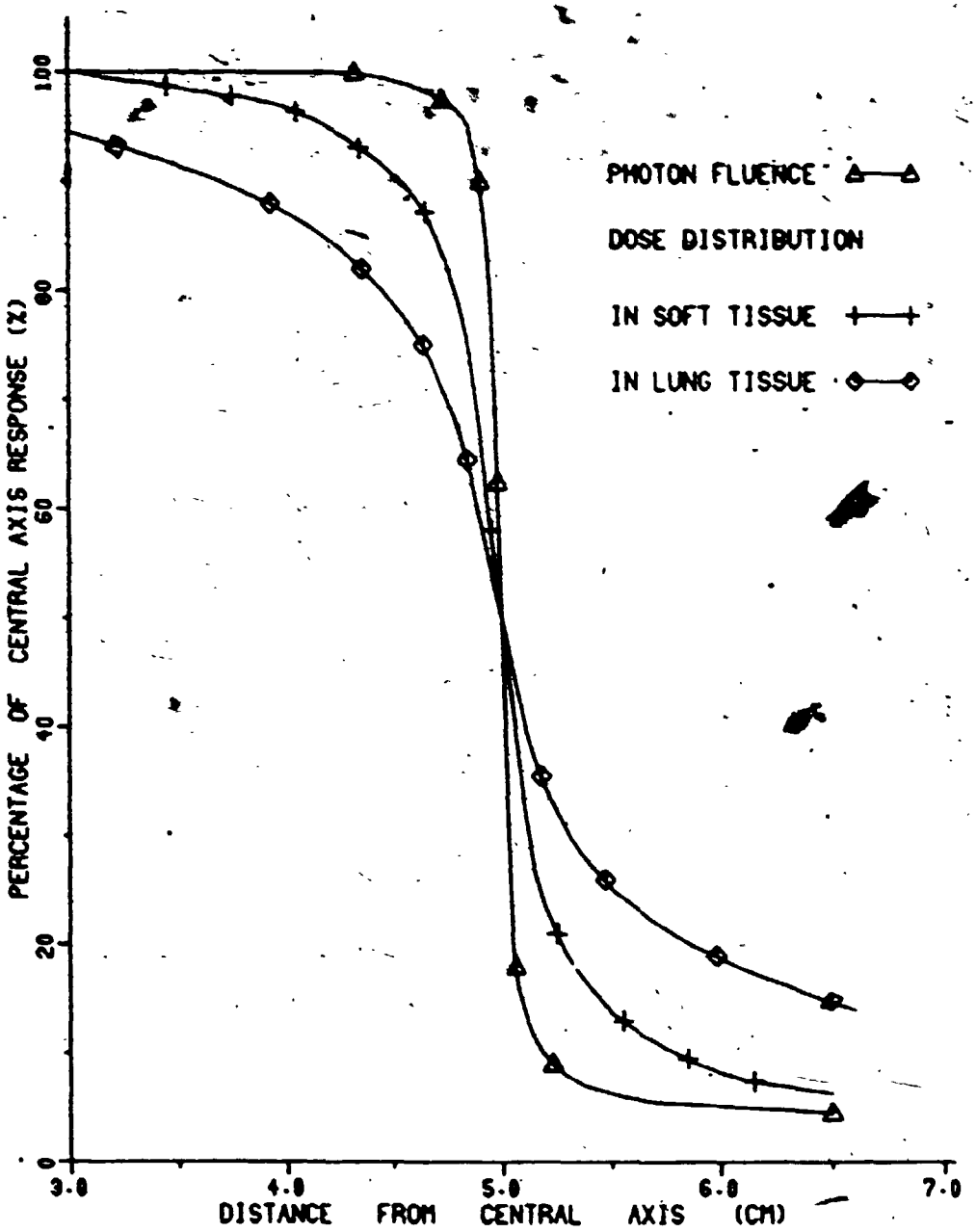

FIGURE 4.21

31-MV X-RAY PRIMARY PENUMBRAL PHOTON-FLUENCE DISTRIBUTION AND THE PRIMARY PENUMBRAL DOSE DISTRIBUTIONS IN SOFT TISSUE AND LUNG

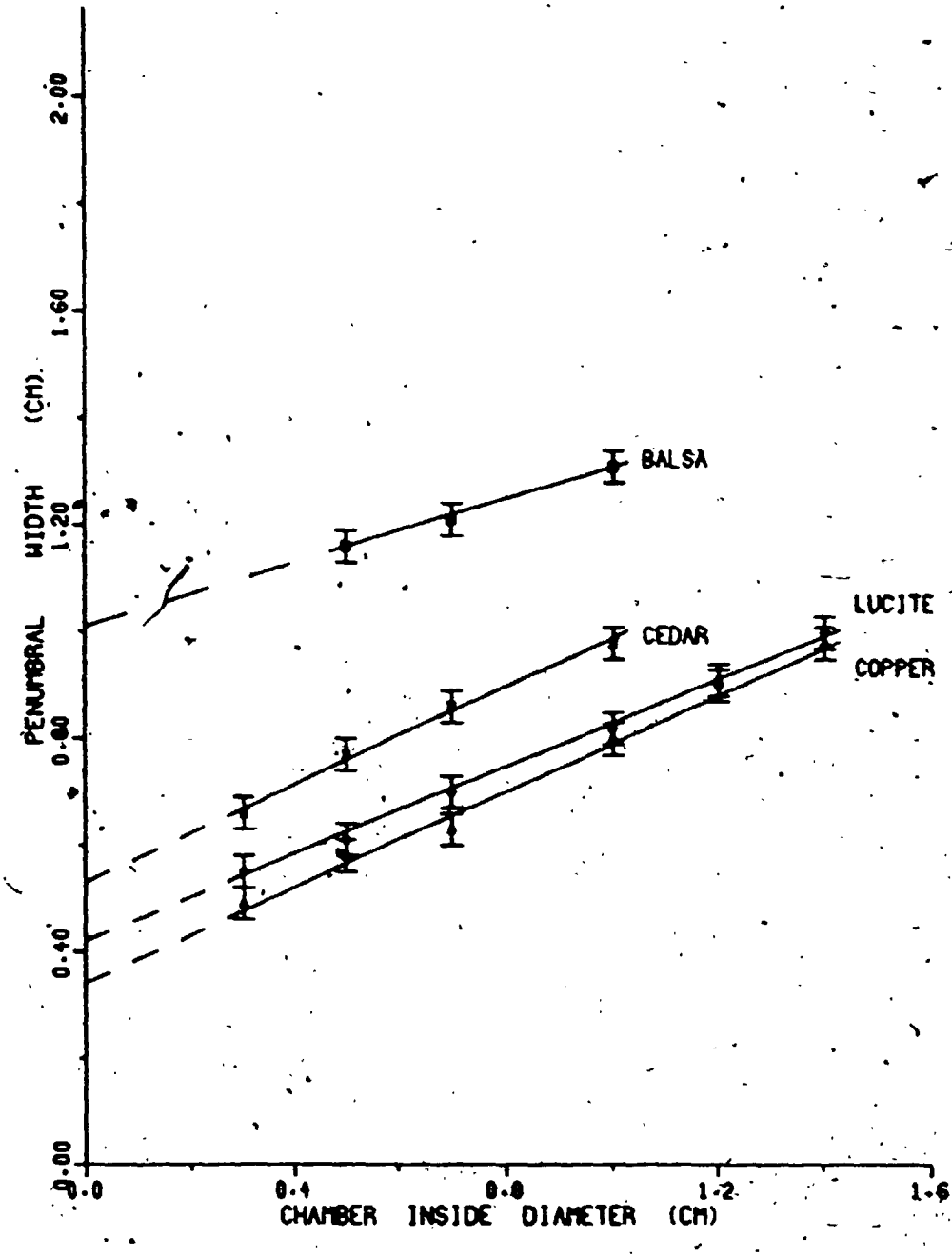

FIGURE 4.22

CO-60 BEAM P20-80 PENUMBRAL WIDTH VERSUS CHAMBER INSIDE DIAMETER FOR THE PENUMBRAL DOSE DISTRIBUTIONS IN LUCITE, CEDAR, BALSA AND COPPER.

CHAPTER V

THEORETICAL RESULTS

5.1 Introduction

The primary penumbral dose distributions can be determined theoretically as the convolution integral of two parameters, the primary penumbral photon-fluence distribution and a convolution kernel representing the dose spread function. This method has not been viable until now because the first of these parameters, the primary penumbral photon-fluence distribution has not been determined previously. The second parameter, namely the kernel, involves the physical processes involved in the dose deposition.

The physical processes that relate the penumbral photon-fluence distribution with the penumbral dose distribution measured by an ionization chamber are, (i) the photon interactions in the chamber wall which result in the production of energetic charged particles, (ii) the transport of these charged particles through the chamber wall and, (iii) the energy deposition by these charged particles in the cavity of the ionization chamber. These processes can be collectively expressed as the kernel or dose spread function.

The methodology used in the calculation of the kernel

has been described in Chapter III. The one-dimensional kernel, $K(x_i, hv, \rho_e, i.d.)$, is a function of the distance from the chamber axis along a line perpendicular to the beam direction, x_i, the photon energy, hv, the electron density of the chamber wall, ρ_e, and the inside diameter of the ionization chamber, i.d. Kernels for different beam energies are calculated for ionization chambers of different electron density and varying inside diameter.

5.2 The Kernels

The kernels, K(x), were calculated at 0.1-mm intervals across the outside diameter of the cylindrical ionization chamber. Since the kernels are symmetric about the origin, only one-half of each kernel is illustrated with identifying symbols in Figures 5.1 to 5.5.

The kernels associated with lucite-walled ionization chambers of varying inside diameter from 1 to 14 mm were calculated for Co-60, 6- and 31-MV x rays. The dependence of the kernel on the inside diameter of the ionization chamber is illustrated in Figures 5.1, 5.2 and 5.3 for Co-60, 6- and 31-MV x rays respectively. A broadening of the kernel with the chamber inside diameter is clearly indicated for all beam energies.

The lateral spread of the secondary electrons increases

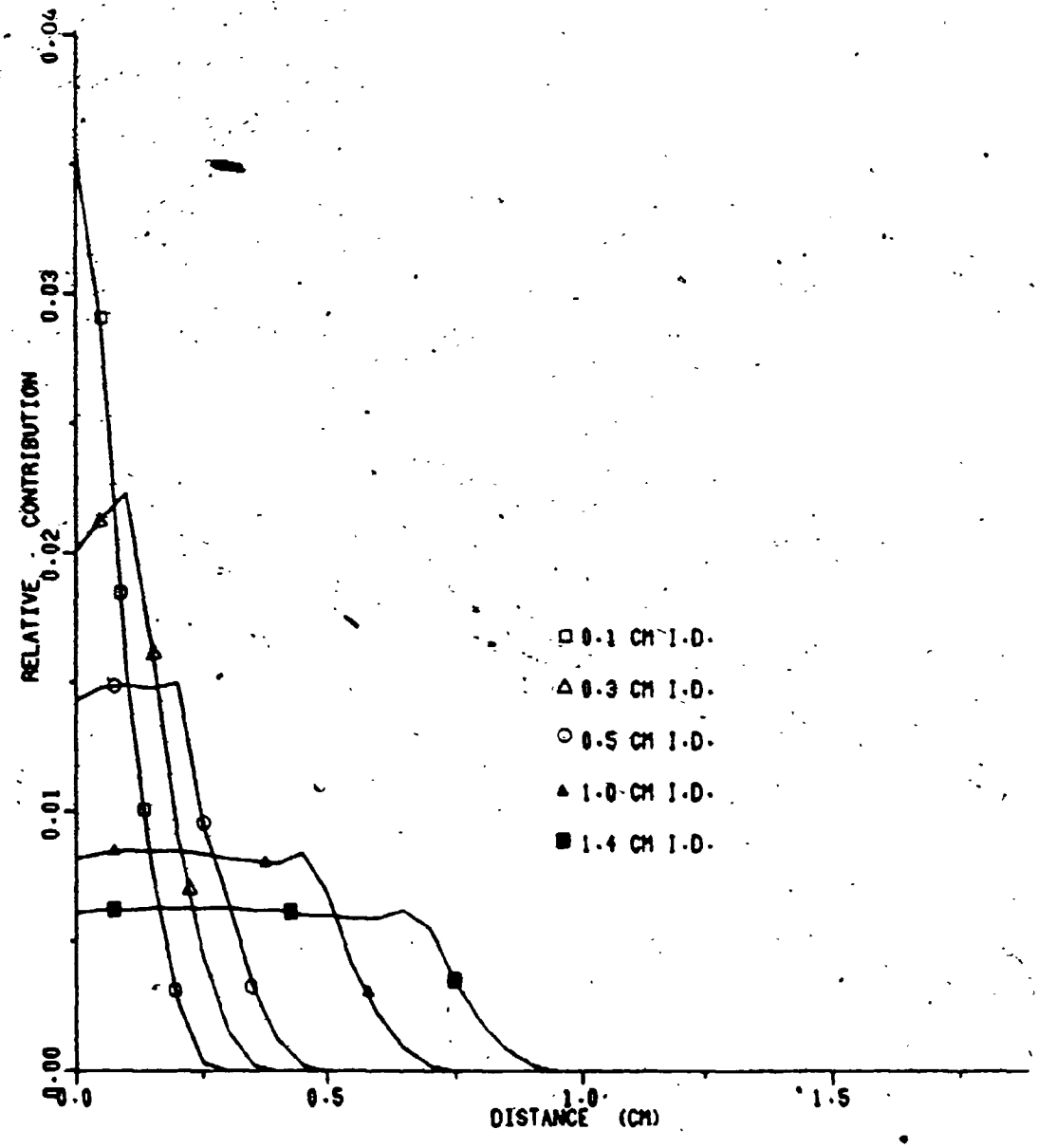

FIGURE 5.1: LUCITE KERNELS FOR VARYING INSIDE DIAMETERS FOR CO-60.

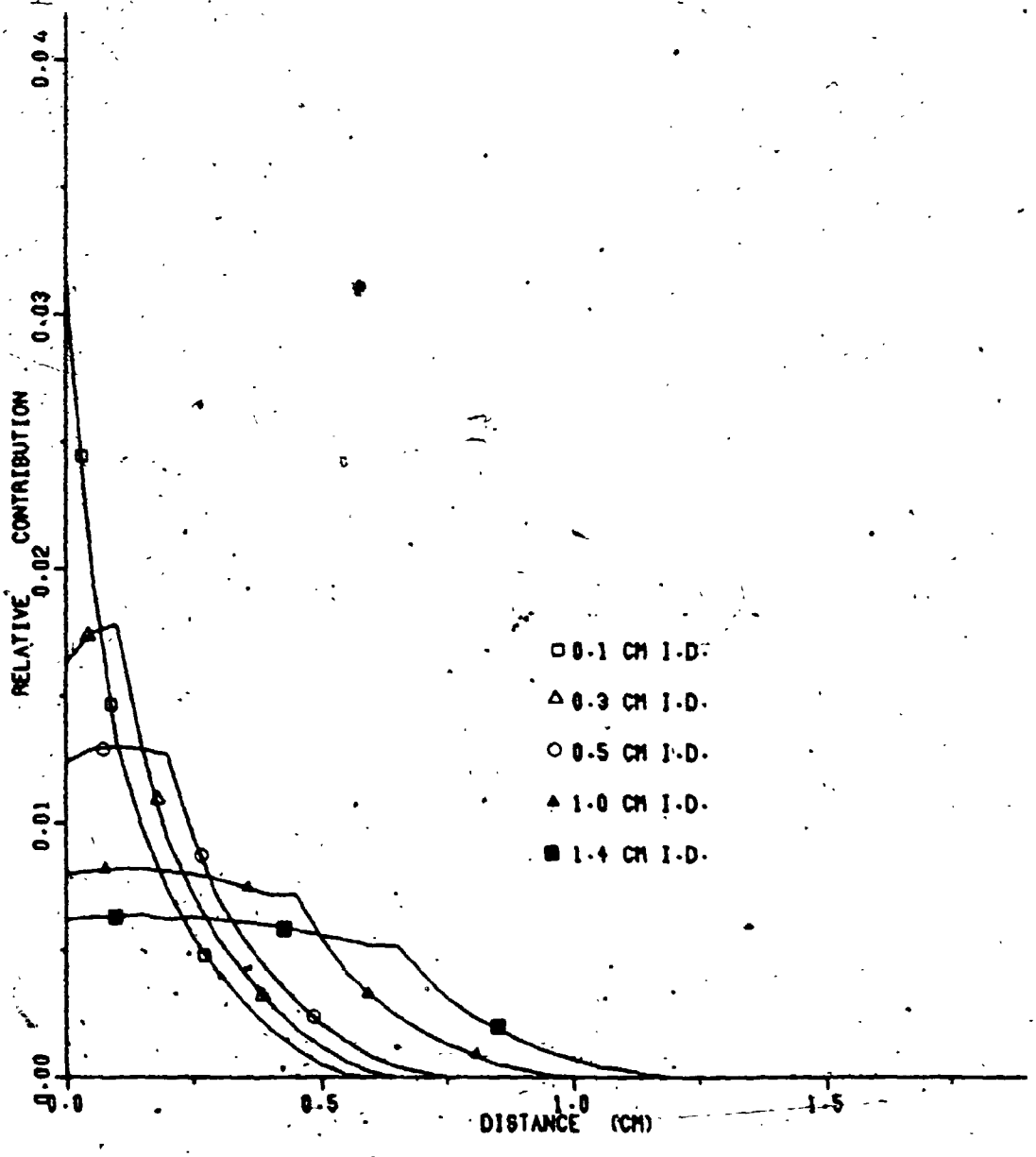

FIGURE 5.2: LUCITE KERNELS FOR VARYING INSIDE DIAMETERS FOR 6-MV X RAYS.

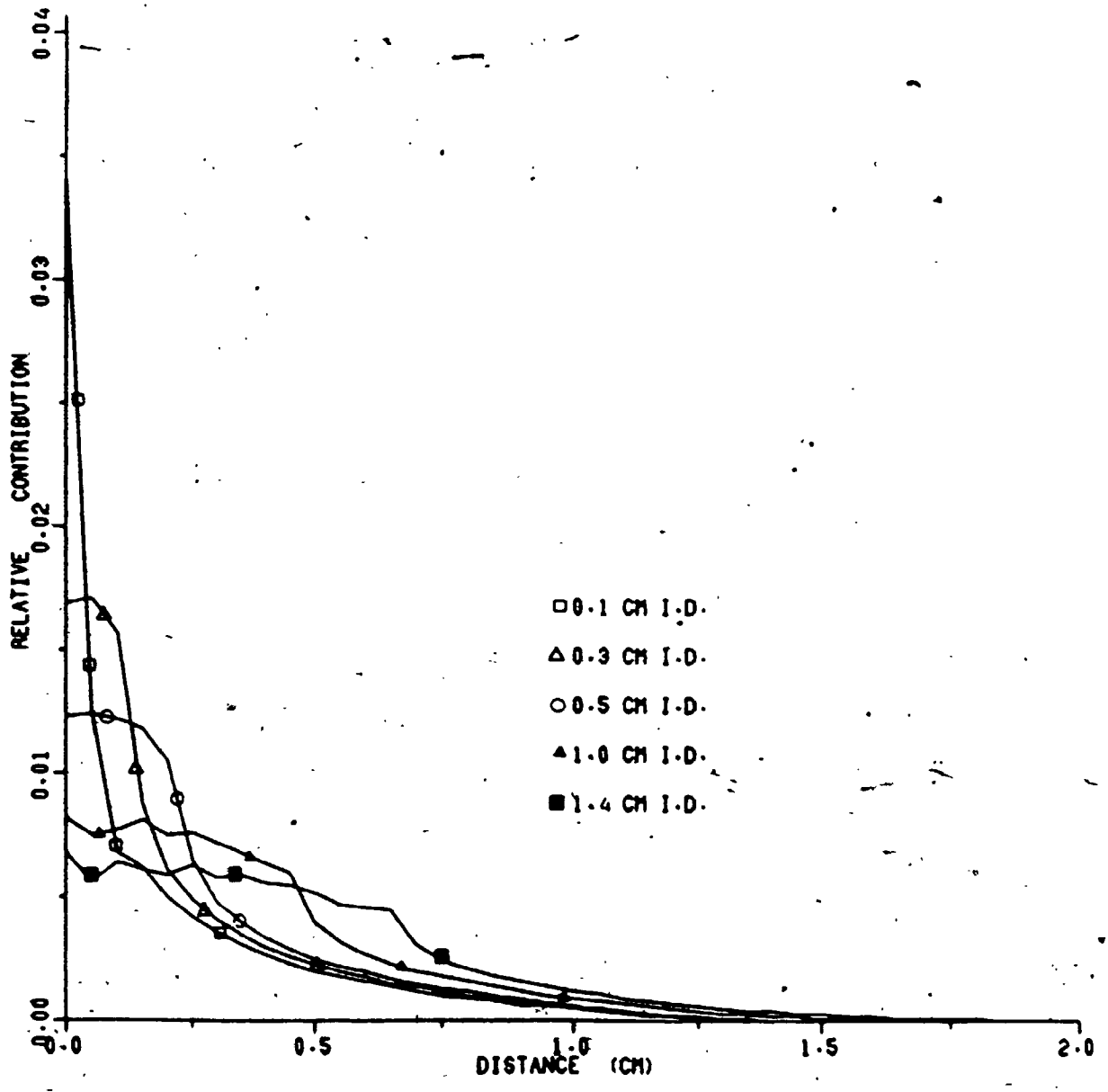

FIGURE 5.3: LUCITE KERNELS FOR VARYING INSIDE DIAMETERS FOR 31-MV X RAYS.

with the energy of the photon beam [66 72,74]. This has a direct impact on the shape of the kernel. Figure 5.4 indicates the dependence of the kernel on the beam energy for a lucite-walled ionization chamber of 0.5-cm inside diameter. Since both the electron density of the chamber wall and the inside diameter of the ionization chamber are kept constant, the variation in the shape of the kernel is directly associated with changes in the energy of the photon beam. The calculated kernels become wider and more triangular with increasing beam energy.

The dependence of the kernels on the electron density of the wall material for 6-MV x rays is indicated in Figure 5.5 for an ionization chamber of 0.5-cm inside diameter. The kernels again become wider and more triangular with decreasing electron density.

5.3 Intercomparison of Theoretical and Experimental Penumbral Widths

The dependence of the experimental P20-80 and P10-90 penumbral widths on the inside diameter of the ionization chamber were shown in Chapter IV for different photon energies and wall materials of varying electron density. In the following sections, the P20-80 and P10-90 penumbral widths, determined from theoretical penumbral dose

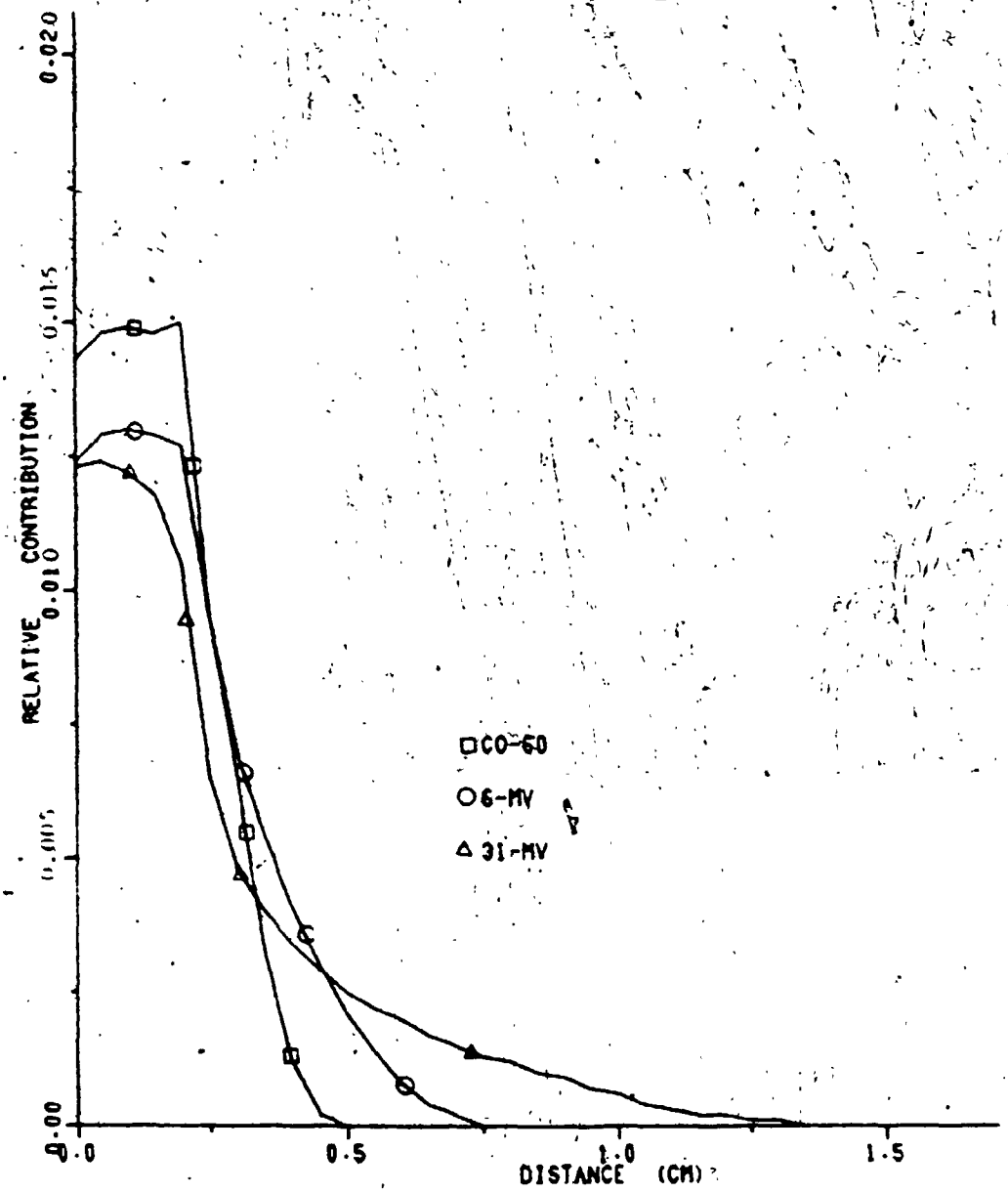

FIGURE 5.4: 0.5-CM INSIDE DIAMETER KERNELS FOR CO-60, 6- AND 31-MV X RAYS

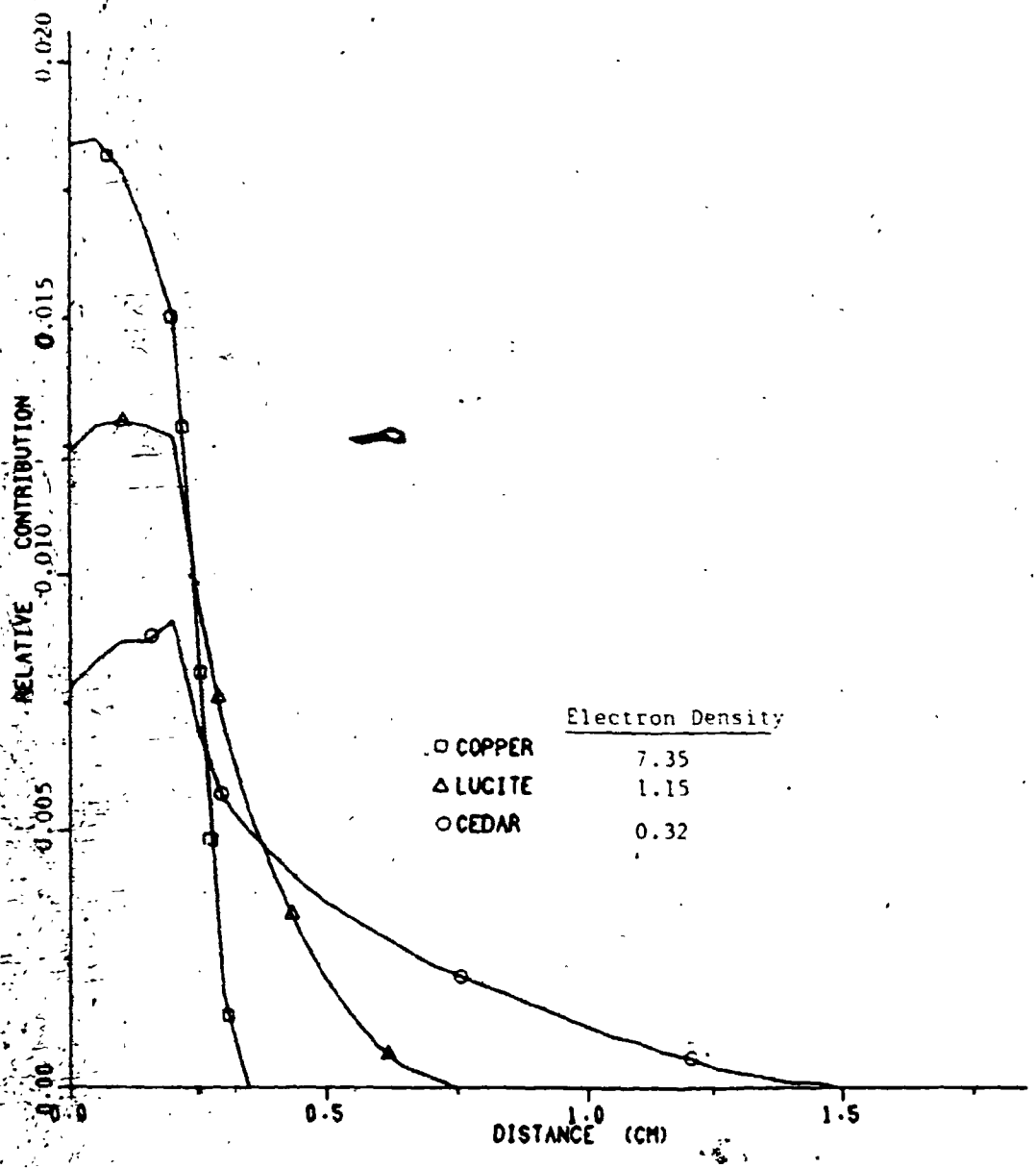

FIGURE 5.5: VARIATION WITH DENSITY OF 0.5-CM INSIDE DIAMETER KERNELS FOR 6-MV X RAYS

distributions, are compared with these experimental results.

5.3.1 Dose Distributions in Soft Tissue.

Theoretical penumbral dose distributions were calculated by the convolution method for lucite-walled ionization chambers of varying inside diameter for Co-60, 6- and 31-MV x rays. The P20-80 and P10-90 penumbral widths, determined from these distributions, are illustrated along with the experimental results in Figure 5.6 for Co-60. Both the theoretical and experimental P20-80 and P10-90 penumbral widths increase linearly with the inside diameter of the ionization chamber for inside diameters greater than 3 to 5 mm. Similar results were observed for 6- and 31-MV x rays. Although the agreement is good between the theoretical and experimental results for all beam energies, the theoretical results are consistently smaller than the corresponding experimental results.

The smallest inside diameter investigated experimentally, was limited by construction difficulties to 0.3 cm. Since any inside diameter can be studied theoretically, this method was used to study the effects of small inside diameters. The theoretical results for small inside diameters in Figure 5.6 indicate clearly that the slopes for large inside diameters decrease for small inside

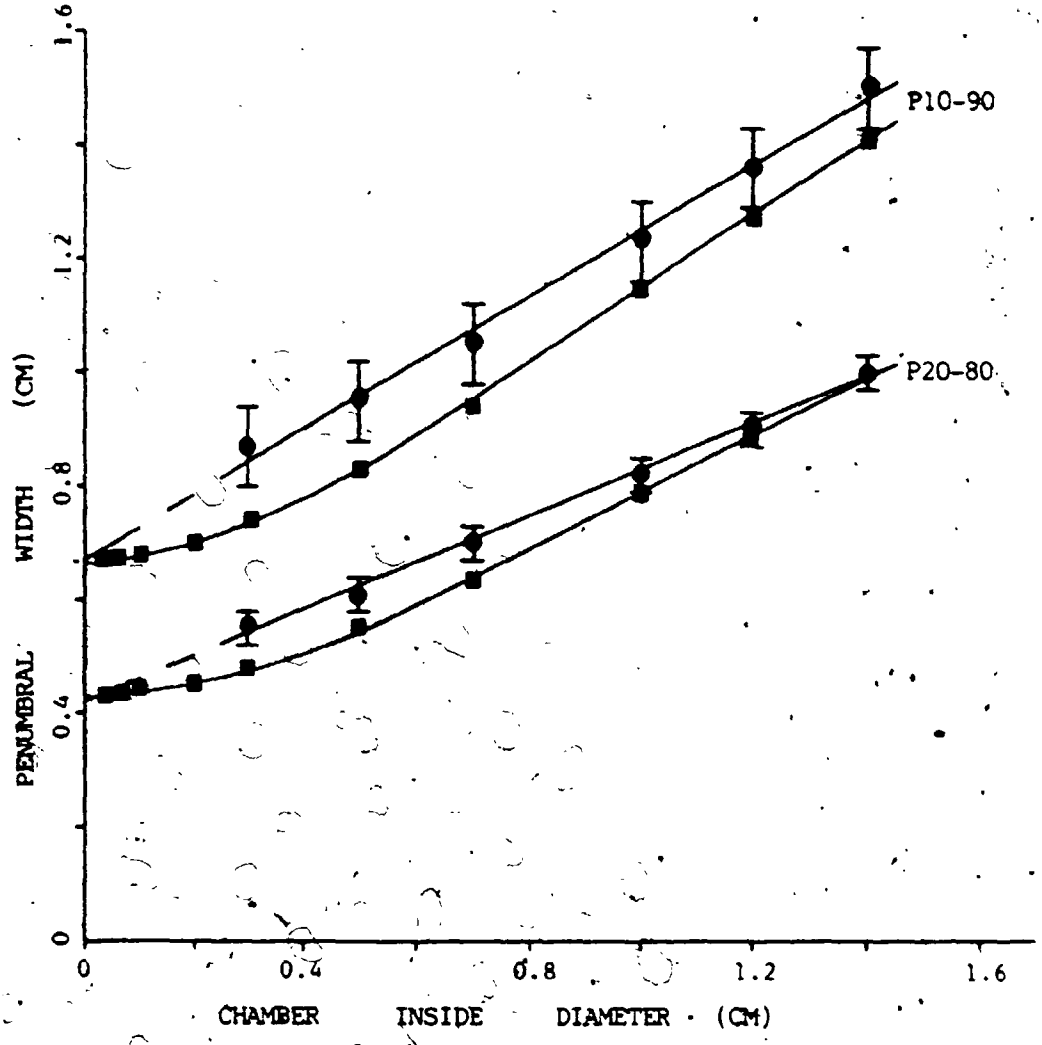

Figure 5.6 Experimental(●) and Theoretical(■) P20-80 and P10-90 Penumbral Widths versus Chamber Inside Diameter for Co-60.
Medium Lucite.

diameters and approach zero as the inside diameter approaches zero. The results for 6- and 31-MV x rays also illustrate this trend.

The P20-80 and P10-90 penumbral widths are shown as a function of inside diameter of the ionization chamber in Tables 5.1, 5.2 and 5.3 for Co-60, 6- and 31-MV x rays respectively. Both the theoretical and experimental results have been fitted with linear least squares for the larger inside diameters. The intercepts and slopes for these fits are also indicated in these tables. There are no significant differences between the experimental and theoretical slopes for either the P20-80 or the P10-90 penumbral widths.

The degradation of the measured penumbral widths, associated with the inside diameter of the ionization chamber, was eliminated by extrapolating the results linearly to zero inside diameter. The intercepts give a first approximation to the primary penumbral widths. When the theoretical results for large inside diameters are extrapolated linearly to zero inside diameter, the corresponding P20-80 and P10-90 penumbral intercepts are 0.10 and 0.15 cm less than the intercept calculated for inside diameters approaching zero. These corrections must be added to the linearly-extrapolated experimental intercepts to obtain the best estimates of the primary P20-80 and P10-90 penumbral widths.

Table 5.1

Chamber Inside Diameter (CM)	Penumbral P20-80 Width (CM)		Penumbral P10-90 Width (CM)	
	Theory	Experiment	Theory	Experiment
0.04	0.43	-	0.67	-
0.06	0.43	-	0.67	-
0.10	0.44	-	0.68	-
0.20	0.45	-	0.70	-
0.30	0.48	0.55	0.74	0.87
0.50	0 55	0.61	0.83	0.95
0.70	0.63	0.70	0.94	1 05
1.00	0.78	0.82	1.14	1.23
1.20	0.88	0.90	1.27	1.36
1.40	1.00	1.00	1.41	1.50
Intercept	0.43	0.42±0.05	0.67	0.67±.11
Slope cm/cm i.d	0 50	0.41±.05	0.65	0.58±.13

Table 5.1: The Theoretical and Experimental P20-80 and P10-90 Penumbral Widths, Intercepts and Slopes for the Penumbral Dose Distributions in Lucite for Co-60.

Table 5.2

Chamber Inside Diameter (CM)	Penumbral P20-80 Width (CM)		Penumbral P10-90 Width (CM)	
	Theory	Experiment	Theory	Experiment
0.04	0.41	-	0.68	-
0.06	0.41	-	0.68	-
0.10	0.43	-	0.69	-
0.20	0.45	-	0.73	-
0.30	0.49	0.48	0.77	0.85
0.50	0.57	0.58	0.88	0.96
0.70	0.65	0.70	0.99	1.07
1.00	0.81	0.86	1.18	1.25
1.20	0.92	0.95	1.31	1.40
1.40	1.02	1.08	1.46	1.57
Intercept	0.41	0.32±0.05	0.68	0.64±.11
Slope cm/cm i.d	0.51	0.54±.05	0.64	0.64±.13

Table 5.2: The Theoretical and Experimental P20-80 and P10-90 Penumbral Widths, Intercepts and Slopes for the Penumbral Dose Distributions in Lucite for 6-MV X Rays.

Table 5.3

Chamber Inside Diameter (CM)	Penumbral P20-80 Width (CM)		Penumbral P10-90 Width (CM)	
	Theory	Experiment	Theory	Experiment
0.04	0.55	-	1.10	-
0.06	0.55	-	1.11	-
0.10	0.57	-	1.12	-
0.20	0.60	-	1.16	-
0.30	0.64	0.64	1.20	1.44
0.50	0.71	0.72	1.28	1.50
0.70	0.79	0.85	1.36	1.59
1.00	0.91	1.00	1.50	1.73
1.20	1.01	1.07	1.61	1.84
1.40	1.10	1.19	1.72	1.96
Intercept	0.55	0.49±0.05	1.10	1.26±.11
Slope cm/cm i.d	0.43	0.50±.05	0.49	0.49±.13

Table 5.3: The Theoretical and Experimental P20-80 and P10-90 Penumbral Widths, Intercepts and Slopes for the Penumbral Dose Distributions in Lucite for 31-MV X Rays.

5.3.2 Dose Distributions in Low-Density Medium

The penumbral model emphasized that the accurate determination of the penumbral dose distribution in lung requires a Bragg-Gray ionization chamber with walls constructed of lung-equivalent media. For comparison with some of the experimentally determined distributions in media of low density, primary penumbral dose-distributions were calculated for cedar-walled ionization chambers for Co-60 and 6-MV x rays, and for balsa-walled ionization chambers for Co-60. The theoretical and experimental penumbral widths for cedar-walled ionization chambers are shown in Figure 5.7 for Co-60; the results for 6-MV x rays are similar. For large inside diameters, both the theoretical and experimental penumbral widths are observed to increase linearly with the chamber inside diameter.

The theoretical results for small inside diameters in Figure 5.7 again indicate that the dependence of the P20-80 and P10-90 penumbral widths approaches zero as the chamber inside diameter approaches zero. The differences of 0.10 and 0.15 cm between the theoretically extrapolated and calculated intercepts for the P20-80 and P10-90 penumbral widths must again be added to the experimental intercepts to obtain the best estimate of the primary penumbral widths.

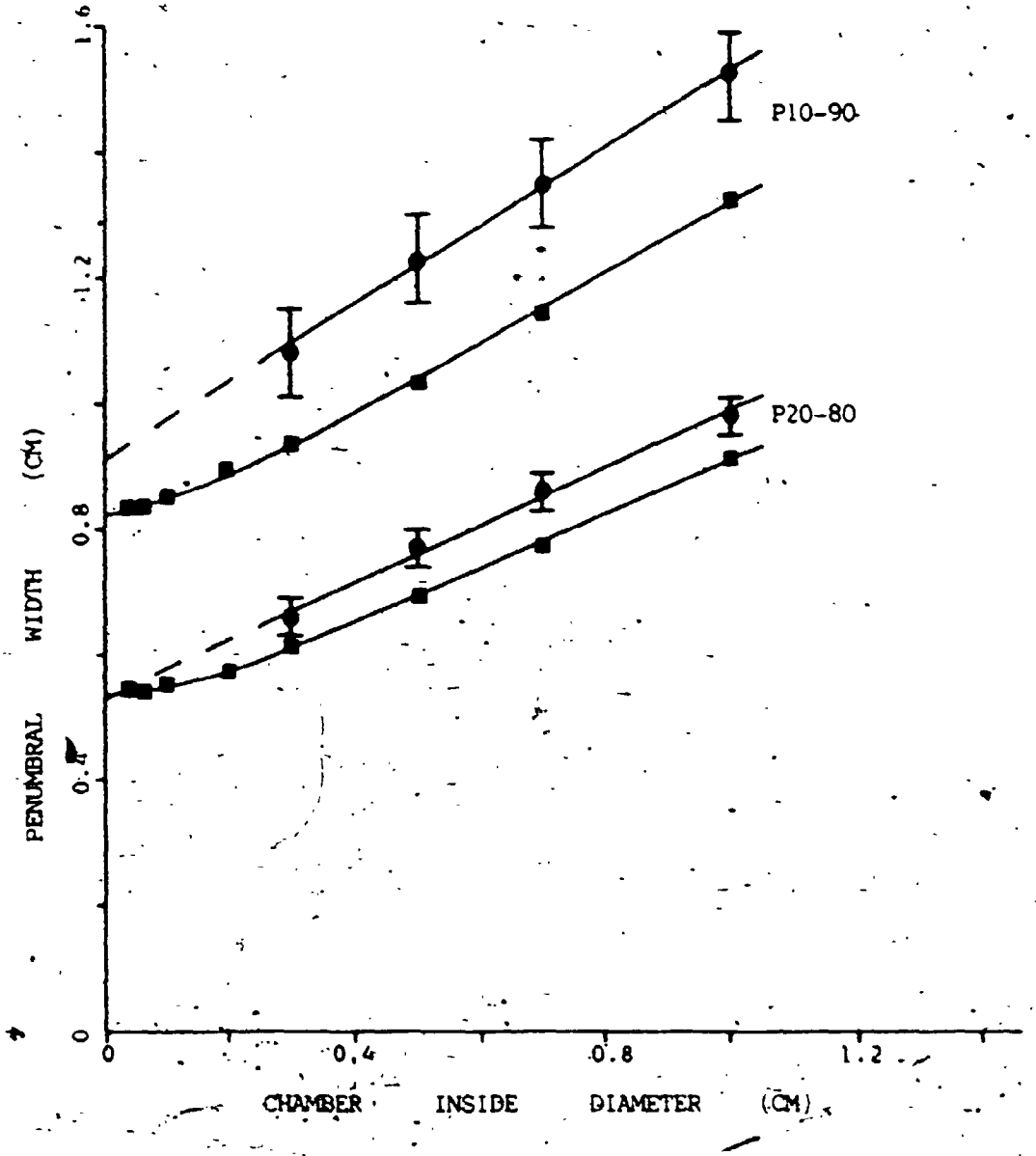

Figure 5.7 Experimental(●) and Theoretical(■) P20-80 and P10-90 Penumbral Widths versus Chamber Inside Diameter for Co-60.
Medium: Cedar.

Tables 5.4 and 5.5 compare the theoretical and experimental P20-80 and P10-90 penumbral widths for cedar-walled ionization chambers. The theoretical penumbral widths are smaller than the experimental widths in agreement with the results for lucite. The difference between the theoretical and experimental results is larger for the P10-90 penumbral widths than for the P20-80 penumbral widths.

The theoretical and experimental results for large inside diameters have been fitted with linear least squares. The intercepts and slopes associated with the dependence of these penumbral widths on the inside diameter of the ionization chamber are also indicated in Tables 5.4 and 5.5. The slope of the linear least squares fit is a measure of the degradation associated with the chamber inside diameter. The theoretical and experimental intercepts and slopes are in good agreement for both Co-60 and 6-MV x rays.

Theoretical penumbral dose distributions were also calculated for balsa-walled ionization chambers of varying inside diameter for Co-60. The theoretical P20-80 and P10-90 penumbral widths, determined for these distributions, are shown along with the experimental results in Figure 5.8. In agreement with the experimental results, the P20-80 and P10-90 penumbral widths increase

Table 5.4

Chamber Inside Diameter (CM)	Penumbral P20-80 Width (CM)		Penumbral P10-90 Width (CM)	
	Theory	Experiment	Theory	Experiment
0.04	0.54	-	0.83	-
0.06	0.54	-	0.83	-
0.10	0.55	-	0.85	-
0.20	0.57	-	0.89	-
0.30	0.61	0.66	0.93	1.08
0.50	0.69	0.77	1.03	1.23
0.70	0.77	0.86	1.14	1.35
1.00	0.91	0.98	1.32	1.52
Intercept	0.54	0.53±0.05	0.83	0.91±.11
Slope cm/cm i.d	0.43	0.46±.05	0.56	0.62±.13

Table 5.4 The Theoretical and Experimental P20-80 and P10-90 Penumbral Widths, Intercepts and Slopes for the Penumbral Dose Distributions in Cedar for Co-60.

Table 5.5

Chamber Inside Diameter (CM)	Penumbral P20-80 Width (CM)		Penumbral P10-90 Width (CM)	
	Theory	Experiment	Theory	Experiment
0.04	0.73	-	1.29	-
0.06	0.74	-	1.30	-
0.10	0.75	-	1.31	-
0.20	0.78	-	1.35	-
0.30	0.82	0.83	1.39	1.61
0.50	0.90	0.93	1.47	1.76
0.70	0.98	1.03	1.56	1.90
1.00	1.11	1.17	1.70	2.09
Intercept	0.73	0.69±0.05	1.29	1.41±.11
Slope cm/cm i.d	0.41	0.49±.05	0.46	0.68±.13

Table 5.5 The Theoretical and Experimental P20-80 and P10-90 Penumbral Widths, Intercepts and Slopes for the Penumbral Dose Distributions in Cedar for 6-MV X Rays.

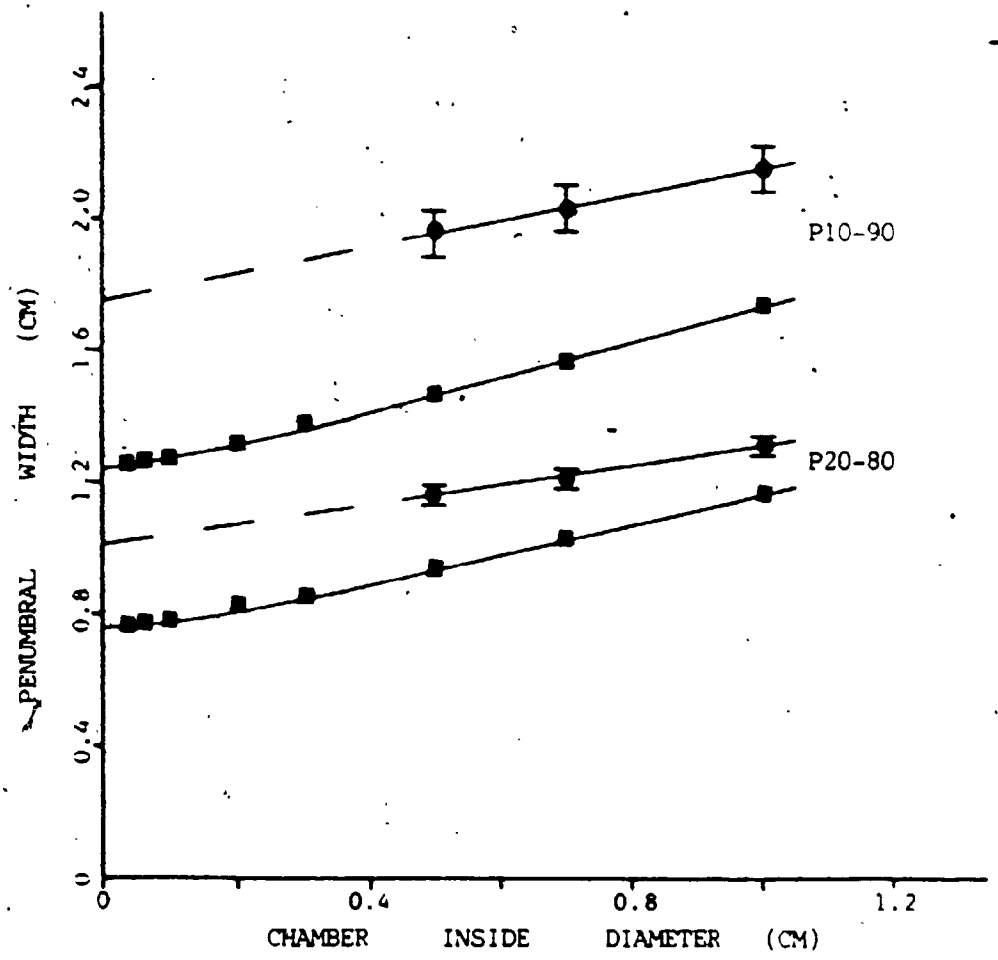

Figure 5.8 Experimental(●) and Theoretical(■) P20-80 and P10-90 Penumbral Widths versus Chamber Inside Diameter for Co-60
Medium Balsa.

linearly with the chamber inside diameter for large inside diameters. The theoretical penumbral widths are however, significantly smaller than the corresponding experimental values.

Table 5.6 compares the intercepts and slopes derived from the experimental and theoretical penumbral widths. For the balsa-walled ionization chambers, the experimental slope is significantly smaller than the corresponding theoretical slopes. In agreement with the results for lucite and cedar, the theoretical results for small inside diameter in Figure 5.8 indicate that the dependence of the P20-80 and P10-90 penumbral widths on the chamber inside diameter approaches zero as the inside diameter approaches zero. These results are discussed in Chapter VI.

5.3.3 Dose Distributions in High-Density Medium

In this project, two distributions, namely, the photon-fluence and the dose distributions, are associated with the penumbral region of high-energy radiotherapy beams. The difference between the two penumbral distributions is associated with the lateral spread of the secondary electrons. In media of high-electron density, the range and lateral spread of the electrons are reduced and the difference between the penumbral photon-fluence and

Table 5.6

Chamber Inside Diameter (CM)	Penumbral P20-80 Width (CM)		Penumbral P10-90 Width (CM)	
	Theory	Experiment	Theory	Experiment
0.04	0.73	-	1.22	-
0.06	0.75	-	1.25	-
0.10	0.78	-	1.27	-
0.20	0.82	-	1.31	-
0.30	0.85	-	1.37	-
0.50	0.93	1.16	1.46	1.95
0.70	1.03	1.21	1.56	2.03
1.00	1.16	1.31	1.73	2.15
Intercept	0.73	1.01±0.05	1.22	1.75±.11
Slope cm/cm i.d	0.46	0.30±.05	0.54	0.40±.13

Table 5.6 The Theoretical and Experimental P20-80 and P10-90 Penumbral Widths, Intercepts and Slopes for the Penumbral Dose Distributions in Balsa for Co-60.

dose distributions then decreases. The two distributions are equivalent in media of infinite electron density. In media of high electron density such as copper, the penumbral dose distribution approaches the penumbral photon-fluence distribution. The measured distribution must, however, be corrected for the inside diameter of the ionization chamber.

For each photon energy, kernels associated with copper-walled chambers of varying inside diameter were calculated and convolved with the corresponding penumbral photon-fluence distributions to obtain the penumbral dose distributions. The P20-80 and P10-90 penumbral widths, determined from these theoretical distributions, are compared with the experimental results in Figures 5.9 for Co-60. The results for 6- and 31-MV x rays are similar to those of Co-60.

In agreement with the experimental results, the theoretical P20-80 and P10-90 penumbral widths increase linearly for chambers of large inside diameter. The theoretical results again indicate that the slope of the penumbral width versus chamber inside diameter approaches zero as the chamber inside diameter approaches zero.

The experimental and theoretical P20-80 and P10-90 penumbral widths are indicated in Tables 5.7, 5.8 and 5.9

associated with the lateral spread of the secondary electrons. Figures 4.19 and 4.20 indicate that the lateral spread of the secondary electrons in soft tissue is smaller for Co-60 than for 6-MV x rays. The advantage of the small source diameter for 6-MV x rays relative to Co-60 is therefore offset by the increased lateral spread of the secondary electrons at the higher energy.

The primary penumbral dose distribution in soft tissue for 31-MV x rays is much broader than those of both Co-60 and 6-MV x rays. Figure 4.18 indicates that the primary penumbral photon-fluence distributions of the two accelerators are nearly identical. Figure 4.21 indicates that the increased broadening of the penumbral dose distribution for 31-MV x rays is associated with the increasing lateral spread of the secondary electrons with increasing beam energy.

Although the primary penumbral dose distributions for Co-60 and 6-MV x rays agree within experimental error, it must be recognized that Co-60 has a significantly larger phantom scatter contribution. This contribution results in a broader penumbral dose distribution in a patient for Co-60 than for 6-MV x rays. For radiotherapy treatments in which a sharp cutoff of the dose distribution is desired, the choice should be 6-MV x rays [35,88] if other factors are not compromised.

Table 5.7

Chamber Inside Diameter (CM)	Penumbral P20-80 Width (CM)		Penumbral P10-90 Width (CM)	
	Theory	Experiment	Theory	Experiment
0.04	0.40	-	0.63	-
0.06	0.40	-	0.63	-
0.10	0.41	-	0.63	-
0.20	0.42	-	0.65	-
0.30	0.44	0.49	0.68	0.81
0.50	0.49	0.58	0.75	0.88
0.70	0.56	0.63	0.85	1.00
1.00	0.69	0.80	1.02	1.17
1.20	0.79	0.91	1.16	1.31
1.40	0.89	0.98	1.28	1.44
Intercept	0.40	0.34±.05	0.63	0.61±.11
Slope cm/cm i.d	0.45	0.46±.05	0.60	0.59±.13

Table 5.7 The Theoretical and Experimental P20-80 and P10-90 Penumbral Widths, Intercepts and Slopes for the Penumbral Dose Distributions in Copper for Co-60.

Table 5.8

Chamber Inside Diameter (CM)	Penumbral P20-80 Width (CM)		Penumbral P10-90 Width (CM)	
	Theory	Experiment	Theory	Experiment
0.04	0.28		0.48	-
0.06	0.28	-	0.48	-
0.10	0.30	-	0.49	-
0.20	0.32	-	0.55	-
0.30	0.34	0.38	0.55	0.61
0.50	0.42	0.48	0.66	0.73
0.70	0.53	0.59	0.78	0.88
1.00	0.68	0.76	0.99	1.09
1.20	0.80	0.91	1.12	1.27
1.40	0.91	1.05	1.27	1.44
Intercept	0.15	0.18± 0.05	0.31	0.36±.11
Slope cm/cm i.d	0.54	0.61±.05	0.68	0.76±.13

Table 5.8. The Theoretical and Experimental P20-80 and P10-90 Penumbral Widths, Intercepts and Slopes for the Penumbral Dose Distributions in Copper for 6-MV X rays.

Table 5.9

Chamber Inside Diameter (CM)	Penumbral P20-80 Width (CM)		Penumbral P10-90 Width (CM)	
	Theory	Experiment	Theory	Experiment
0.04	0.33	-	0.61	-
0.06	0.33	-	0.61	-
0.10	0.33	-	0.62	-
0.20	0.35	-	0.64	-
0.30	0.38	0.35	0.68	0.62
0.50	0.45	0.46	0.76	0.75
0.70	0.54	0.58	0.86	0.89
1.00	0.69	0.78	1.04	1.11
1.20	0.79	0.89	1.17	1.25
1.40	0.89	1.04	1.32	1.39
Intercept	0.20	0.15±.05	0.40	0.40±.11
Slope cm/cm i.d	0.49	0.63±.05	0.65	0.71±.13

Table 5.9 The Theoretical and Experimental P20-80 and P10-90 Penumbral Widths, Intercepts and Slopes for the Penumbral Dose Distributions in Copper for 31-MV X rays.

for Co-60, 6- and 31-MV x rays respectively. The results for large inside diameters were fitted with linear least squares. The intercepts and slopes derived from the experimental and theoretical results are indicated in the tables. When the theoretical results for large chamber inside diameters are linearly extrapolated to zero inside diameter, the intercepts are approximately 0.15 cm less than the P20-80 and P10-90 penumbral widths calculated for small inside diameters. This correction should be added to the experimental intercepts to obtain the best estimates of the primary P20-80 and P10-90 penumbral widths.

There is good agreement between the theoretical and experimental slopes for large chamber inside diameters. While the theoretical intercepts for lucite, cedar and balsa are smaller than the corresponding experimental intercepts, the theoretical intercepts indicated in Tables 5.8 and 5.9 for 6- and 31-MV x rays respectively are larger than the corresponding experimental intercepts. The experimental and theoretical results for Co-60 are, however, in good agreement for wall materials of all electron densities. The theoretical slopes indicated in Tables 5.8 and 5.9 are consistently smaller than the experimental slopes, for Co-60 however, the two results are equal. These differences are discussed in Chapter VI.

CHAPTER VI

DISCUSSION

The penumbral model adopted in this project considers that two distributions exist in the penumbral region of high-energy radiotherapy units, namely, the photon-fluence and the dose distributions. The difference between the two distributions is associated with the lateral spread of the secondary electrons and is strongly dependent on the beam energy and the electron density.

The penumbral photon-fluence distribution is associated with the source-collimator configuration of the radiotherapy unit. The betatron with a focal spot less than 1 mm in diameter is expected to produce a beam with a sharp penumbral primary photon-fluence distribution. On the other hand, a Co-60 unit, housing a source of 15-mm diameter, is expected to produce a significantly broader penumbral primary photon-fluence distribution.

The interaction of this photon-fluence distribution with a medium results in the production of secondary electrons. The energy deposition by the secondary electrons results in a second distribution in the penumbral region, namely, the dose distribution. This distribution is of interest in radiotherapy. The finite range and lateral spread of the secondary electrons result in a dose distribution in the

penumbral region which is either broader than or equivalent to that of the corresponding photon-fluence distribution.

For photon beams produced by kilovoltage x-ray generators, the range of the secondary electrons approaches zero and the photon-fluence and dose distributions are equivalent. With increasing photon energy, however, the electron ranges become significant and the penumbral dose distribution becomes broader than the corresponding photon-fluence distribution. Although the angular distribution of secondary electrons becomes increasingly forward-peaked with increasing photon energy above 1 MeV [37, 38], the increased range of the secondary electrons has been shown to result in a further increase in the lateral spread [67, 73, 74]. The difference between the width of the penumbral photon-fluence and dose distributions is then expected to increase with energy above 1 MeV.

The photon-fluence distributions emitted by the radiotherapy units has never been detected directly. The response of photon detectors is a measure of the kerma. The measured kerma is, however, related directly to the photon fluence. For the in-air measurements employed in this project, the limited positional dependence of the photon-energy spectrum across the penumbral region results in equivalent kerma and photon-fluence distributions. For this reason, the primary penumbral photon-fluence

distribution can be measured with the use of photon detector if the effect of the detector configuration on the measured distribution is taken into account.

The correct measurement of the penumbral dose distribution requires the use of electron detectors that fulfils the Bragg-Gray conditions. The ionization chambers, employed in this project, fulfil those conditions. The penumbral dose distribution in a tissue-equivalent medium must be measured with a detector with walls of tissue-equivalent material. The configuration of this detector must also be considered. The artificial flattening of the penumbral distribution by the dimensions of the detector must be eliminated [62,63]. For ionization chambers, the measured distribution must therefore be corrected for the inside diameter of the ionization chamber.

In media of low electron density such as lung the range and lateral spread of the secondary electrons are increased [67,73,74]. For high-energy x rays, this results in a further broadening of the penumbral dose distribution with respect to the photon-fluence distribution. Ionization chambers with walls of lung-equivalent media must be used to measure this distribution correctly. Again, the measured distribution must be corrected for the inside diameter of the ionization chamber.

For wall materials of high-electron density, the range and lateral spread of the secondary electrons are decreased. The difference between the penumbral photon-fluence and dose distributions then decreases. In the limit of infinite electron density, the range of the secondary electrons is reduced to zero and the penumbral photon-fluence and dose distributions are equivalent. Thus, an electron detector with a wall material of infinite electron density can be made equivalent to a photon detector and can be used to measure the kerma distribution in the penumbral region of high-energy radiotherapy photon beams. The configuration of the photon detector must, however, be considered. For ionometric measurements, the distribution must be corrected for the inside diameter of the ionization chamber.

6.1 Penumbral Distributions in Soft Tissue

The measurement of the primary penumbral dose distribution in tissue-equivalent media requires the use of an electron detector such as an ionization chamber with tissue-equivalent walls. Since the inside diameter of the chamber cavity can result in the degradation of the measured primary penumbral dose distribution, the measured distribution must be corrected for this parameter.

This effect was determined using cylindrical ionization

chambers of varying inside diameters and walls of tissue-equivalent media. The dependence of the primary penumbral dose distributions on the chamber inside diameter is indicated in Figure 4.1 for Co-60. The increasing degradation with chamber inside diameter is indicated. Similar results were observed for 6- and 31-MV x-rays.

The dependence of the P20-80 and P10-90 penumbral widths on the chamber inside diameter are illustrated in Figures 4.2, 4.3 and 4.4 for Co-60, 6- and 31-MV x rays respectively. The slope of the linear least squares fit for the dependence of the penumbral widths on the chamber inside diameter is a measure of the degradation of the penumbral dose distribution by the chamber inside diameter. The slopes in Table 4.4 are nearly independent of beam quality. The results indicate that an average slope of 0.5 cm/cm inside diameter can be used to correct the measured P20-80 and P10-90 penumbral dose widths in soft tissue for chambers of any inside diameter.

Tables 5.1 5.2 and 5.3 indicate that the slopes of the linear least squares fits to the theoretical results for inside diameter greater than 0.3 cm agree with the experimental slopes. The theoretical degradation with the chamber inside diameter of the P20-80 and P10-90 penumbral dose widths in a tissue-equivalent medium is equal to the experimental degradation in Table 4.4. This indicates that

the approximations in the theoretical model relating to the inside diameter of the ionization chamber are appropriate.

The linear extrapolation of the experimental penumbral widths to zero inside diameter gives a first approximation to the primary penumbral dose widths. The primary penumbral dose distributions, derived from these penumbral widths in tissue-equivalent media, are illustrated in Figure 4.5 for Co-60, 6- and 31-MV x rays. The theoretical results, shown in Figure 3.6 for Co-60 indicate that the linear extrapolation of the experimental penumbral dose widths to zero inside diameter results in an underestimate of the correct penumbral dose widths. This underestimate is associated with the change in the slope of these curves for inside diameters which are small with respect to the width of the primary penumbral photon-fluence distribution. The theoretical results in Appendix C, indicate that when the kernel width is entirely in the linearly decreasing component of the penumbral photon-fluence distribution, the penumbral dose width is equivalent to the penumbral dose intercept corresponding to kernel width of zero dimensions. That is, the degradation associated with the kernel width is zero for sufficiently small kernel widths. Based on these results, the slope of the penumbral width versus chamber inside diameter is expected to change as the chamber inside diameter approaches zero. The magnitude of the underestimate, asociated with the linear extrapolation

of the experimental penumbral widths to zero inside diameter, is approxiamtely 0.15 cm for both the P20-80 and P10-90 penumbral widths for the three beam energies and must be added to the experimental intercepts to obtain the correct results.

It is interesting to compare the primary penumbral dose distributions for the three beam energies with a view toward the selection of machines for use in radiotherapy. The small effective source diameters for the accelerators in relation to that for Co-60 is expected to result in sharper penumbral distributions for the accelerators. The primary penumbral dose distributions for Co-60 and 6-MV x rays, however agree within the limits of experimental error. The equivalence of the two primary penumbral dose distributions can be explained in terms of the combination of the primary penumbral photon-fluence distributions and the lateral spread of the secondary electrons in soft tissue.

Table 4.18 indicates that the primary penumbral photon-fluence distribution for the Co-60 unit, housing a source of 15-mm diameter, is much broader than that for 6-MV x-ray unit with a focal spot less than 3 mm in diameter. The penumbral model indicates that the difference between the penumbral photon-fluence and dose distributions for a high-energy radiotherapy unit is

associated with the lateral spread of the secondary electrons. Figures 4.19 and 4.20 indicate that the lateral spread of the secondary electrons in soft tissue is smaller for Co-60 than for 6-MV x rays. The advantage of the small source diameter for 6-MV x rays relative to Co-60 is therefore offset by the increased lateral spread of the secondary electrons at the higher energy.

The primary penumbral dose distribution in soft tissue for 31-MV x rays is much broader than those of both Co-60 and 6-MV x rays. Figure 4.18 indicates that the primary penumbral photon-fluence distributions of the two accelerators are nearly identical. Figure 4.21 indicates that the increased broadening of the penumbral dose distribution for 31-MV x rays is associated with the increasing lateral spread of the secondary electrons with increasing beam energy.

Although the primary penumbral dose distributions for Co-60 and 6-MV x rays agree within experimental error, it must be recognized that Co-60 has a significantly larger phantom scatter contribution. This contribution results in a broader penumbral dose distribution in a patient for Co-60 than for 6-MV x rays. For radiotherapy treatments in which a sharp cutoff of the dose distribution is desired, the choice should be 6-MV x rays [35,88] if other factors are not compromised.

The P20-80 and P10-90 penumbral widths measured by the PTW and Farmer ionization chambers, are indicated in Figures 4.2, 4.3 and 4.4 for Co-60, 6- and 31-MV x rays respectively. The agreement of the commercial ionization chambers with the specially designed chambers of equivalent inside diameter is excellent. Table 4.5 compares the P20-80 and P10-90 intercepts with the penumbral widths measured with the Nuclear Associates diode and the two commercial ionization chambers. The penumbral widths for the ionization chambers are degraded relative to the intercepts. Although the P20-80 and P10-90 penumbral widths for the diode agree with the intercepts for Co-60, they are significantly smaller for the two accelerators. Since the shielded diode has a greater electron density than lucite, the lateral spread of the secondary electrons is reduced. This results in the decreased penumbral widths observed for the diode. It is evident from these results that shielded diodes cannot be employed for the measurement of penumbral dose distributions for high-energy x rays.

6.2 Penumbral Distributions in Low-Density Media

The treated volume of the patient in radiotherapy often includes lung. The correct determination of the penumbral dose distribution in lung requires the use of electron detectors manufactured with lung-equivalent walls. Since the dimensions of the sensitive volume of the detector can

result in the degradation of the penumbral dose distribution, the measured distribution must also be corrected for the configuration of the detector.

Low- and high-density lung were simulated with cedar and balsa respectively. The measurements with cylindrical cedar-walled ionization chambers, shown in Figure 4.7 for Co-60 indicate the increasing degradation of the primary penumbral dose distributions with chamber inside diameter. Similar results were observed for 6-MV x rays. The primary penumbral dose widths, determined from the measured distributions, increase linearly with the inside diameter of the ionization chamber in Figures 4.8 and 4.9 for Co-60 and 6-MV x rays respectively.

The dependence of the experimental primary penumbral dose widths on the chamber inside diameter is again a measure of the degradation associated with the chamber inside diameter. This slope is independent of the beam energy in Table 4.10 and is in agreement with the slopes for lucite. For large inside diameters, the theoretical and experimental slopes agree within the error limits. In the light of these results it is of interest to recall that the theoretical primary penumbral dose distribution in a medium of any electron density can be determined by convolving the primary penumbral photon-fluence distribution with a kernel associated with the lateral

spread of the secondary electrons in a medium of corresponding electron density. Similarly, the primary penumbral dose distribution that would be measured by an ionization chamber of any inside diameter can be determined by convolving the penumbral photon-fluence distribution with a kernel which accounts for both the inside diameter and the lateral electron spread. The shape of the kernel becomes more rectangular with increasing inside diameter.

Table C.1 (in Appendix C), indicates that the slopes are larger for rectangular than for triangular kernels. Therefore, the slope of the penumbral width versus chamber inside diameter is expected to increase with the chamber inside diameter. Both the experimental and theoretical results indicate similar increases in slope with increasing chamber inside diameter. On the other hand, the kernel becomes more triangular with decreasing electron density. The experimental slopes for Co-60 in Tables 5.5 for balsa is less than that for cedar in Table 5.4. It can therefore be concluded that the slope of the penumbral width versus chamber inside diameter decreases with increasing photon energy (kernel becomes more triangular) increases with chamber inside diameter (kernel becomes more rectangular), and decreases with electron density (kernel becomes more triangular). The change in slope with the various parameters are however, modest within the range of chamber inside diameters employed in this project. For

convenience, a constant correction factor for the degradation of the penumbral dose distribution by the chamber inside diameter can be applied for the range of beam energies and electron densities considered in this project.

A first approximation to the primary penumbral dose widths is obtained by linearly extrapolating the experimental penumbral dose widths to zero inside diameter to eliminate the inside diameter effect. The primary penumbral dose distributions, derived from these penumbral widths, are illustrated in Figure 4.10 for Co-60, 6- and 31-MV x rays. The broadening of the penumbral distributions with increasing energy is in agreement with the penumbral model and is associated with the significant lateral spread of the secondary electrons in these low-density media. The results clearly indicate that high-energy x rays are unsatisfactory for the treatment of lung disease.

The theoretical results in Figure 5.7 again indicate that the measured penumbral dose widths are independent of the inside diameter for sufficiently small inside diameters. Consequently, the linear extrapolation to zero inside diameter underestimates the primary penumbral dose widths. Due to the change in slope of the penumbral width versus chamber inside diameter as the inside diameter

approaches zero, the linear extrapolation of the results again underestimates the primary penumbral dose widths by 0.15 cm for all beam energies. This correction should be added to the experimental intercepts to obtain a better estimate of the primary penumbral dose distribution in lung-equivalent material.

Figures 4.19, 4.20 and 4.21 indicate that the primary penumbral dose distributions in lung are much broader than those in soft tissue and that the differences increase with beam energy. This increased broadening of the penumbral distributions is directly associated with decreasing electron density. These large differences in the primary penumbral dose distributions in soft tissue and lung are associated with electron fluence effects. Since these effects are not considered in the present dose calculation models, these models cannot be expected to assess accurately the dose in interface regions between soft tissue and lung. The region over which these effects are operative must be expected to increase with the beam energy.

6.3 Penumbral Distributions in a High-Density Medium

As the electron density of the medium increases, the lateral spread of the secondary electrons is reduced

[67,73,75]. Since the difference between the photon-fluence and dose distributions in the penumbral region is assocrated with the lateral spread of the secondary electrons, the penumbral dose distributions, measured with ionization chambers constructed with wall materials of high-electron density, approach the penumbral photon-fluence distribution. In the limit of infinite electron density, the penumbral dose and photon-fluence distributions are equivalent.

As in the case of measurements with unit-density and low-density media, the primary penumbral dose distributions, measured with copper-walled ionization chambers, are dependent on the inside diameter of the ionization chamber as illustrated in Figure 4.11 for Co-60. Similar results are also observed for 6- and 31-MV x rays. Figures 4.12, 4.13 and 4.14 indicate that the primary P20-80 and P10-90 penumbral dose widths of these distributions increase linearly with the chamber inside diameter for Co-60, 6- and 31-MV x rays respectively. The slopes of these linear least squares fit in Table 4.14, are approximately independent of beam energy. Although these slopes are not significantly different from those determined for unit-density and low-density media, the copper results indicate a different trend. The 31-MV x rays experimental P20-80 and P10-90 slopes for copper in Table 4.14 are larger than for lucite in Table 4.4. The

increase in slope with electron density can be explained in terms of the kernels. The kernels are expected to be more rectangular for copper than for lucite due to the reduced lateral electron spread in copper. The results in Table C.1 (Appendix C) indicate that the slopes are larger for rectangular than for triangular kernels. The experimental results are in agreement with this expectation. Since the slopes are nearly independent of both the beam energy and the electron density, an average slope of 0.5 cm/cm inside diameter can, for convenience, be used to correct the P20-80 and P10-90 penumbral dose widths measured in any medium for any beam energy, for chamber inside diameter effect.

For inside diameters larger than 0.3 cm the theoretical penumbral dose widths also increased linearly with the inside diameter. The theoretical slopes in Tables 5.7, 5.8 and 5.9 for Co-60, 6- and 31-MV x rays respectively are approximately equal to the experimental slopes. This agreement was observed earlier with ionization chambers of both tissue-equivalent and lung-equivalent media and has been discussed previously.

The extrapolation of the linear least squares fits to zero chamber inside diameter eliminates the inside diameter effect and gives a first approximation to the primary penumbral dose widths. The primary penumbral dose

distribution, derived from these penumbral widths in copper, is illustrated in Figure 4.11 for Co-60. It is observed that the primary penumbral dose distributions in copper for the accelerators are equivalent but significantly broader than that for Co-60.

The theoretical results, shown in Figure 5.9 for Co-60 indicate that linear extrapolation of the results to zero inside diameter results in an underestimate of the correct primary penumbral dose widths. This underestimate is again associated with the change in slope for inside diameters which are small with respect to the penumbral widths of the photon-fluence distributions. The results for 6- and 31-MV x rays indicate similar trends. In agreement with the results for media of low-electron density, the underestimate of the P20-80 and P10-90 penumbral widths is approximately 0.15 cm for the three beam energies.

The theoretical results in Appendix C indicate that when the kernel width is entirely in the linearly decreasing component of the penumbral photon-fluence distribution, the penumbral dose width is equivalent to the penumbral dose intercept corresponding to kernel width of zero dimensions. Moreover, the penumbral dose intercept corresponding to kernel width of zero dimensions, is equivalent to the penumbral photon-fluence width. These results are relevant to the design of ideal photon

detectors. It will be recalled the kernel accounts for both the chamber inside diameter and the lateral spread of the secondary electrons. The kernel width approaches zero only when both the chamber inside diameter and the lateral spread approach zero. In a sufficiently high-density medium, the lateral spread of the secondary electrons approaches zero. Therefore, the kernel associated with an ionization chamber of sufficiently small inside diameter and wall of high electron density, is of sufficiently narrow width that the photon-fluence distribution is undegraded by the kernel width. Such an ionization chamber approaches an ideal photon detector.

The extrapolated primary penumbral dose distributions in copper are very similar for 6- and 31-MV x rays. This result is significant when considered in relation to the penumbral model. For media of low-electron density, the primary penumbral dose distributions for 31-MV x rays were significantly broader than the corresponding distributions for Co-60 and 6-MV x rays. This is expected on the basis of the increased lateral electron spread for 31-MV x rays. For medium of high-electron density such as copper, the lateral electron spreads are reduced for all energy. The primary penumbral dose distrbutions in copper are consequently approaching the primary penumbral photon-fluence distributions. The agreement between the 6- and 31-MV x-ray distributions is then associated with the

near equality of the effective source diameters for these units. The broader primary penumbral dose distribution for Co-60 is expected on the basis of the 15-mm source diameter.

6 4 The Primary Penumbral Photon-Fluence Distribution

The penumbra model considers that two distributions exist in the penumbral region of high-energy x-ray beams namely the photon-fluence and dose distributions. The difference between the distributions is associated with the lateral spread of the secondary electrons. In medium of infinite electron density, the lateral spread of the secondary electrons is reduced to zero and the two distributions are equivalent.

The penumbral photon-fluence distribution has not been previously measured. In this project, extrapolation techniques to zero chamber inside diameter and to infinite electron density have been introduced to make this measurement possible. The former extrapolation has been considered theoretically in Chapter V. The latter extrapolation, however, involves the correlation of measurements involving media of varying electron density and atomic number and requires some explanation.

Kornelsen [66] has indicated that the lateral spread of the secondary electrons in media of the same atomic number can be scaled as the reciprocal of their respective electron densities. Since the atomic numbers of lucite, cedar and balsa are approximately equal, the scaling of these media should not represent a significant approximation. For copper, however, the atomic number is significantly higher. This impacts significantly on the mass angular scattering power with the result that the scaling is not expected to be exact. Since this has not been investigated experimentally and theoretical approaches involves numerous assumptions, [66], the results for copper have also been scaled inversely with the electron density. This scaling results in the incorrect placement of the copper results on the abscissa in Figures 4.15, 4.16 and 4.17. The lateral shift, however, is expected to be small and is not likely to seriously affect the slopes of the curves in these figures.

The P20-80 and P10-90 primary penumbral dose widths for Co-60, 6- and 31-MV x rays are plotted against the reciprocal of the relative electron density in Figures 4.15, 4.16 and 4.17 respectively. The slope of the linear least squares fit for the dependence of the primary penumbral widths on the reciprocal of the relative electron density is a measure of the lateral spread of the secondary electrons. The slopes, listed in Table 4.18, increase

significantly with the photon beam energy. This demonstrates clearly that the lateral spread of the secondary electrons increases with beam energy. The linear extrapolation of the results to infinite electron density gives a first approximation to the primary penumbral photon-fluence widths. Similar extrapolations for a number of penumbral widths were used to determine the penumbral primary photon-fluence distributions indicated in Figure 4.18 for Co-60, 6- and 31-MV x rays. The primary penumbral photon-fluence distributions for 6- and 31-MV x rays are in close agreement while that for Co-60 is significantly broader.

The Co-60 source has a diameter of 15 mm while the source diameters for 6- and 31-MV x rays are less than 3 and 1 mm respectively. The broader photon-fluence distribution for Co-60 is clearly associated with the larger source diameter. Since the source diameter is less for 31- than for 6-MV x rays, the photon-fluence distribution is expected to be sharper. Table 4.18 does, in fact, indicate that the P20-80 penumbral width is less for 31- than for 6-MV x rays. The P10-90 penumbral widths are however, equivalent for the two accelerators. The increased broadening of the P10-90 penumbral widths for 31-MV x rays is associated with the increase in the effective source diameter relating to the use of larger beam flattener.

Since the primary dose widths were underestimated by the linear extrapolation to zero inside diameter, the resulting photon-fluence widths are similarly underestimated. Consequently, the P20-80 and P10-90 penumbral widths for the primary penumbral photon-fluence distributions are underestimated by about 0.15 cm. Therefore the photon-fluence distributions employed in the calculation of the theoretical results are too sharp. The underestimates for other photon-fluence penumbral widths should be determined and added to the experimental photon-fluence widths in order to obtain a better estimate of the primary penumbral photon-fluence distributions.

6.5 Comparison between Theory and Experiment

The theoretical study in this project was designed to validate the penumbral model, to confirm the experimental results and to extend the experimental results into areas which cannot be readily investigated. The theoretical results involved the development of kernels to describe the lateral spread of the secondary electrons for media of varying electron density and the convolution of these kernels with the experimental penumbral photon-fluence distribution. The experimental results were obtained from detailed ionometric measurements of the primary penumbral dose distributions in media of varying electron density for

three photon energies. Both the theoretical and experimental results have been conveniently described by employing the slope and intercept of the linear least squares fit for the dependence of the penumbral widths on the chamber inside diameter. These parameters along with the small inside diameter effects are now considered.

6.5.1 The Slope

Although the slopes can be approximated by a single correction factor of 0.5 cm/(cm inside diameter) for both the P20-80 and P10-90 penumbral widths, it is interesting to study the trends of the slopes in more detail. The slopes, determined for the idealized photon-fluence distributions and kernels, are useful in this regard. These results indicate that the P10-90 slopes are from 0.1 to 0.2 cm/(cm inside diameter) greater than the P20-80 slopes. Both the experimental and theoretical slopes in Tables 5.1 to 5.9 similarly indicate larger slopes for the P10-90 penumbral withds.

The idealized results also indicate that the slopes for rectangular kernels are from 0.15 to 0.20 cm/(cm inside diameter) greater than for triangular kernels. With increasing inside diameter, the kernels become more rectangular and the slopes are expected to increase.

Although the experimental results have been fitted linearly, Figures 4.2, 4.3 and 4.4 indicate that the slopes could be fitted with a curve of increasing slope with increasing inside diameter. With increasing photon beam energy, the kernels become more triangular. Since the primary penumbral photon-fluence distributions are in agreement for 6- and 31-MV x rays, these beams can be compared in this regard. There is some experimental and theoretical evidence in Tables 5.1 to 5.9 of a decreased slope for the more triangular kernel for 31-MV x rays. The kernels are also expected to become more triangular with decreasing electron density of the medium with a resultant decrease in slope. In agreement with this expectation, the experimental and theoretical results for Co-60 do indicate smaller slopes for balsa than for lucite. Similarly, the experimental and theoretical slopes for 31-MV x rays are smaller for lucite than for copper.

The idealized distributions also indicate that the slopes decrease as the width of the photon-fluence distribution increases. The photon-fluence distribution for Co-60 is broader than those for the two accelerators. Hence, some decrease in slope can be expected for Co-60. Both the experimental and theoretical results in Chapter V indicate smaller slopes for Co-60 than for 6-MV x rays. Both the experimental and theoretical results have indicated some dependence of the slope of the penumbral

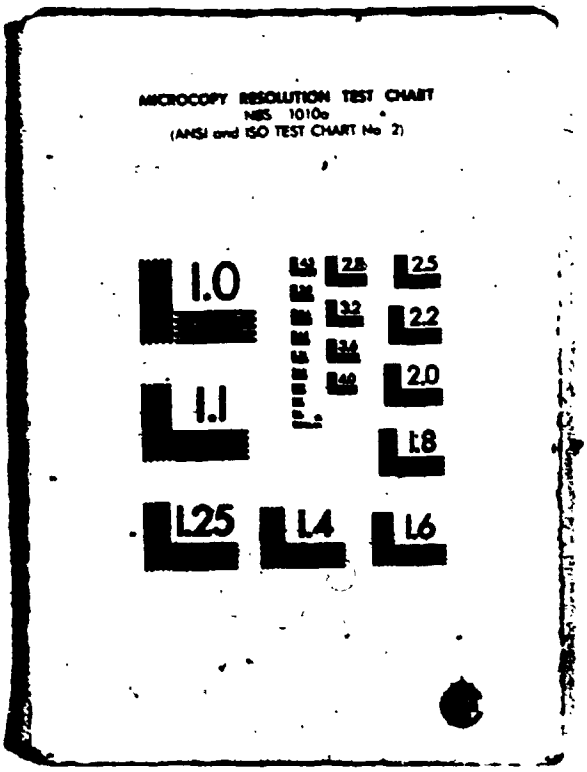
MICROCOPY RESOLUTION TEST CHART
NBS 1010a
(ANSI and ISO TEST CHART No. 2)
1.0
1.1
1.25
1.4
1.6
2.0
2.2
2.5

width versus chamber inside diameter on both the beam energy and electron density of the chamber wall. This slope, however, is not a strong function of these parameters. Therefore, for convenience, a single correction factor of 0.5 cm/cm inside diameter can be used for both the P20-80 and P10-90 penumbral widths for all energies and electron densities considered in this project.

6.5.2 The Intercept

As a result of the decreased slope for ionization chambers of small inside diameter, the linear extrapolation to zero inside diameter of the experimental results leads to an underestimate of the correct penumbral width by about 0.1 to 0.15 cm. The theoretical intercepts, however, are similarly underestimated because the primary penumbral photon-fluence distributions, employed in the calculations, were based on penumbral widths which were similary extrapolated to zero inside diameter. The direct comparison of the theoretical and experimental intercepts, therefore has some validity.

For chamber walls with atomic numbers close to that of air (lucite, cedar and balsa), the agreement between the theoretical and experimental intercepts is satisfactory. There is evidence of the agreement getting worse with balsa

but this must be expected as a result of the large increase in the lateral spread of the secondary electrons for the low-electron density. For copper, the agreement between the theoretical and experimental intercepts is weakest. This lack of agreement for copper is associated with two factors. First, the effect of the atomic number on the scaling of the electron ranges and lateral spreads was ignored in the calculations. Second, the high atomic number of copper results in significant pair production interactions. The short range contribution of these pair production interactions for copper were neglected in the calculations. This effectively results in a broadening of the kernel which would result in the larger theoretical penumbral widths observed.

6.5.3 Small Inside-Diameter Effect

Since it was not practical to use chambers of inside diameter smaller than 0.3 cm, the linear least squares fits of the penumbral widths against the chamber inside diameter were linearly extrapolated to zero inside diameter to eliminate the effect of the chamber diameter. The theoretical results indicate that the degradation associated with the chamber inside diameter approaches zero as the chamber inside diameter approaches zero. This has already been explained in section 6.1. A linear

extrapolation to zero inside diameter, therefore, results in an underestimation of the primary penumbral dose widths. Since the slope of 0.5 cm/cm inside diameter is nearly independent of both the beam energy and the electron density of the medium, the experimental P20-80 and P10-90 primary penumbral dose widths are underestimated by no more than 0.15 cm. The linear extrapolation to zero inside diameter of the theoretical results for large inside diameters similarly resulted in an underestimate of 0.1 to 0.15 cm.

6.5.4 Differences between Theory and Experiment

The differences between theory and experiment are largely associated with the limitations of the theoretical model. The kernels, employed in the penumbral dose calculations, were obtained by assuming both that all photons interact by the Compton process and that the electrons travel straight paths from the point of origin to the chamber cavity. These assumptions, which were made to reduce the complexity of the kernel calculations, are not valid for high-energy x-ray beams and hence the theoretical results are less accurate.

Since the pair production particles are emitted at small angles to the direction of the photons, exclusion of pair

production process eliminates some contributions from regions close to the chamber cavity. This has the greatest impact on the 20 to 80% dose region of the penumbral dose distribution and is likely responsible for the poor agreement between theory and experiment for the P20-80 penumbral dose widths in copper. Similarly, the exclusion of pair production in the calculation of the kernels will result in overestimation of the kernel widths for copper. This is expected to get worse with increase in beam energy. Triangular kernels will result in a smaller slope for the penumbral width versus chamber inside diameter. The 31-MV x rays theoretical slopes for copper in Table 5.9 are smaller than the experimental slopes. Therefore, in order to improve the accuracy of the results for copper, pair production interactions must be included in the calculation of the kernels, especially for photon energies above 6-MV x rays.

The multiple scattering of the secondary electrons results in a Gaussian distribution in their lateral coordinates as they propagate through matter. This was not taken into account in our theoretical model. This underestimation of the lateral spread of the secondary electrons resulted in an underestimate in the kernel width (especially in low-density media). The poor agreement between theory and experiment in the P10-90 penumbral width is associated with the exclusion of the Gaussian spread of

the secondary electrons from the theoretical model.

Effective photon energies were used in the theoretical calculations. Although Co-60 is a homogeneous beam, the photon beams from the accelerators are heterogeneous. The choice of a single energy has some impact on the shape of the kernel and could contribute in part to the differences between theory and experiment.

CHAPTER VII

CONCLUSIONS

A model was considered in this project [32] which indicates that there are two distributions in the penumbral region of high-energy radiotherapy beams, namely, the photon-fluence and the dose distributions. The difference between the two distributions is associated with the lateral spread of the secondary electrons and increases with both increasing beam energy and decreasing electron density. The penumbral photon-fluence distribution is associated with the source/collimator configuration of the radiotherapy unit while the penumbral dose distribution is of interest in radiotherapy.

The measurement of these two distributions requires detectors of different types. The cavity theory relating to this model indicates that electron detectors are required to measure the penumbral dose distribution while photon detectors are required to measure the penumbral kerma distribution. For measurements in air, the limited positional dependence of the photon energy spectra across the penumbral region of high-energy radiotherapy beams results in equivalent primary penumbral kerma and photon-fluence distributions.

This project has also extended the experimental use of ionization chambers. The effect of both the configuration and type of the dosemeter on the measurement of penumbral distributions has been indicated and new extrapolation techniques have been introduced to measure improved primary penumbral dose distributions for Co-60, 6- and 31-MV x rays.

The effect of the configuration of the detector on the primary penumbral dose distribution was studied in detail using cylindrical lucite-walled chambers with inside diameters from 0.3 to 1.4 cm. The penumbral widths, determined from these distributions, increased linearly with the inside diameter of the ionization chamber and were extrapolated to zero inside diameter to eliminate this effect. The intercepts of the primary penumbral dose widths for the three beam energies were employed to determine a first approximation to the primary penumbral dose distributions. The degradation of the primary penumbral dose widths, associated with the inside diameter of the ionization chamber, was nearly independent of the beam energy.

This ionometric technique was extended to the determination of the primary penumbral dose distributions in non tissue-equivalent media including both lung-equivalent media and a high-density medium. The degradation of the penumbral dose distributions increased

with decreasing electron density of the medium and with increasing beam energy.

The experimental determination of the primary penumbral dose widths for copper-walled ionization chambers clearly indicated a decreasing range and lateral spread of the secondary electrons. This indicates the importance of detector type, that is the atomic number and electron density of the detector, on the measurement of the penumbral dose distributions. This effect was clearly indicated by the narrow penumbral widths measured with the diode detector. It was indicated that diode detectors cannot be used to measure the penumbral dose distributions for high-energy x rays.

In a medium of infinite electron density, the range and lateral spread of the secondary electrons is reduced to zero. In this case, the penumbral kerma and dose distributions are equivalent. The primary penumbral dose widths for media of varying electron density were plotted as a function of the reciprocal of the relative electron density to make the extrapolation to infinite electron density practical. This method was employed to determine the equivalent primary penumbral kerma and photon-fluence distributions for the three beam energies.

Convolution techniques were employed to study the primary penumbral dose distributions for Co-60, 6- and 31-MV x rays in media of varying electron density including lucite, cedar, balsa and copper. Kernels were calculated for chambers of varying inside diameter and wall materials of varying electron density. The primary penumbral dose distributions, obtained by convolving these kernels with the experimental primary penumbral photon-fluence distributions, compared favourably with the experimental primary penumbral dose distributions. The degradation associated with the inside diameter of the ionization chamber agreed with the experimental results. The theoretical determination of the dependence of the primary penumbral dose width on the inside diameter of the ionization chamber indicated that the slope decreases for ionization chambers of small inside diameter. This effect results in a 0.10 to 0.15 cm underestimate in the extrapolated primary penumbral P20-80 and P10-90 dose widths. The primary penumbral photon-fluence widths, based on a similar linear extrapolation to zero inside diameter, were also underestimated by a corresponding amount. Idealized photon-fluence distributions and kernels were employed to illustrate the effects of the shape of the kernel on the calculated distributions.

Although there is satisfactory agreement between theory and experiment, there are some important areas that need to be developed further to improve the accuracy of the model. The discrepancy between theory and experiment stems from the approximations introduced in the theoretical model. A more accurate model requires an improved treatment of the photon energy spectra of the accelerators, involving both pair production process and multiple scattering of the secondary electrons. The experimental techniques, developed in this work in combination with a new penumbral model, has led to an improved assessment and understanding of the penumbral regions for high-energy radiotherapy units.

APPENDIX A

Kernel Calculation for Offset Disc.

The second stage in the calculation of the kernel associated with the central disc, as indicated in Chapter III, involves the calculation of the relative dose contributions from interaction voxels in the offset discs, to the air cavity of the central disc. This calculation requires the determination of three parameters: (i) the pathlength of an electron from the point of origin to the edge of the air cavity, S, (ii) the pathlength of the electron through the air cavity of the central disc, Δl and (iii) the solid angle subtended at the interaction voxel by the appropriate area element of the air cavity of the central disc, $\Delta\Omega$. The path of the electron can be illustrated by considering orthogonal projections of the cylindrical ionization chamber.

Figures A.1 and A.2 illustrate the projections onto the y-z and x-y planes respectively and can be used to calculate the pathlength from the interaction voxel $A(x_i, y_i, z_i)$ to the edge of the cavity, S, the pathlength of the electron through the air cavity of the central disc, Δl, and the solid angle subtended at the interaction voxel, $\Delta\Omega$.

We consider, as a first step, the angle subtended at the

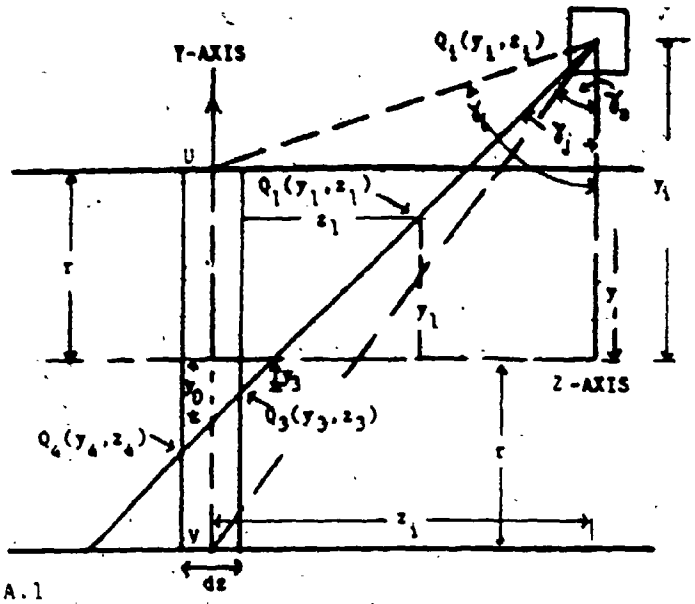

FIGURE A.1
THE Y-Z PROJECTION.

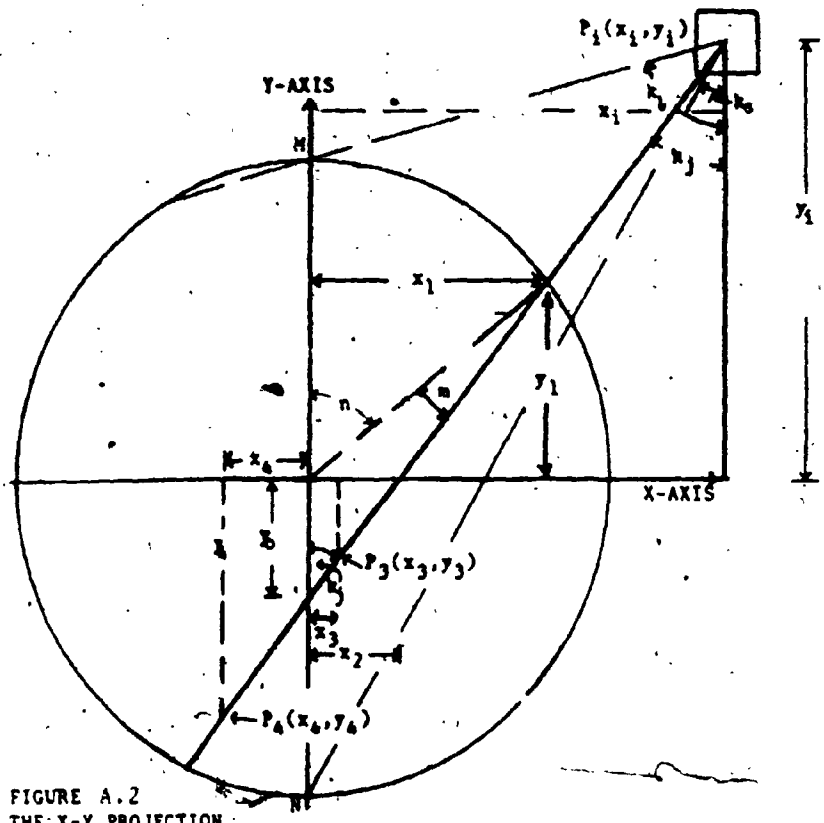

FIGURE A.2
THE X-Y PROJECTION.

ORTHOGONAL PROJECTIONS OF THE CYLINDRICAL IONIZATION CHAMBER.

interaction voxel $A(x_i, y_i, z_i)$ by a narrow strip of the air cavity of the central along the y-axis. Let the path of an electron originating from the interaction voxel intersect the y-axis at $(x=0, y=y_0, z=0)$. The Compton scattering angle for this electron, θ_j, is given by:

$$\tan^2(\theta_j) = (x_i^2 + z_i^2)/(y_i - y_o)^2 \qquad (A.1)$$

This scattering angle, θ_j (in 3-Dimension), becomes γ_j and k_j when projected onto the y-z and x-y planes, as indicated in Figures A.1 and A.2 respectively. The projected angles, γ_j and k_j are given by the following equations:

$$\tan^2(\gamma_j) = z_i^2/(y_i - y_o)^2$$

$$= [z_i^2/(x_i^2 + z_i^2)] \tan^2(\theta_j) \qquad (A.2)$$

and

$$\tan^2(k_j) = x_i^2/(y_i - y_o)^2$$

$$= [x_i^2/(x_i^2 + z_i^2)] \tan^2(\theta_j) \qquad (A.3)$$

Therefore,

$$\tan^2(\theta_j) = \tan^2(\gamma_j) + \tan^2(k_j) \qquad (A.4)$$

In order to calculate S and Δl, we need to calculate the following:

(i) the point of entry of the electron to the air cavity, $Q_1(x_1, y_1, z_1)$

(ii) the point of entry of the electron into the air cavity of the central disc, $Q_3(x_3, y_3, z_3)$; and

(iii) the point of exit of the electron from the air cavity of the central disc, $Q_4(x_4, y_4, z_4)$

In the y-z projection illustrated in Figure A.1, the point of origin of the electron becomes $Q_i(y_i, z_i)$ and the electrons travelling between the angles γ_s and γ_l are considered in the calculations and are given by the following equations:

$$\tan(\gamma_s) = z_i/(y_i + r)$$

Therefore, $$\gamma_s = \tan^{-1}[z_i/(y_i + r)] \qquad (A.5)$$

Similarly, $$\gamma_l = \tan^{-1}[z_i/(y_i - r)] \qquad (A.6)$$

The angle $(\gamma_l - \gamma_s)$ is divided into 15 equal angles, $\Delta\gamma[=(\gamma_l - \gamma_s)/15]$. The pathlengths to the edge of the air cavity, S_j, and through the air cavity of the central disc, Δl_j, are calculated for electrons scattered at mean (projected) angles, γ_j (i.e. between $\gamma_j - \Delta\gamma/2$ and $\gamma_j + \Delta\gamma/2$, with γ_j varying between γ_s and γ_l in increments of $\Delta\gamma$ such that

$$\gamma_j = \gamma_s + (2j-1)\Delta\gamma/2; \quad j=1,..,15 \qquad (A.7)$$
$$[\gamma_1 = \gamma_s + \Delta\gamma/2; \quad \gamma_{15} = \gamma_l - \Delta\gamma/2]$$

The points Q_1, Q_3 and Q_4 are determined for each of the 15 electron paths. One such electron path (projected unto the y-z and x-y planes) is illustrated in Figures A.1 and A.2. The approach used in the determination of Q_1, Q_3 and Q_4 are described below.

Let the thickness of the disc, Δz, be equal to 2t. Then, If $\tan(\gamma_j) < (z_i + t)/(y_i + r)$. $y_4 = -r$. Otherwise,

$$\tan(\gamma_j) = (z_i + t)/(y_i - y_4)$$

Therefore, $$y_4 = y_i - (z_i + t)\cot(\gamma_j) \quad (A.8)$$

and $$z_4 = -t$$

Also, $$\cot(\gamma_j) = (y_i - y_o)/z_i$$

Therefore, $$y_o = y_i - z_i\cot(\gamma_j) \quad (A.9)$$

$$\tan(\gamma_j) = (z_i - t)/(y_i - y_3)$$

Therefore, $$y_3 = y_i - (z_i - t)\cot(\gamma_j) \quad (A.10)$$

and $$\tan(\gamma_j) = (z_i - z_3)/(y_i - y_3)$$

Therefore, $$z_3 = z_i - (y_i - y_3)\tan(\gamma_j) \quad (A.11)$$

From Figure A.2, using similar triangles,

$$y_o/y_i = -x_2/(x_i - x_2)$$

Therefore, $$x_2 = -y_o * x_i/(y_i - y_o) \quad (A.12)$$

$$y_o/y_3 = x_2/(x_2 - x_3)$$

Therefore, $$x_3 = -x_2(y_3 - y_o)/y_o \quad (A.13)$$

$$y_4/y_o = (x_2 - x_4)/x_2$$

Therefore, $$x_4 = x_2(y_o - y_4)/y_o \quad (A.14)$$

Also from Figure A.2,

$$\tan(k_j) = |x_2|/|y_o|$$

Hence, $$k_j = \tan^{-1}(|x_2|/|y_o|) \quad (A.15)$$

Similarly, using sine rule,

$$\sin(k_j)/r = \sin(m)/|y_o|$$

Hence,

$$m = \sin^{-1}[\,|y_o| * \sin(k_j)/r\,] \quad (A.16)$$

When the x-coordinate of the point of intersection of the

projected electron path (in the x-y plane) with the x-axis, x_2, is greater than zero ($x_2 > 0$) as illustrated in Figure A.2,

$$n = k_j + m \qquad (A.17)$$

However, when x_2 is less than zero ($x_2 < 0$), which is the case when $\tan(k_j) > (x_i/y_i)$

$$n = k_j - m \qquad (A.18)$$

And when $x_2 = 0$, $m = 0$ and $n = k_j$

From Figure A.2,

$$x_1 = r\sin(n) \qquad (A.19)$$

and

$$y_1 = r\cos(n) \qquad (A.20)$$

From Figure A.1,

$$\tan(\gamma_j) = (z_i - z_1)/(y_i - y_1)$$

Therefore,

$$z_1 = z_i - (y_i - y_1)\tan(\gamma_j) \qquad (A.21)$$

Using the above equations, the coordinates $Q_1(x_1,y_1,z_1)$, $Q_3(x_3,y_3,z_3)$ and $Q_4(x_4,y_4,z_4)$ are determined. Then, the pathlength from the interaction voxel, $A(x_i,y_i,z_i)$, to the edge of the air cavity, S_j, is calculated using the following equation:

$$S_j^2 = (x_i - x_1)^2 + (y_i - y_1)^2 + (z_i - z_1)^2 \qquad (A.22)$$

The pathlength of the electron through the air cavity of the central disc, Δl_j, is given by:

$$\Delta l_j^2 = (x_3 - x_4)^2 + (y_3 - y_4)^2 + (z_3 - z_4)^2 \qquad (A.23)$$

In order to calculate the relative number of ionizations produced in the air cavity of the central disc, due to electrons scattered between the angles $(\theta_j - \Delta\theta/2)$ and $(\theta_j + \Delta\theta/2)$, we need to calculate the element of solid angle, $\Delta\Omega_j$, subtended at the interaction voxel. To do this, we need to calculate the element of area normal to the direction of the electrons.

Figure A.4 illustrates the cross-section of the air cavity in the x-y plane. This cross section is divided into strips parallel to the x-axis. One such strip, shown shaded in Figure A.4, is for electrons scattered between the projected angles $(\gamma_j - \Delta\gamma/2)$ and $(\gamma_j + \Delta\gamma/2)$ in Figure A.3. The chord length perpendicular to the y-axis at the point of intersection of the electron path with the y-axis $(x=0, y=y_o)$, AB, is given by:

$$AB^2 = 4(r^2 - y_o^2) \qquad (A.24)$$

where y_o is given by Eqn. (A.9). The component of AB normal to the direction of the electrons in the x-y plane is $ABcos(k_j)$. Also from Eqn. (A.9),

$$CD = |z_i * [cotan(\gamma_j - \Delta\gamma/2) - cotan(\gamma_j + \Delta\gamma/2)]| \qquad (A.25)$$

and the component of CD normal to the direction of the electrons (in the y-z plane) is $CDsin(\gamma_j)$. Therefore, the component of the area EFGH normal to the direction of the electrons (in 3-Dimensions) is $ABcos(k_j) * CDsin(\gamma_j)$.

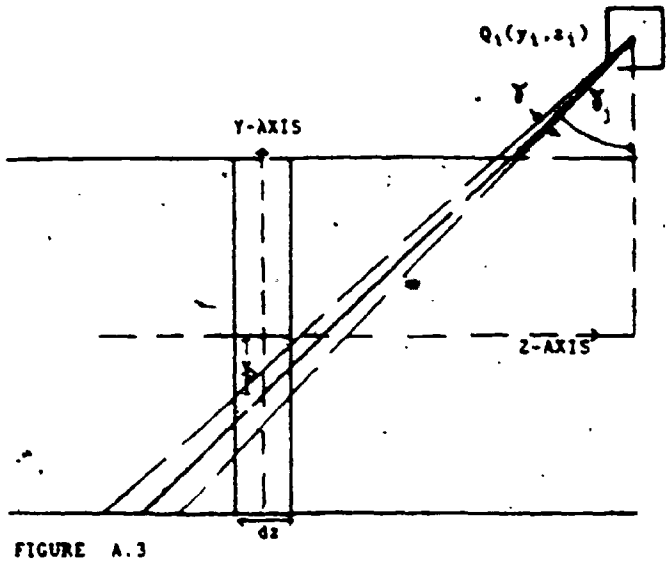

FIGURE A.3
THE Y-Z PROJECTION.

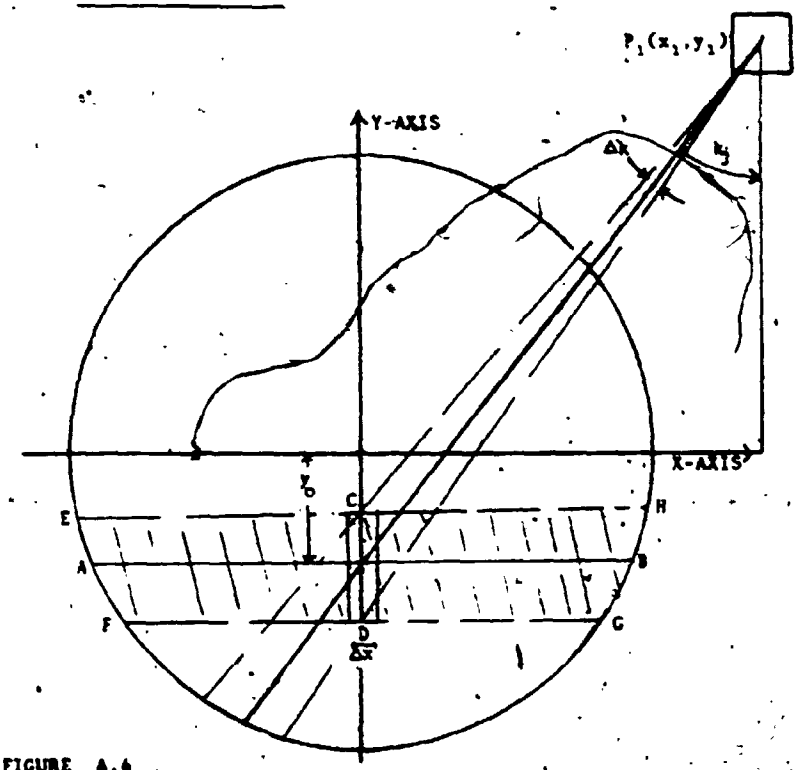

FIGURE A.4
THE X-Y PROJECTION.

We consider next the solid angle subtended at the interaction voxel by the area element, ΔA ($=CD\Delta x$), shown shaded in Figure A.4. The component of this area normal to the direction of the electrons scattered at mean angle θ_j is $\Delta A\cos(k_j)\sin(\gamma_j) = CD*\Delta x*\cos(k_j)\sin(\gamma_j)$. The pathlength of the electron from the interaction voxel to the point of intersection with the y-axis $(0, y=y_o, 0)$ is given by:

$$R_j^2 = x_i^2 + (y_i - y_o)^2 + z_i^2 \qquad (A.26)$$

Therefore, the element of solid angle subtended at the interaction voxel by the element of area ΔA, $\Delta\Omega$, is given by:

$$\Delta\Omega = CD*\Delta x*\sin(\gamma_j)\cos(k_j)/R_j^2 \qquad (A.27)$$

Therefore, the solid angle subtended at the interaction voxel by the area EFGH ($=AB.CD$ with component $AB*CD*\sin(\gamma_j)\cos(k_j)$ normal to the direction of the elctrons), $\Delta\Omega_j$, is approximately equal to $AB*\Delta\Omega/\Delta x$.

The relative number of ionizations produced in the air cavity of the central disc, due to electrons originating from the interaction voxel $A(x_i, y_i, z_i)$, that are scattered between the angles $(\theta_j - \Delta\theta/2)$ and $(\theta_j + \Delta\theta/2)$, is given by:

$$\Delta N_{i,j} = \frac{d\sigma(\theta_j)}{d\Omega'} \cdot \Delta\ell_j . \Delta\Omega_j \qquad (A.28)$$

where $d\sigma/d\Omega'$ is the Klein-Nishina differential collision cross section [See Eqn.(3.8) in Chapter III], and θ_j, the Compton scattering angle, is given by Eqn.(A.4).

The relative number of ionizations (per unit photon fluence) produced in the air cavity of the central disc, due to the electrons originating from the interaction voxel $A(x_i,y_i,z_i)$, that are scattered between the angles θ_s and θ_l, and having sufficient energy to reach the edge of the air cavity, ΔN_i, is given by:

$$\Delta N_i = \sum_{j=1}^{j=15} \frac{d\sigma(\theta_j)}{d\Omega} \cdot \Delta\mathcal{L}_j \cdot \Delta\Omega_j \qquad (A.29)$$

where

$$\tan^2(\theta_s) = \tan^2(\gamma_s) + \tan^2(k_s) = (x_i^2 + z_i^2)/(y_i + r)^2 \qquad (A.30)$$

and

$$\tan^2(\theta_l) = \tan^2(\gamma_l) + \tan^2(k_l) = (x_i^2 + z_i^2)/(y_i - r)^2 \qquad (A.31)$$

The relative number of ionizations, ΔN_i, is associated with the location of the interaction voxel, (x_i,y_i,z_i).

The z-coordinates of the interaction voxels of each disc are the same. If, for example, the calculations are for interaction voxels of the third offset disc, the z-coordinate, z_i, of each voxel is given by:

$$z_i = 3*dz = 3*2L_{max}/11 \qquad (A.32)$$

(See Eqn.(3.5) in Chapter III.)

The repetition of these calculations for each interaction voxel of the offset disc, results in a two-dimensional array of relative dose contributions to the air cavity of the central disc associated with photon interactions in that offset disc.

APPENDIX B

Interaction of X rays with Matter

Only the Compton interaction was considered in the kernel calculations. First however, it is relevant to describe briefly the important interaction processes.

A photon can interact with matter by any one of several competing mechanisms. The probability for each of these competing independent processes can be expressed as a collision cross section. The sum of these cross sections is then the probability that the incident photon will interact while passing through a square centimeter of area normal to the path of the incident photon.

In the energy range from Co-60 to 31-MV x rays, photoelectric process constitutes less than 1% of the photon interactions in chamber wall materials considered in this project [37,38,62]. Consequently, only the Compton effect and pair production need be considered. The relative importance of these processes depends on both the atomic number of the absorber and the photon energy [37,38,62].

The particles in pair production (electrons and positrons) are emitted increasingly in the forward

direction as the energy of the photon increases. At high energies, this angle is of the order of $0.511/E_\gamma$ radian where E_γ is the photon energy in MeV. For example, at a photon energy of 2.6 MeV, the mean angle at which the positron and electron are emitted is within 15 degrees from the direction of motion of the photon [79]. There is no more precise relationship between the angles and the energies of the particles since in pair production the nucleus carries away a variable amount of the momentum which is dependent on the point at which the pair was produced [79].

Since the pair particles are emitted at small angles to the direction of the incident photon, the impact of the pair production process on the lateral spread of the secondary electrons is limited to interactions occurring at small angles to the chamber cavity. The zone of contribution is limited to the region above the chamber cavity and of width slightly greater than the lateral dimension of the chamber cavity. This can be referred to as the short-range contribution. The proportion of the total chamber response that comes from regions above and close to the cavity will increase with the increase in the pair production process. The short-range contribution therefore increases with the beam energy and the atomic number of the medium of interaction. To reduce the complexity of determing the kernel, as stated earlier, only

the Compton process was considered in this project. The impact on the theoretical results of omitting the pair process from the theoretical model is however considered in the thesis.

The Compton electrons are emitted at wider angles and consequently have more impact on the broadening of the primary penumbral dose distribution. The incident photon, indicated in Figure B.1 has an energy $h\nu_o$ and a momentum $p=h\nu_o/c$. The interaction is with a single individual atomic electron in a given collision. Conservation of momentum and energy lead to the Compton equations, and the cross sections of the interactions are given by the Dirac electron theory as first applied to the Compton collision by Klein and Nishina [37,38].

The Compton electron recoils at an angle θ with kinetic energy T. A Compton scattered photon, emitted at an angle w, receives the remaining energy, $h\nu' = h\nu_o - T$. The energy of a photon is $E=h\nu$, where ν is the frequency and $h=4.135 \times 10^{-21}$ MeV.sec is Planck's constant. The rest mass energy of an electron is $m_o c^2 = 0.511$ MeV.

If the incident energy is written in terms of the dimensionless quantity,

$$\alpha = \frac{h\nu_o}{m_o c^2} \qquad (B.1)$$

then the angle θ and the kinetic energy T of the Compton recoil electron are related to the photon scattering angle, w, by:

$$\cot\theta = (1+\alpha)\tan(w/2) \qquad (B.2)$$

$$T(\theta) = h\nu_o \frac{2x\cos^2\theta}{(1+\alpha) - \alpha^2\cos^2\theta} \qquad (B.3)$$

The number of photons that are scattered in a particular direction, as a function of the number of incident photons, is $d({}_e\sigma)$ and has the dimensions:

$$d({}_e\sigma) = \frac{\text{number scattered [number/(sec.electrons)]}}{\text{number incident [number/(cm.sec)]}}$$

$$= \frac{\text{cm}}{\text{electron}} \qquad (B.4)$$

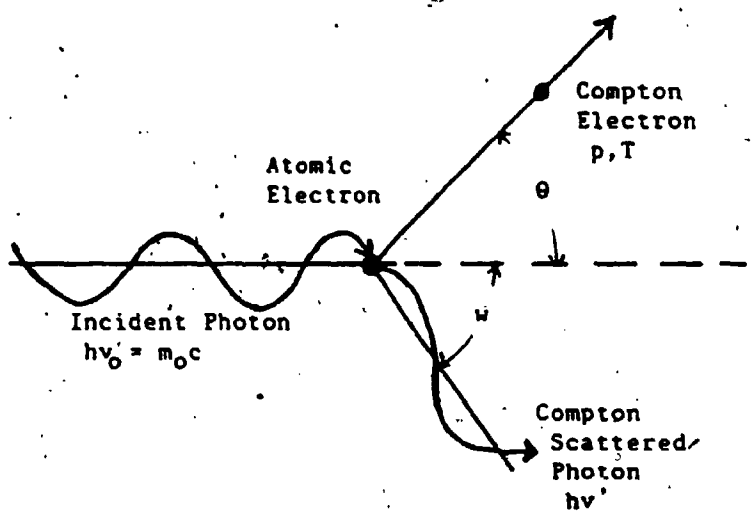

Figure B.1: The Compton Interaction Process

The probability of electrons being scattered into the solid angle $d\Omega'$ steradians at mean angle θ is given by the Klein-Nishina collision differential cross section formula:

$$\frac{d(_e\sigma)}{d\Omega'} = \left\{\frac{r_0^2}{(1+\alpha)}\right\}(1+\cos w)\left\{\frac{1}{1+\alpha(1-\cos w)}\right\}^2\left\{\frac{1+\cos^2 w}{2}\right\}$$

$$\times\left\{1+\frac{\alpha^2(1-\cos w)^2}{(1+\cos^2 w)[1+\alpha(1-\cos w)]}\right\}\left\{\frac{\sin w}{\sin^3\theta}\right\} \qquad (B.5)$$

where r_0 is the classical radius of the electron:

$$r_0 = \frac{e^2}{m_0 c^2} = 2.818 \times 10^{-13} \text{ cm} \qquad (B.6)$$

In the calculation of the kernels described in Chapter III, Equations (B.3). and (B.5) were employed respectively, in the calculation of the energy distribution, $E(\theta)$, and the angular distribution, $d\sigma(\theta)/d\Omega'$, of the Compton electrons.

APPENDIX C

Theoretical Study of the Penumbral Model

The theoretical penumbral dose distribution involves two parameters, namely the penumbral photon-fluence distribution and the convolution kernel. The photon-fluence distribution for photon beams of varying energy is determined using the experimental techniques introduced in this project while the kernel was calculated. The calculated penumbral dose distributions, which are a convolution of the photon-fluence distribution and the kernel, indicate a significant dependence on the shape of both the photon-fluence distribution and the kernel. Idealized photon-fluence distributions and kernels are used to illustrate the impact of the shape of these parameters on the calculated dose distributions.

The penumbral region of the photon-fluence distribution is simulated with a linear decrease in photon fluence from the 100% to 0% across a width w which was varied to represent photon-fluence distributions from different therapy units. These idealized distributions, illustrated in Figure C.1, have P20-80 and P10-90 penumbral photon-fluence widths of 0.6w and 0.8w respectively.

The shape of the one-dimensional calculated kernel depends on both the photon beam energy and the electron

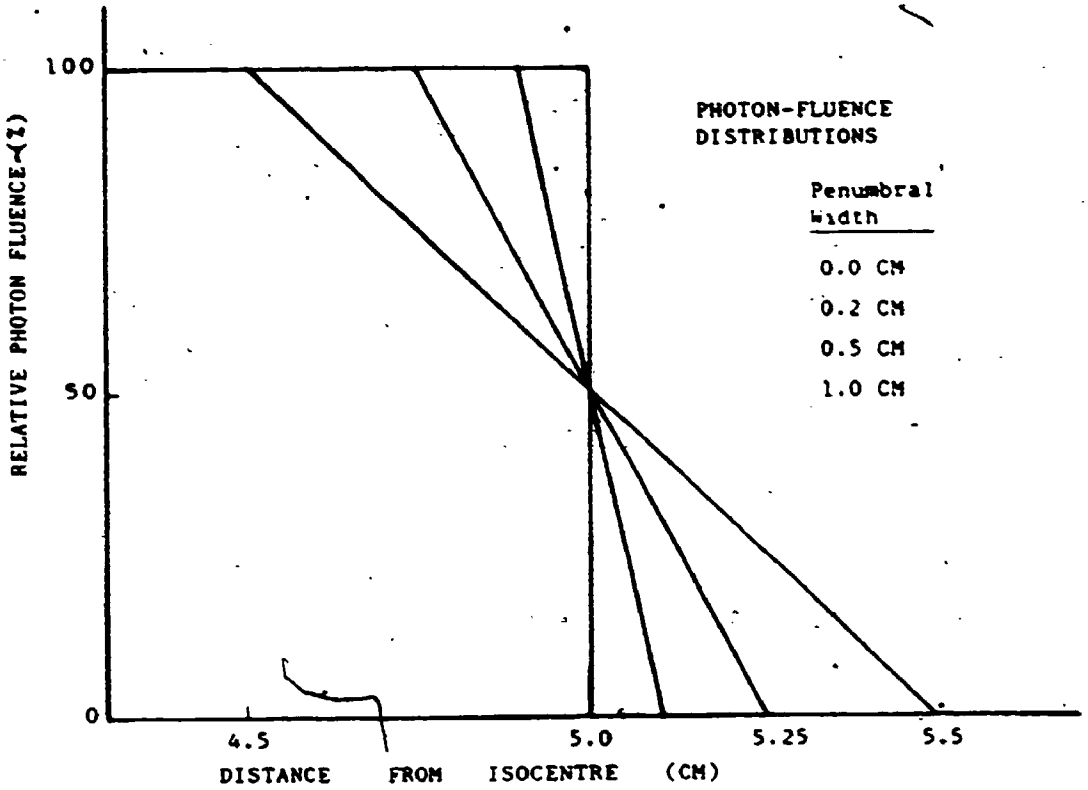

Figure C.1: Idealized Photon-Fluence Distributions.

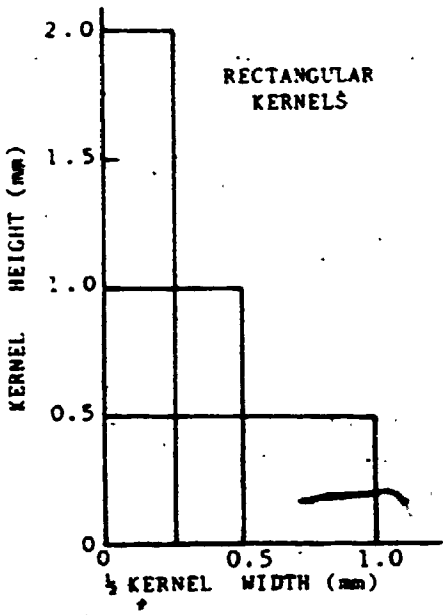

Figure C.2

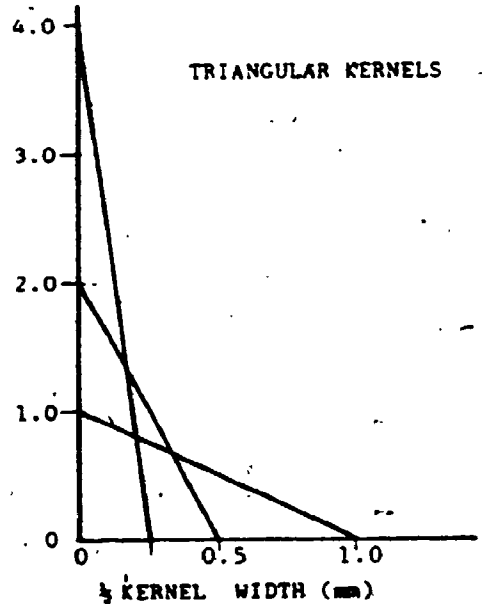

Figure C.3

Figures C.2 and C.3: Idealized Rectangular and Triangular Kernels

density of the medium. As the beam energy increases or the electron density of the wall material decreases, the kernel shape moves from a rectangular to a triangular shape. Idealized rectangular and triangular kernels were, therefore, used to approximate the calculated kernels. The height of each rectangular kernel was equal to the reciprocal of the kernel width while the height of each triangular kernel was equal to twice the reciprocal of the kernel width (the base of the triangle) as illustrated in Figures C.2 and C.3

The rectangular and triangular kernels were convolved with the idealized penumbral photon-fluence distributions using the one-dimensional convolution equation:

$$D(n) = \sum_{m=1}^{M} K(m) \cdot F(n-m) \qquad (C.1)$$

where D(n) is the dose or convolution product, F(n) is the photon fluence, K(m) is the kernel and m, n are the incremental indices.

The P20-80 and P10-90 penumbral dose widths, determined as a function of the kernel width from the convolution products, are illustrated in Figures C.4, C.5 C.6 and C.7 for photon-fluence widths of 0, 0.2, 0.5 and 1.0 cm respectively.

For photon-fluence distributions of any width, the

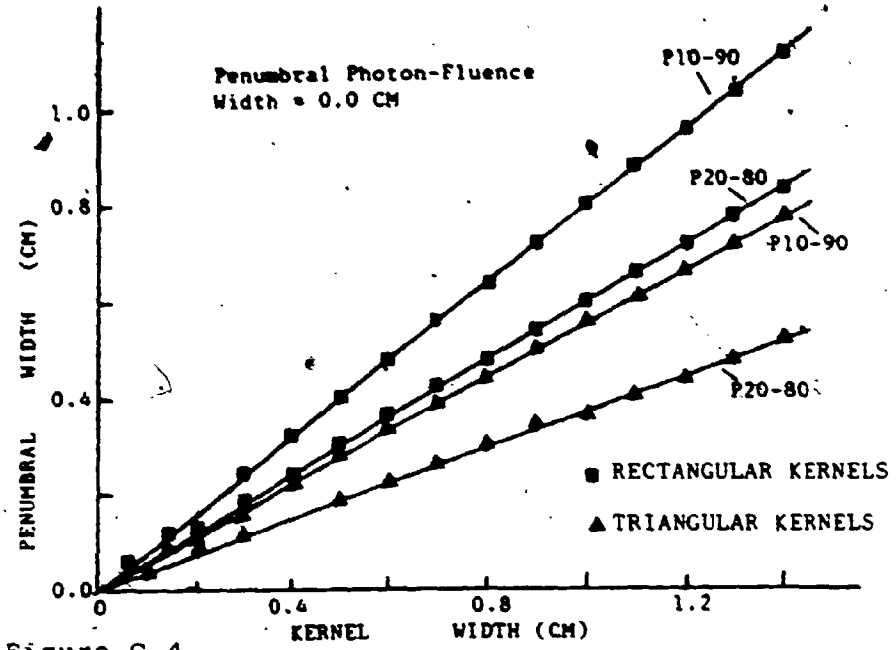

Figure C.4

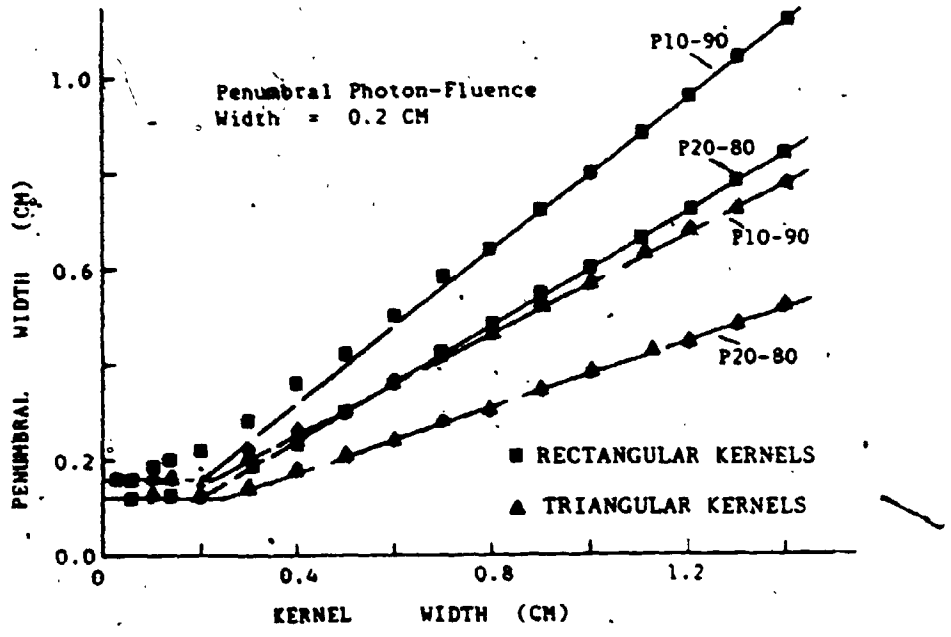

Figure C.5

Figures C.4 and C.5: P20-80 and P10-90 Penumbral Widths versus Kernel Width for Idealized Photon-fluence Distributions of 0.0 and 0.2 cm Penumbral Width respectively.

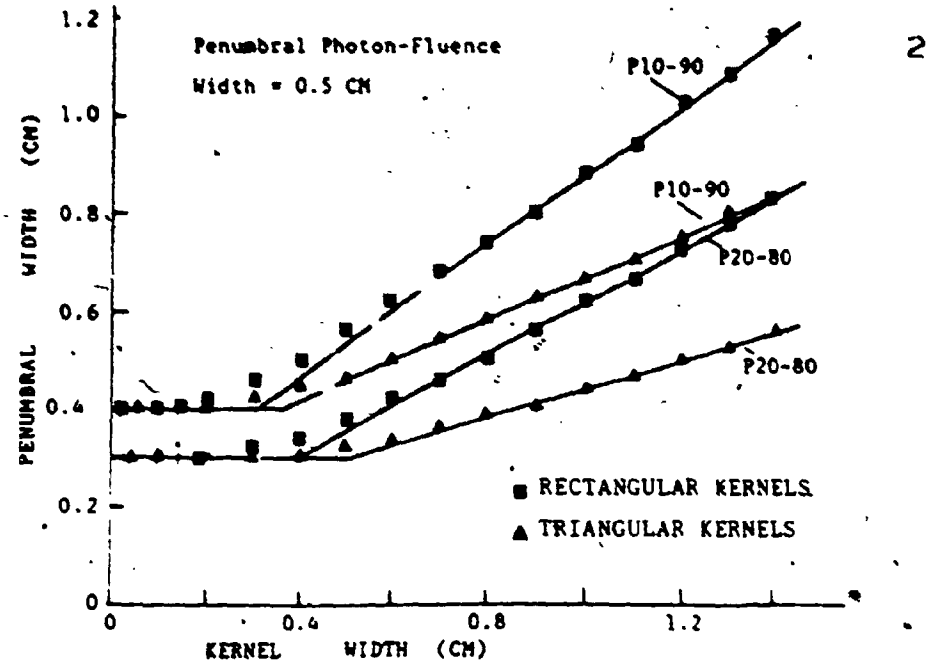

Figure C.6

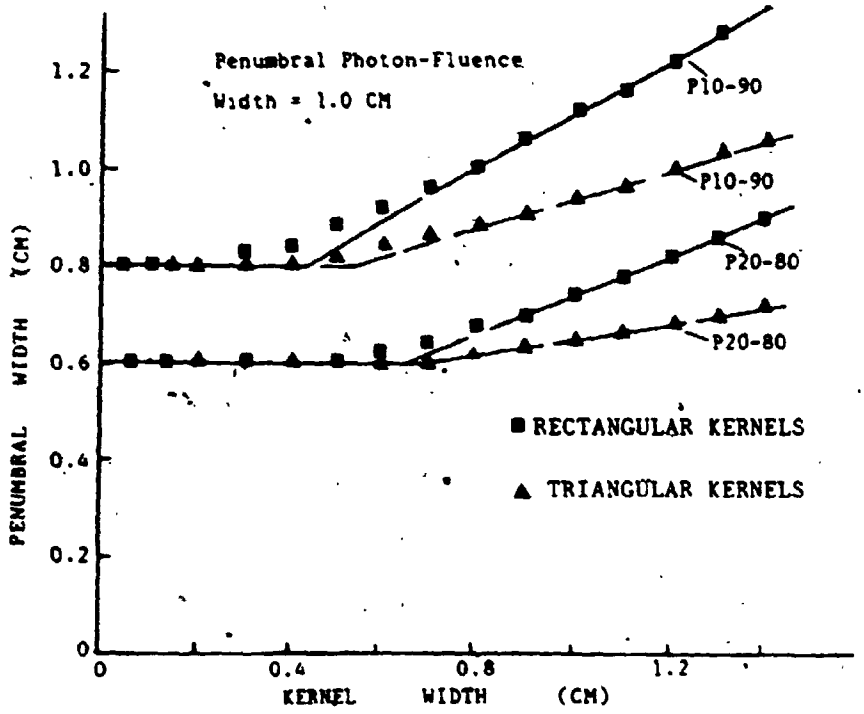

Figure C.7

Figures C.6 and C.7: P20-80 and P10-90 Penumbral Widths versus Kernel Width for Idealized Photon-fluence Distributions of 0.5 and 1.0 cm Penumbral Width respectively.

P20-80 and P10-90 penumbral dose intercepts corresponding to kernel widths of zero dimensions are equivalent to the corresponding penumbral widths for the photon-fluence distributions. When the kernel width is entirely on the linearly decreasing component of the penumbral photon-fluence distribution, the penumbral dose widths are equivalent to the penumbral dose intercepts corresponding to kernel widths of zero dimensions. In this case, for the P20-80 and P10-90 penumbral widths, the corresponding half-widths of the kernels are 0.1 and 0.2 times the photon-fluence penumbral widths.

The dependence of the penumbral dose width on the width of the kernel is related to the degradation associated with the inside diameter of the ionization chamber. The penumbral dose widths increase linearly with kernel width for kernels widths wider than the corresponding photon-fluence penumbra. For small kernel widths, the convolution products (or penumbral dose distributions) are constant and the dependence of the convolution product on the kernel width is reduced to zero. Intermediate slopes are determined for intermediate kernel widths for photon-fluence distributions of finite width.

The slopes of the P20-80 and P20-90 penumbral dose widths versus kernel width for both rectangular and triangular kernels are indicated as a function of the width

Table C.1

FIGURE	Photon-Fluence Penumbral Width (P100-0) (cm)	P20-80 Penumbral Width (CM)		P10-90 Penumbral Width (CM)	
		P20-80 Slopes (cm/cm k.w.)		P10-90 Slopes (cm/cm k.w.)	
		Rectangular Kernel	Triangular Kernel	Rectangular Kernel	Triangular Kernel
C.1	0.0	0.60	0.37	0.80	0.56
C.2	0.2	0.60	0.34	0.80	0.53
C.3	0.5	0.53	0.29	0.69	0.42
C.4	1.0	0.40	0.16	0.56	0.30

k.w. means kernel width

Table C.1: Convolution Results from Idealized Photon-Fluence Distributions and Kernels.

of the penumbral photon-fluence distribution in Table C.1. Some general conclusions relating to those slopes can be drawn. The P10-90 slopes are from 0.15 to 0.2 larger than the P20-80 slopes. Similarly, the slopes for rectangular kernels are approximately 0.25 larger than those for triangular kernels. Both the P10-90 and P20-80 slopes decrease as the width of the photon-fluence width increases. The slopes for most practical situations (for both the photon-fluence distribution and the kernel) vary from 0.4 to 0.6. These results can be used to explain some of the theoretical results presented in Chapter V.

APPENDIX D

PROGRAM FOR KERNEL CALCULATION

The PROGRAM KANAL calculates one-dimensional kernels, K(xi,hv,pe,i.d.) at intervals of 0.1mm as a function of the photon energy, hv, the chamber wall electron density, pe, and the inside diameter of the cylindrical ionization chamber.

Compton equations are used to determine the energy distribution of the Compton electrons;

Klein-Nishina differential collision cross section formula is used to determine the scattering probability of the electrons per unit solid angle;

Electron stopping powers are used to determine the range of the secondary electrons in the chamber wall.

```
C*************************************************************
C**    XINC - STEP SIZE
C**    ALPHA - PHOTON ENERGY IN ELECTRON MASS UNITS
C**    (0.511 MEV)
C**    ATCOEF - ATTENUATION COEFFICIENT (OF CHAMBER WALL
C**    MATERIAL)
C**    DEN - DENSITY OF CHAMBER WALL MATERIAL
C**    RMAX - DEPTH OF MAXIMUM ELECTRONIC BUILDUP (IN WATER)
C**    SBAR - ELECTRON STOPPING POWER
C**    XMAX - MAXIMUM LATERAL RANGE OF THE ELECTRONS
C*************************************************************
```

```
      PROGRAM KANAL
      REAL KERNAL(1500),THLUT(158),RADLUT(158),INRAD,IN2
      REAL ATTEN(800),LOWER,OFSETS(10),EOUT(158),THETA(158)
      REAL XX(1200),XK(1000),YK(1000),OUTRAD,RORAD,INDIAM
      INTEGER NSTEP,NSTEP2,LAST

      BYTE OFILE(11),OTEST(11) INFOFL(11)

      OFILE(11)=0
      OTEST(11)=0
      INFOFL(11)=0

      XINC = 0.1
      WRITE(5 10)
   10 FORMAT(' INPUT THE DESIRED INFORMATION FILE ',$)
      READ(5,15) (INFOFL(II), II=1,10)
   15 FORMAT(10A1)
      OPEN(UNIT=2,TYPE='NEW',FORM='FORMATTED',NAME=INFOFL)
      WRITE(5,20)
   20 FORMAT(' INPUT ALPHA, ATTEN. COEFF. ',$)
      READ(5,25) ALPHA, ATCOEF
   25 FORMAT(F6.4,F10.6)
      WRITE(5 30) ALPHA, ATCOEF
   30 FORMAT(1H ,10X,'ALPHA = ',F6.4,2X,'ATTEN. COEF. ='
     1                          ,F10.6,/)
      WRITE(5,35)
   35 FORMAT(' INPUT DENSITY OF CHAMBER WALL ',$)
      READ(5,40) DENS
   40 FORMAT(F6.3)
      WRITE(5 45)
   45 FORMAT(' INPUT RMAX ',$)
      READ(5 50) RMAX
   50 FORMAT(F6.3)
      WRITE(5,55) DENS, RMAX
   55 FORMAT(1H ,'DENSITY = ',F6.3,2X,'RMAX = ',F6.3,/)
      WRITE(5,60)
   60 FORMAT(' INPUT SBAR IN ALPHA(0.511) UNITS. ',$)
      READ(5 62) SBAR
   62 FORMAT(F7.4)
      WRITE(5,64) SBAR
   64 FORMAT(1H ,'SBAR = ',F7.4,/)

C      Call lut to calculate the LOOKUP TABLE used to reduce
C     calculation inside the integration loops.

      CALL LUT(SBAR,ALPHA,DENS,THETA,EOUT,THLUT,RADLUT,XMAX)

C      Set up 5 offsets at 0.18,0.36,0.54,0.72,0.90 of the
C     maximum lateral  range of the electrons

      DO 65 I=1,5
         OFSET(I)=XMAX*I/5.5
   65 CONTINUE
```

```
      WRITE(2,66)
 66   FORMAT(' ----------------------------------------',/)
      WRITE(2 67) INFOFL
      WRITE(5,67) INFOFL
 67   FORMAT(' THE INFORMATION FILE IS ',20A1,/)
      WRITE(5,68) ALPHA, XMAX
 68   FORMAT(' ALPHA = ' F6.3 3X,' THE MAXIMUM LATERAL ',
     1       'SPREAD = ',F8.4)
      WRITE(2 70) DENS, RMAX SBAR
      WRITE(5 70) DENS, RMAX,SBAR
 70   FORMAT(' DENSITY = ' F6.3 4X,'RMAX = ',F5.2,2X,
     1       ' SBAR = ',F5.2,/)

      DO 999 KOUNT = 1 5
         WRITE(2,101)
101       FORMAT(' ----------------------------------------')
         WRITE(5,102)
102      FORMAT(' INPUT THE INNER RADIUS ',$)
         READ(5,103) INRAD
103      FORMAT(F5.2)
         WRITE(5,104)
104      FORMAT(' INPUT THE DESIRED OUTPUT FILE  ',$)
         READ(5,105) (OFILE(II),II=1,10)
105      FORMAT(20A1)

         OPEN(UNIT=3,TYPE='NEW',FORM='FORMATTED',NAME=OFILE)
         WRITE(2,110) OFILE
110      FORMAT(1H ,30X,10A1)

         CHDIAM = 2.0*(INRAD+RMAX)
         OUTRAD = CHDIAM/2.0
         RL = OUTRAD/0.1
         NUM = (CHDIAM/.2) + 1

C        Create a LOOKUP TABLE of ATTENUATIONS

         DO 150 I=1,NUM
               DEPTH=XINC*(I-1)
               ATTEN(I)=EXP(DEPTH*DENS*ATCOEF)
150      CONTINUE
         SUM=0.0
         IN2=INRAD**2
         RSQUAR=OUTRAD**2
         NWALL=RL+1
         NSTEP=NWALL
         NSTEP2=2*NSTEP
         NZERO=NSTEP-((1.0*(XMAX+INRAD))/0.1)-1
         IF(NZERO.LT.0) NZERO=0
         IF(NZERO.EQ.0) GOTO 160
         DO 155 I=1,NSTEP
               KERNAL(I)=0.0
               KERNAL(NSTEP2-I)=0.0
155      CONTINUE
160      CONTINUE
```

```
      DO 200 I=NZERO,NSTEP
              WRITE(5,165) I
  165         FORMAT(I6)
      X=((I-1)*XINC)-OUTRAD
      IF(ABS(X).EQ.INRAD) X=-INRAD-0.01
      Y=SQRT(RSQUAR-X**2)
      IF(-X.LT.INRAD) GO TO 170
      CALL INTEG(X,-INRAD,Y,INRAD,THLUT,RADLUT,
     1                  XINC,ATTEN,KERNAL(I),OFSETS)
      GO TO 180
  170 CONTINUE

C     YINT is the y value of the edge of the cavity at X.

      YINT=SQRT(IN2-X**2)+XINC
      IF(YINT.GE.INRAD) GO TO 175
      CALL INTEG(X,-INRAD,-YINT,INRAD,THLUT,RADLUT,
     1                  XINC,ATTEN(NWALL),LOWER,OFSETS)
  175         CONTINUE
      CALL INTEG(X,YINT,Y,INRAD,THLUT,RADLUT,
     1                           XINC,ATTEN,UPPER,OFSETS)
      KERNAL(I)=UPPER+LOWER
  180         CONTINUE
      KERNAL(NSTEP2-I)=KERNAL(I)
      SUM=SUM+2.0*KERNAL(I)
      WRITE(5,185) X,KERNAL(I),SUM,OFILE
  185         FORMAT(1X,'X = ' 3(F12.4,2X),3X,20A1,/)
  200 CONTINUE

      SUM=SUM-KERNAL(NSTEP)
      WRITE(5,210) SUM
  210 FORMAT('  SUM = ',F20.8,/)

C     Normalize the KERNELS

      DO 220 I =1,NSTEP2-1
      XX(I)=((I-1)*0.1)-OUTRAD
      KERNAL(1)=KERNLA(I)/SUM
  220 CONTINUE

        DO 230 I=1,NSTEP2-1
      IF(XX(I).EQ.0.0) GOTO 235
  230   CONTINUE
  235   N=1
        J=0
        DO 250 I=N,NSTEP2
      J=J+1
      IF(KERNAL(I).EQ.0.0) GOTO 255
  250   CONTINUE
  255   MAX=J
        MAX2=2*MAX-1
        WRITE(5,260) MAX,MAX2
        FORMAT(6X,'MAX = ' I4.5X,'MAX2 =',I4,/)
```

```
      J=0
      DO 270 I=1,MAX-1
      J=J+1
      YK(MAX-I)=KERNAL(N-J)
      YK(MAX+I)=YK(MAX-I)
270   CONTINUE
      YK(MAX)=KERNAL(N)
      DO 280 I=1,MAX2,5
           WRITE(3,275) ((I+J), YK(I+J),J=0,4)
275        FORMAT(1H ,5(I3,2X,F12.7,2X),/)
280   CONTINUE
      CLOSE(UNIT=3)
      WRITE(5,290) OFILE
290    FORMAT(1H ,30X,10A1,/)
      WRITE(5,295) INRAD,INDIAM
      WRITE(2,295) INRAD,INDIAM
295    FORMAT(1H ,'IN. RADIUS = ',F5.1,3X,'IN. DIAMETER'
     1                ' =',F5.1,/)
      WRITE(5,296) CHDIAM
      WRITE(2,296) CHDIAM
296    FORMAT(1H ,'CHAMBER DIAM. =',F6.2,4X,'P20-80 = ',
     1                6X,'P10-90 = ',/)

999   CONTINUE


      WRITE(2,314)
      WRITE(2,315) INFOFL
      WRITE(5,315) INFOFL
      WRITE(5,316) ALPHA, XMAX
      WRITE(2,316) ALPHA, XMAX
      WRITE(5,317) DENS, RMAX, SBAR
      WRITE(2,317) DENS, RMAX, SBAR
      WRITE(2,318)
314    FORMAT(' ----------------------------------------',/)
315    FORMAT(' THE INFORMATION FILE IS ', 20A1,/)
316    FORMAT(' ALPHA = ',F6.3,3X,' THE MAXIMUM LATERAL ',
     1          'SPREAD = ',F8.4)
317    FORMAT(' DENSITY = ',F6.3,4X,'RMAX = ',F5.2,'SBAR = ',
     1          F5.2,/)
318    FORMAT(' ----------------------------------------',/)

      CLOSE(UNIT=2)
      STOP
      END
```

```
C*****************************************************************
C
C       This routine calculates the LOOKUP TABLES for angular
C       probability and the maximum range of an electron of
C       given initial energy for a given scattering angle.
C
C*****************************************************************

      SUBROUTINE LUT (SBAR,ALPHA,DENS,THETA,EOUT,THLUT,
     1                                        RADLUT,XMAX)
      REAL THLUT(158),RADLUT(158),EOUT(158),THETA(158)
      THLUT(158)=0.0
      RADLUT(158)=0.0
      EOUT(158)=0.0

      THETA(158)=1.570795
      R=1.0
      XMAX=0.0
      DO 100 I=1,157
       THETA(I)=0.005+0.1*(I-1)
       SINTH=SIN(THETA(I))
       TANTH=SINTH/COS(THETA(I))
             CALL ANGLE(TANTH,ALPHA,THLUT(I),EOUT)
       CALL RANGE(SBAR,R,EOUT,FR,RAD)

C      The ranges calculated by RANGE are for water, scale
C      by dividing by realtive electron density

       RAD=RAD/DENS
       X=SINTH*RAD
       RADLUT(I)=RAD
       IF(X.GT.XMAX) XMAX=X
100    CONTINUE
      WRITE(5,20) XMAX
 20    FORMAT(' THE MAXIMUM LATERAL SPREAD IS ',F10.4)
      RETURN
      END
```

```
C*************************************************************
C
C       This routine implements the Klein-Nishina equation
C       for the scattering probability per unit solid angle,
C       and calculates the energy of the scattered electron.
C
C*************************************************************

        SUNROUTINE ANGLE(X,ALPHA,FX,EOUT)
        DATA ROSQU/0.0794112/
        TANPH=X
        SINPH=SIN(ATAN(TANPH))
        THETA=2.0*ATAN(1.0/(TANPH*(1.0+ALPHA)))
        COSTH=COS(THETA)
        TERM1=1.0/(1.0+ALPHA*(1.0-COSTH))
        TERM2=0.5*(1.0+COSTH**2)
        T3TOP=ALPHA**2*(1.0-COSTH)**2
        T3BOT=(1.0+COSTH**2)*(1.0+ALPHA*(1.0-COSTH))
        TERM3=1.0+T3TOP/T3BOT
        DSIG=ROSQU*TERM1**2*TERM2*TERM3
        FX=DSIG*(1.0+COSTH)*SIN(THETA)/((1.0+ALPHA)*SINPH**3)
        EOUT=(1.0-TERM1)*ALPHA
        RETURN
        END

C*************************************************************
C
C   This routine calculates the maximum range of an electron
C      of a given initial energy using the average electron
C      stopping power.
C
C*************************************************************

        SUBROUTINE RANGE (SBAR,R,E,FR,MAXRAD)
        REAL MAXRAD,LNE

        FR=0.0
        MAXRAD=E/SBAR
        IF (MAXRAD.GE.R) FR=1.0/R
        RETURN
        END
```

```
C*****************************************************************
C        This Subroutine calculates the line integrals
C*****************************************************************
      SUBROUTINE INTEG(XIN,Y0,Y1,INRAD,THLUT,RADLUT,
     1                 XINC,ATTEN,INTGRL,OFSETS)
      REAL MODSTP,LOWF,INTGRL,PARAM(1),LTHETA,LRAD,INRAD
      REAL PATH(15),THLUT(158),RADLUT(158),ANGLES(15)
      REAL RADII(15),ATTEN(1),OFSETS(5),COSTH(15),ORADII(15)
      REAL SUB(15),OANGLE(15),OPATH(15)
      DIFF=Y1-Y0
      NSTEP=DIFF/XINC+1
      MODSTP=DIFF/NSTEP
      HLFSTP=MODSTP/2.0
      SUM=0.0
      X=ABS(XIN)
      RAD2=INRAD**2
      YFIRST=Y0-HLFSTP
      NSTP2=NSTEP+2
      DO 100 ISTEP=1,NSTEP+1
       Y=YFIRST+ISTEP*MODSTP
       IF(HLFSTP.EQ.0) GOTO 30

C   Call SUBTND to determine the scattering angles and radii
C   from the point of scattering to the edge of the cavity
C       in the 0 offset plane
        CALL SUBTEND(X,Y,INRAD,RAD2,ANGLES,RADII,THSUB,
     1                                  PATH,COSTH,SUB,S1,S2)

C  Call PIXINT to calculate the contribution to the cavity
C       in the 0 offset plane
        CALL PIXINT(ANGLES,RADII,THLUT,RADLUT,PINTGL,
     1                          THSUB,PATH,SUB)

        DO 50 ISLICE=1,5

C  OFAXIS calculates the scattering angles and radii
C  necessary to scatter into an offset cavity volume

            CALL OFAXIS(COSTH,RADII,PATH,OFSETS(ISLICE),
     1                      OANGLE,ORADII,OPATH,S1,S2,THSUB,SUB)
            CALL PIXINT(OANGLE,ORADII,THLUT,RADLUT,OINTGL,
     1                                  THSUB,PATH,SUB)
            PINTGL=PINTGL+2.0*OINTGL
 50             CONTINUE
        GO TO 31
 30             CONTINUE
        PINTGL=0.0
 31             CONTINUE
        SUM=SUM+PINTGL*ATTEN(NSTP2-ISTEP)
100.    CONTINUE
      INTGRL=SUM*DIFF/NSTEP
      RETURN
      END
```

```
C*****************************************************************
C This routine calculates the scattering angles, radii
C and pathlength from the scattering point to 15 points
C       on the circumference of the cavity with no offset.
C
C        B is the inside radius;
C        B2 is the inside radius squared;
C        C is the distance from the scattering point to the
C       centre of the cavity;
C   A is the distance from the scattering point to that point
C on the circumference of the cavity where a line from the
C       scattering point is tangential to the circle.
C THMID is the scattering angle to the centre of the cavity;
C THSUB is 1/2 the angle subtended by the cavity with respect
C       to the scattering point;
C        Beta is the angle located at the centre of the cavity;
C*****************************************************************

      SUBROUTINE SUBTND(X,Y,INRAD,RAD2,ANGLES,RADII,
     1                  THSUB,PATH,COSTH,SUB,S1,S2)
      REAL INRAD,ANGLES(15),RADII(15),
     PATH(15),COSTH(15),SUB(15)
      DATA PI/3.1415926535/, PIBY2/1.570796327/

      B=INRAD
      B2=RAD2
      C2=X**2+Y**2
      C=SQRT(C2)
      A=SQRT(C2-B2)
      THSUB=ATAN(B/A)
      THMID=ATAN(X/Y)
      IF (THMID.LT.0.0) THMID=PI+THMID
      S1 = A*SIN(THSUB)
      S2 = A*COS(THSUB)
      S2 = S2*S2
      THINC=THSUB/7.5
      DO 100 ITHETA=1,7
         DTHETA=(8-ITHETA)*THINC
         ANGLES(ITHETA)=-DTHETA+THMID
         ANGLES(16-ITHETA)=THMID+DTHETA
         COSTH(ITHETA)=COS(ANGLES(ITHETA))
         COSTH(16-ITHETA)=COS(ANGLES(16-ITHETA))
         SINDTH=SIN(DTHETA)
         RATIO=SINDTH/B
         SINALP=C*RATIO
         ALPHA=ATAN(SINALP/SQRT(1.-SINALP**2))
         BETA=ALPHA-DTHETA
         RADII(ITHETA)=SIN(BETA)/RATIO
         RADII(16-ITHETA)=RADII(ITHETA)
         SUB(ITHETA)=1.0/RADII(ITHETA)
         SUB(16-ITHETA)=1.0/RADII(16-ITHETA)
         GAMMA=PI-2.0*ALPHA
         PATH(ITHETA)=B*SIN(GAMMA)/SINALP
         PATH(16-ITHETA)=PATH(ITHETA)
100   CONTINUE
```

```
      ANGLES(8)=THMID
      RADII(8)=C-B
      SUB(8)=1.0/RADII(8)
      PATH(8)=2.0*B
      COSTH(8)=COS(THMID)
      RETURN
      END

C*****************************************************************
C
C   This routine calculates the integral of the probability
C   functions over the 15 rays from the scattering point to
C       cavity disc with the current offset
C
C*****************************************************************

      SUBROUTINE PIXINT(ANGLES,RADII,THLUT,RADLUT,INTGRL,
     1                                          THSUB,PATH,SUB)
      REAL ANGLES(15),RADII(15),THLUT(158),RADLUT(158)
      REAL INTGRL,PATH(15),SUB(15)
      SUM=0.0
      DO 100 I=1,15
            INDEX=100.0*ANGLES(I)+1.0
            IF(INDEX.GT.158) GOTO 100
            FR=0.0
            IF(RADII(I).LE.RADLUT(INDEX)) FR=1.0
            SUM=SUM+FR*THLUT(INDEX)*PATH(I)*SUB(I)
100    CONTINUE
      INTGRL=SUM/15.0*THSUB
      RETURN
      END
```

```
C**********************************************************************
C
C This routine calculates the scattering angles and radii
C       for cavity discs when the offset is nonzero.
C
C COSTH contains the cosines of the 15 rays from the
C scattering point to the cavity for 0 offset.
C RADII contains the corresponding radii for 0 offset.
C PATH contains the corresponding path lengths for 0 offset.
C
C**********************************************************************

      SUBROUTINE OFAXIS(COSTH,RADII,PATH,OFFSET,OANGLE,
     1                  ORADII,OPATH,S1,S2,THSUB,SUB)
      REAL COSTH(15),RADII(15),PATH(15),SUB(15)
      REAL OANGLE(15),ORADII(15),OPATH(15)
      DATA PIBY2/1.570796327/
      OFF2=OFFSET**2
      DO 100 I=1,7

C   Find the radius by Pythagoras

       ORAD=SQRT(RADII(I)**2+OFF2)
       ORADII(I)=ORAD
       ORADII(16-I)=ORAD
       SUB(I)=RADII(I)/(ORAD*ORAD)
       SUB(16-I)=SUB(I)

C    Ratio of pathlengths is equal to the ratio of radii
            OPATH(I)=PATH(I)*ORAD/RADII(I)
       OPATH(16-I)=OPATH(I)
100    CONTINUE
      ORADII(8)=SQRT(RADII(8)**2+OFF2)
      OPATH(8)=SQRT(PATH(8)**2+OFF2)

C  Find the new scattering angles using direction cosines

      DO 200 I=1,15
       COSOTH=COSTH(I)*RADII(I)/ORADII(I)
       OANGLE(I)=PIBY2
       IF(COSOTH.EQ.0.0) GOTO 200
       OANGLE(I)=ATAN(SQRT(1.0-COSOTH**2)/COSOTH)
200    CONTINUE
      THSUB=ATAN(S1/SQRT(S2+OFF2))
      RETURN
      END
```

REFERENCES

1. Agarwal S.K., Marks R.D and Constable W.C.:
Adjacent field separation for homogeneous dosage at a given depth; Data for the 8 MV (Mevatron 8) linear accelerator.
Am. J. Roentgen. 114; 632 (1972).

2. Aird E.G.A and Farmer F.T:
The design of a thimble chamber for the Farmer dosemeter.
Phys. Med. Biol. 17; 169 (1972).

3. Almond P.R.:
'Dosimetry considerations of electron beams'
High-Energy Photons and Electrons: Edited by Krameer S., Suntharalingam Zinninger G.F.

4. Attix F.H. and Roesch W.C. : Editors.
Radiation Dosimetry, Vols. I and II, 2nd Edition.
(Academic Press, 1968).

5. Bagne F.:
A method for calculating megavoltage x-ray dose and dose parameters.
Med. Phys. 7; 664 (1980).

6. Battista J.J. and Bronskill M.J.:
Compton scatter tissue dosimetry: calculation of single and multiple scatter photon fluences.
Phys. Med. Biol. 23; 1 (1978).

7. Battista J.J., Mackie T.R., El-Khatib E. and Scrimger J.W.:
Lung dose corrections for 6 MV and 15 MV x-rays: Anomalies.
IEEE 31-35, (1984).

8. Bentley R.E. and Lillicrap S.C.:
X-ray spectra from accelerators in the range 2 to 6 MeV.
Phys. Med. Biol. 12, 301 (1967).

9. Berger M.J.:
'Monte Carlo calculation of the penetration and diffusion of fast charged particles' in Methods in Computational Physics, Ed. B. Alders, S. Fernbach and M. Rotenberg (New York: Academic Press, 1963).

10. Bevington P.R.:
Data Reduction and Error Analysis for the Physical Sciences.
(McGraw-Hill, 1969).

11. Biggs P.J. and Ling C.C.:
Electrons as the cause of the observed Dmax shift with field size in high-energy photon beams.
Med. Phys. 6, 291 (1979).

12. Bloch P. and Wallace R.:
Computer generated scatter dose distributions for 6-MV radiotherapy photon beams.
Med. Phys. 6, 149 (1979).

13. Boag J.W.:
'Ionization chambers' in Radiation Dosimetry, Vol. II, Instrumentation; 2nd edn. Edited by Attix F.H. and Roesch W.C. (Academic Press, 1966).

14. Boag J.W. and Currant J.:
Current collection and ionic recombination in small cylindrical ionization chambers exposed to pulsed radiation.
Brit. J. Radiol. 53, 471 (1980).

15. Boyer A.L. and Mok E.C.:
Photon beam modeling using Fourier transform techniques.
IEEE 14-16 (1984).

16. Boyer A.L. and Mok E.C.:
A photon dose distribution model employing convolution calculations.
Med. Phys. 12, 188 (1985).

17. British Journal of Radiology:
Central Axis Depth Dose Data for use in Radiotherapy;
Br. J. Radiol., Suppl. 17, (1983).

18. Brownridge J., Samnick S., Stiles P., Tipton P., Veselka J and Yeh N.:
Determination of the photon spectrum of a clinical accelerator.
Med. Phys. 11, 794, (1984).

19. Bruce W.R. and Johns H.E.:
The spectra of x rays scattered in low atomic number materials:
Brit. J. Radiol. Suppl. No. 9, 1960.

20. Burlin T.E.:
'Cavity chamber theory': in Radiation Dosimetry, Vol. I, Fundamentals; 2nd Edn. Edited by Attix F.H. and Roesch W.C. (Academic Press, 1968).

21. Burrus C.S. and Parks T.W.:
DFT/FFT and Convolution Algorithms; Theory and Implementation. John Wiley and Sons, 1985.

22. Cashwell E.O. and Everett C.J.:
A Practical Manual on Monte Carlo Method for Random Walk Problems. 1959.

23. Chan F.K., Haymond H.R., Kagan A.R., Carbone G.E. and George III F.W.:
Comparative beam data for the 25 MV Betatron, 8, 6, and 4 MV linear accelerators, and Co-60 units:- central-axis depth dose, field flatness, and decrement lines.
Radiology 109, 691 (1973).

24. Chan H-P and Doi K.:
The validity of Monte Carlo simulation in studies of scattered radiation in diagnostic radiology.
Phys. Med. Biol. 28, 109 (1983).

25. Coates G. and Webber C.E.:
The influence of certain physical and physiological factors on the in vivo measurement of lung density.
Med. Phys. 9, 478 (1982).

26. Coia L.R. and Moylan D.J.:
Therapeutic Radiology for the House Officer.
(Williams and Wilkins, 1984).

27. Connor W.G., Hicks J.A., Boone M.L.M., Mayer E.G. and Miller R.C.:
10 MV x-ray beam characteristics from a new 18 MeV linear accelerator.
Int. J. Radiat. Oncol. Biol. Phys. 1, 705 (1976).

28. Constantinou and Sternick E.S.:
Reduction of the "horns" observed on the beam profiles of a 6-MV linear accelerator.
Med. Phys. 11, 840 (1984)

29. Cunningham J.R., Shrivastava P.N. and Wilkinson J.M.:
Program IRREG - Calculation of dose from irregularly shaped beams.
Comput. Progr. Biomed. 2, 192 (1972).

30. Cunningham J.R. and Johns H.E.:
The calculation of absorbed dose from exposure measurements: Practical Problems in Dosimetry.
Phys. Med. Biol. 15, 71 (1970).

31. Dawson D.J.:
Tissue maximum ratios for high-energy x rays.
Med. Phys. 4, 423 (1977).

32. Dawson D.J., Harper J.M. and Akinradewo A.C.:
Analysis of the physical parameters associated with the measurement of high-energy x-ray penumbra.
Med. Phys. 11, 491 (1984).

33. Dawson D.J. and Akinradewo A.C.:
Characteristics of cobalt-60 penumbral regions.
Med. Phys. 12, 389 (1985).

34. Devita V.T., Hellman S. and Rosenberg S.A.; Editors.
Cancer: Principles and Practice of Oncology.
J.B. Lippincott company, Toronto, 1982.

35. Dutreix A.:
'Problems of high-energy x-ray beam dosimetry';
High-Energy Photons and Electrons; Edited by S. Kramer, N. Suntharalingam and G.F. Zinninger; (Wiley, 1976).

36. Dutreix J., Dutreix A., and Tubiana M.:
Electronic equilibrium and transition stages.
Phys. Med. Biol. 10, 177 (1965).

37. Evans R.D.:
'X-ray and -ray interactions' in Radiation Dosimetry, Vol. I, Fundamentals (2nd edn.). Edited by Attix F.H. and Roesch W.C. (Academic Press, 1968).

38. Evans R.D.:
The Atomic Nucleus : (McGraw-Hill, 1955).

39. Farmer F.T.: Sub-Standard x-ray dose-meter.
Br. J. Radiol. 28, 304 (1955).

40. Fowler J.F.:
'Solid state electrical conductivity dosimeters';
Radiation Dosimetry, Vol II, Instumentation (2nd edn.). Edited by Attix F.H. and Roesch W. C. (Academic Press, 1966).

41. Gager L.D., Wright A.E., and Almond P.R.:
Silicon diode detectors used in radiological physics measurements. Part I: Developement of an energy compensating shield.
Med. Phys. 4, 494 (1977).

42. Galbraith D.M. and Rawlinson J.A.:
Direct measurement of electron contamination in cobalt beams using a charge detector.
Med. Phys. 12, 273 (1985).

43. Grant III W., Ames J. and lmondND P.R.:
Evaluation of the Therac 6 linear accelerator for radiation therapy.
Med. Phys. 5, 448 (1978).

44. Gray L.: Properties of a diode dosemeter for radiotherapy. Distributed by, Nuclear Associates, 100 Voice Road, Carle Place, NY 11514-1593, New York, U.S.A.

45. Gray L.H.:
Radiation Dosimetry. Part I.
Brit J. Radiol. 10, 600 (1937).

46. Greene D.:
Size of the focal spot in a betatron.
Brit. J. Appl. Phys. 8, 29 (1957).

47. Greene D.:
Observation on the effect of chamber size on measurements of the edge of an x-ray beam.
Brit. J. Appl. Phys. 35, 856 (1962).

48. Hall E.J.:
Radiobiology for the Radiologist; 2nd Edition.
(Harper and Row, 1979).

49. Harper J.M.:
Beam Penumbra for Megavoltage Photons.
M Sc. Thesis, (UWO, 1982).

50. Hendee W.R.:
Medical Radiation Physics, 2nd edn.
(Year Book Medical Publishers, Inc., 1979).

51. Hettinger G., Petterson C. and Svensson H.:
Displacement effect of thimble chambers exposed to a photon or electron beam from a betatron.
Acta Radiol. Ther. Phys. Biol. 6, 61 (1967).

52. Hine G.J.:
Scattering of secondary electrons produced by gamma rays in materials of various atomic numbers.
Phys. Rev. 82, 755 (1951).

53. Holt J.G., Staton R.E. and Sell R.E.:
Ionization collection efficiencies of some ionization chambers in pulsed and continuous radiation beams.
Med. Phys. 5, 107 (1978).

54. Ibbott G.S, Barnes J.E., Hall G.R. and Hendee W.R.:
Stem correction for ionization chambers.
Med. Phys. 2, 328 (1975).

55. International Commission on Radiation Units and Measurements (ICRU): Radiation Dosimetry: X rays and gamma rays with maximum photon energies between 0.6 and 50 MeV. Washington, D.C. (1969).
ICRU Report 14 , Washington, D.C. (1969).

56. International Commission on Radiation Units and Measurements (ICRU): Radiation quantities and units.
ICRU Report 19, Washington, D.C. (1971).

57. International Commission on Radiation Units and Measurements (ICRU):
Radiation Dosimetry: Electrons with initial energies between 1 and 50 MeV.
ICRU Report 21 , Washington, D.C. (1971).

58. International Commission on Radiation Units and Measurements (ICRU): Radiation Dosimetry: Electron beams with energies between 1 and 50 MeV.
ICRU Report 35 (1984).

59. International Commission on Radiation Units and Measurements (ICRU): Stopping powers for electrons and positrons.
ICRU Report 37 (1984).

60. Jacobson A., Burkhead and Scott R.M.:
Correlation of physical characteristics of 4 MV x-ray beams with skin reactions of patients undergoing radiation therapy.
Radiol. 112, 203 (1974).

61. Johns H.E, Cormack D.V, Denesuk S.A and Whitmore G.F.:
Initial distribution of compton electrons.
Can. J. Phys. 30, 556 (1952).

62. Johns H.E. and Cunningham J.R.:
The Physics of Radiology. 4th Edn. (Thomas Springfield, 1983).

63. Johns H.E. and Darby E. K.:
The distribution of radiation near the geometrical edge of an x-ray beam.
Brit. J. Radiol. 23, 193 (1950).

64. Kahlhofer J.:
Description of the dose distribution in the radiation field of a teletherapy unit with Co-60.
Strahlentherapie 157, 329 (1981).

65. Kessaris N.D.:
Penetration of high energy electron beams in water.
Phys. Review. 145, 164 (1966).

66. Kornelsen R.O.:
'Secondary electron effects on dose distributions from photon beams' in Proceedings of Symposium "Computation in Radiation Therapy".
Canadian College of Physicists in Medicine (1983).

67. Kornelsen R.O. and Young M.E.J.:
Changes in the dose-profile of a 10 MV x-ray beam within and beyond low density material.
Med. Phys. 9, 114 (1982).

68. Kuspa J.P. and Tsoulfanidis N.:
Calculation of gamma-ray buildup factors including the contribution of bremsstrahlung.
Nucl. Sci. Engng 52, 117 (1973).

69. Leaver R.H. and Thomas T.R.:
Analysis and presentation of experimental results.
(Wiley, 1974).

70. Lempert G.D., Nath R. and Schulz R.J.:
Fraction of ionization from electrons arising in the wall of an ionization chamber.
Med. Phys. 10, 1 (1983).

71. Ling C.C., Schell M.C. and Rustgi S.N.:
Magnetic analysis of a 10MV photon beam.
Med. Phys. 9, 20 (1982).

72. Mách H. and Rogers D.W.O:
A measurement of absorbed dose to water per unit incident 7 MeV photon fluence.
Phys. Med. Biol. 29, 1555 (1984).

73. Mackie T.R. and Scrimger J.W.:
Computing radiation dose for high energy x-rays using a convolution method.
IEEE 36-40 (1984).

74. Mackie T.R., El-Khatib E., Battista J., Scrimger J., Van Dyk J. and Cunningham J.R.:
Lung dose corrections for 6- and 15-MV x rays.
Med. Phys. 12, 327 (1985).

75. Mackie T.R., Scrimger J.W. and Battista J.J.:
A convolution method of calcualting dose for 15-MV x rays.
Med. Phys. 12, 188 (1985).

76. Mackie T.R.:
Personal communication.

77. Mcginley P.H. and Sanders M.:
Lung correction factors for 45-MV therapy.
Med. Phys. 9, 738 (1982).

78. Minato S.:
Monte Carlo calculation of electron emission from aluminium and lead exposed to 1.25 MeV gamma rays.
Radiat. Res. 56, 1 (1973).

79. Mladjennovic M:
Radioisotope and Radiation Physics, an Introduction.
Academic Press, (1973).

80. Mohan R., Chui C. and Lidofsky L.:
Energy and angular distributions of photons from medical linear accelerators.
Med. Phys. 12, 592 (1985).

81. Nath R., Agostinelli A.G., Gignac C.E. and Schulz R.J.:
Improvement of small-field penumbra and dose distribution on 4 MV accelerator.
Int. J. Radiat. Oncol. Biol. Phys. 7, 957 (1981).

82. Nath R. and Schulz R.:
Calculation response and wall correction factors for ionization chambers exposed to Co-60 gamma rays.
Med. Phys. 8, 85 (1981).

83. O'Connor J.E.:
The variation of scattered x rays with density in an irradiated body.
Phys. Med. Biol. 1, 352 (1957).

84. Orchard P.G.:
Decrement lines: a new presentation of data in Cobalt 60 beam dosimetry.
Brit. J. Radiol. 37, 756 (196).

85. Padikal T.N., Editor, and Fivozinsky S.P, Assoc. Editor:
Medical Physics Handbook.
National Bureau of Standards, Washington, DC, (1982).

86. Padikal T.N. and Deye J.A.:
Electron contamination of a high-energy x-ray beam.
Phys. Med. Biol. 23, 1086 (1978).

87. Paterson M.S. and Shragge C.:
Characteristics of an 18 MV photon beam from a Therac 20 medical linear accelerator.
Med. Phys. 8, 312 (1981).

88. Pla M., Podgorsak E.B., Kim T.H. and Freeman C.R.:
Improved radiotherapeutic techniques for prophylaxis of the central nervous system on patients with acute lymphoblastic leukaemia.
Brit. J. Radiol. 54, 412 (1981).

89. Raeside D.E.:
Monte Carlo principles and applications.
Phys. Med. Biol. 21, 181 (1976).

90. Roesch Wm.C.:
Dose for nonelectronic equilibrium conditions.
Rad. Research 9, 399 (1958).

91. Rogers D.W.O:
'The Use of Monte-Carlo Techniques in Radiation Therapy' in Proceedings of Symposium "Computation in Radiation Therapy" Canadain College of Physicists in Medicine (1983).

92. Sasane J.B. and Iyer P.S.:
Relevance of radiation penumbra in high-energy photon beam therapy.
Stranlentherapie 157, 658 (1981).

93. Scarpa G., Mascati M. and Furetta C.:
Use of thermoluminescent dosimeter for measuring dose distribution with high spatial resolution in partial-body irradiation of small animals.
Br. J. Radiol. 52, 75 (1979).

94. Smith I.H., MacDonald J.C.F, and others.:
Cobalt 60 Teletherapy: A Handbook for the Radiation Therapist and Physicist ; 1964.

95. Sontag M.R. and Cunningham J.R.:
The equivalent Tissue Air Ratio method for making absorbed dose calculations in a heterogeneous medium.
Radiology 129, 782 (1978).

96. Spiegel M.R.:
Theory and Problems of Statistics. (Schaum Outline Series)

97. Suntharalingam N. and Steben J.D.:
Physical characteristics of 45 MV photon beams for use in treatment planning.
Med. Phys.. 4, 134 (1977).

98. Tatcher M. and Palti S.:
Evaluation of density correction algorithms for photon-beam dose calculations.
Radiology 141, 201 (1981).

99. Tronc D. and Gayet P.:
Absorbed dose distributions from the Therac 10 Neptune linear accelerator.
Strahlentherapie 156, 125 (1980).

100. Tsoulfanidis N;
Measurement and Detection of Radiation.
McGraw-Hill Book Co., (1983).

101. Turner A.P. and Anderson D.W.:
Thermoluminescent response of lithium fluoride to high energy photons.
Phys. Med. Biol. 18, 46 (1973).

102. Van Dyk J:
Practical dosimetric considerations of a 10-MV photon beam.
Med. Phys. 4, 145 (1977).

103. Van Dyk J., Battista J.J., and Rider W.D:
Half body radiotherapy: The use of computed tomography to determine the dose to lung.
Int. J. Radiat. Oncol. Biol. Phys., 6, 463 (1980).

104. Waggener R.G, Kereiakes J. G. and Shalek R.J.;
Editors: Handbook of Medical Physics, Vols I.
CRC Press Inc., (1982).

105. Waggener R.G, Kereiakes J. G. and Shalek R.J.;
Editors: Handbook of Medical Physics, Vols II.
CRC Press Inc., (1984).

106. Webb S. and Fox R.A.:
Verification by Monte Carlo Methods of a power law tissue-air ratio algoritm for inhomogeneity corrections on photon beam dose calculations.
Phys. Med. Biol. 25, 225 (1980).

107. Webb S. and Parker R.P.:
A Monte Carlo Study of the interaction of external beam x-radiation with inhomogeneous media.
Phys. Med. Biol. 13, 1043 (1978).

108. Wecksung G.W., Walker J.J. and Brown R.T.:
Monte Carlo calculation of electron production by a gamma beam incident on a thick foil.
Nucl. Instr. Meth. 95, 605 (1971).

109. Wilkinson J.M., Rawlinson J.A and Cunningham J.R:
Dosimetry workshop; Hodgkin's Disease; Chicago, Illinois, (1970).

110. Williamson J.F.:
An effecient method of randomly sampling the coherent angular scatter distribution.
Phys. Med. Biol. 28, 57 (1983).

111. Williamson J.F., Morin R.L. and Khan F.M.:
Dose calibrator response to brachytherapy sources: A Monte Carlo and analytic evaluation.
Med. Phys. 10, 135 (1983).

112. Wong J.W. and Henkelman R.M.:
Second scatter contribution to dose in a Cobalt-60 beam.
Med. Phys. 8, 775 (1981).

113. Wong J.W. and Henkelman R.M.:
Reconsideration of the power-law (Batho) equation for inhomogeneity corrections.
Med. Phys. 9, 521 (1982).

114. Wright A.E. and Boyer A.L, Editors:
Advances in Radiation Therapy Treatment Planning.
American Institute of Physics, Inc., (1983).

115. Wright A.E. and Gager L.D.:
Silicon diode detectors used in radiological physics measurements. Part II: Measurement of dosimetry data for high-energy photons.
Med. Phys. 4, 499 (1977).

116. Young M.E.J. and Kornelsen R.O.:
Dose corrections for low-energy tissue inhomogeneities and air channels for 10-MV x rays.
Med. Phys. 10, 450 (1983).